Doctoral Dissertation

博士論文

Grain boundary diffusion creep of olivine and its role in upper mantle rheology

（オリビンの粒界拡散クリープと上部マントルレオロジーにおける役割）

A Dissertation Submitted for the Degree of Doctor of Philosophy

August 2020

令和 2 年 8 月博士（理学）申請

Department of Earth and Planetary Science,

Graduate School of Science, The University of Tokyo

東京大学大学院理学系研究科地球惑星科学専攻

Kosuke Yabe

谷部　功将

Abstract

Olivine is the most abundant mineral in the Earth's upper mantle and its deformation properties have been intensively studied to understand mantle rheology. Diffusion creep is considered to be one of the major deformation mechanisms. However, the creep properties are controversial. Differences of up to two orders of magnitude in viscosity at the same grain sizes and temperatures have been reported from experimental diffusion creep studies on olivine aggregates. Based on the knowledge of material science, the difference in strength is likely to be due to slight difference in the chemical composition. In this study, I firstly established constitutive equations for olivine diffusion creep which include the effect of the chemical composition, and then calculated the viscosity-depth profiles for the oceanic upper mantle based on the established flow law.

I conducted one-atmosphere uniaxial compression experiments on fine-grained (~1 μm) Fe-bearing olivine ($Mg_{1.8}Fe_{0.2}SiO_4$) aggregates that were variably doped with CaO ± Al_2O_3. I identified power-law interface-controlled creep at low stresses and grain-boundary diffusion creep at high stresses, which operate as mutually coupled, i.e., sequential processes. I established constitutive equations for interface-controlled creep and diffusion creep of undoped olivine:

$$\dot{\varepsilon}_{\mathrm{int}}^{\mathrm{ref}} = 2.12 \times 10^{12} \mu\mathrm{m/MPa^3/s} \cdot (\sigma^3/d) \cdot \exp\left(-\frac{610\ \mathrm{kJ/mol}}{\mathrm{R}T}\right)$$

and

$$\dot{\varepsilon}_{\mathrm{diff}}^{\mathrm{ref}} = 1.12 \times 10^{10}\ \mu\mathrm{m^3/MPa/s} \cdot (\sigma/d^3) \cdot \exp\left(-\frac{470\ \mathrm{kJ/mol}}{\mathrm{R}T}\right),$$

where $\dot{\varepsilon}_{\mathrm{int}}^{\mathrm{ref}}$ and $\dot{\varepsilon}_{\mathrm{diff}}^{\mathrm{ref}}$ are strain rates of interface-controlled creep and grain-boundary diffusion creep, respectively, σ is stress, d is grain size, T is absolute temperature, and R is the gas constant. Then I used the combined rate equation (i.e., $\dot{\varepsilon} = \left(\dot{\varepsilon}_{\mathrm{int}}^{\mathrm{ref}\,-1} + \dot{\varepsilon}_{\mathrm{diff}}^{\mathrm{ref}\,-1}\right)^{-1}$, where $\dot{\varepsilon}$ is the bulk strain rate) as a reference to examine the effect of doping on creep rates. Ca and Al were found to enhance rates of both interface-controlled creep and diffusion creep above certain temperatures, and this effect becomes significant with increasing temperature. I attribute the rate enhancements to grain-boundary disordering promoted by grain-boundary segregation of the dopants at near-

solidus (bulk eutectic temperature) conditions. The enhancements are well described in relation to the sample solidus and an additional activation energy relative to that of the reference creep state:

$$\chi_{\mathrm{int}} = 1 \qquad \text{at } T \leq 0.84 \cdot T_{\mathrm{s}},$$
$$\chi_{\mathrm{int}} = \exp\left[-\frac{\Delta Q}{\mathrm{R}} \cdot \left(\frac{1}{T} - \frac{1}{0.84 T_{\mathrm{s}}}\right)\right] \qquad \text{at } T > 0.84 \cdot T_{\mathrm{s}}$$

and

$$\chi_{\mathrm{diff}} = 1 \qquad \text{at } T \leq 0.92 \cdot T_{\mathrm{s}},$$
$$\chi_{\mathrm{diff}} = \exp\left[-\frac{\Delta Q}{\mathrm{R}} \cdot \left(\frac{1}{T} - \frac{1}{0.92 T_{\mathrm{s}}}\right)\right] \qquad \text{at } T > 0.92 \cdot T_{\mathrm{s}},$$

where χ_{int} and χ_{diff} are the enhancements of interface-controlled creep and diffusion creep rate, respectively, ΔQ is an additional activation energy (= 230 kJ/mol), and T_{s} is bulk eutectic temperature in K. Overall, the creep of doped olivine is well described in terms of $\dot{\varepsilon}_{\mathrm{int}}^{\mathrm{ref}}$ and $\dot{\varepsilon}_{\mathrm{diff}}^{\mathrm{ref}}$ with χ_{int} and χ_{diff} by:

$$\dot{\varepsilon}_{\mathrm{int}} = \chi_{\mathrm{int}} \cdot \dot{\varepsilon}_{\mathrm{int}}^{\mathrm{ref}}$$

and

$$\dot{\varepsilon}_{\mathrm{diff}} = \chi_{\mathrm{diff}} \cdot \dot{\varepsilon}_{\mathrm{diff}}^{\mathrm{ref}},$$

where $\dot{\varepsilon}_{\mathrm{int}}$ and $\dot{\varepsilon}_{\mathrm{diff}}$ are strain rates of interface-controlled creep and grain-boundary diffusion creep, respectively.

I estimated solidus temperatures of the samples used in the previous diffusion creep experiments. These temperatures were used to compare previously reported diffusion creep rates for olivine with my established diffusion creep law. I found that the law explains a difference of up to two orders of magnitude in olivine creep rates at the same temperatures, stresses, grain sizes, and water contents in the previous studies.

The geotherm normalized by the mantle solidus was calculated for the upper mantle with water contents ranging from 0 to 300 μg/g, which predicts depths where grain-boundary diffusion creep is enhanced due to grain-boundary disordering. Constructed viscosity-depth profiles reveal a very thin mantle lithosphere beneath mid-ocean ridges,

with development of the lithosphere away from the ridge, leaving a low-viscosity region below. Given a grain size of 1 mm and depending on the water content, a viscosity of 2–5×10^{19} Pa·s is predicted for the low-viscosity mantle beneath 50-million-year-old seafloor.

Contents

Chapter 1

1. Introduction

1.1. General introduction

Olivine is the most abundant mineral in the Earth's upper mantle and its deformation properties have been intensively studied to understand mantle rheology (e.g. Karato et al., 1986; Hirth & Kohlstedt, 1995ab; Mei & Kohlstedt, 2000ab; Hansen et al., 2011). Three flow mechanisms likely dominate in the mantle: (1) grain-boundary diffusion (Coble) creep (Karato et al., 1986; Hirth & Kohlstedt, 1995a; Mei & Kohlstedt, 2000a), (2) dislocation-accommodated grain-boundary-sliding (GBS) creep (Hirth & Kohlstedt, 1995b; Hansen et al., 2011), and (3) dislocation creep (Karato et al., 1986; Mei & Kohlstedt, 2000b). The constitutive equation of each mechanism is expressed as:

$$\dot{\varepsilon} = A \cdot (\sigma^n / d^p) \cdot \exp\left(-\frac{Q}{RT}\right), \qquad (1\text{-}1)$$

where $\dot{\varepsilon}$ is the strain rate, A is a constant, R is the gas constant, T is absolute temperature, σ is differential stress, d is grain size, n and p are the stress and grain-size exponents, respectively, and Q is activation energy. The corresponding values of (n, p) are (1, 3), (~3, ~1), (3–5, 0) for grain-boundary diffusion creep, dislocation-accommodated GBS creep, and dislocation creep, respectively.

These equations which incorporate water and pressure effects (Hirth and Kohlstedt, 2003) are used for geophysical modeling of mantle flow (e.g., Warren & Hirth, 2006; Behn et al., 2009; Turner et al., 2015). However, over the past 10 years such established equations, especially for grain-size-sensitive creep (i.e., mechanisms (1) and (2)), have been challenged by several studies that include: (i) Bayesian statistical analyses of reported mechanical data that show poor constraints on the flow law parameters used to determine deformation mechanisms (Korenaga & Karato, 2008; Jain et al., 2018), (ii) differences in flow strength of up to two orders of magnitude between naturally derived and synthetic, reagent-derived olivine aggregates (Faul & Jackson, 2007), and (iii) re-analysis of grain size in experimental olivine aggregates using scanning electron microscopy (SEM) with electron back scattered diffraction (EBSD), yielding grain sizes that are finer by up to a factor of 2 than the reported previously sizes (Hansen et al., 2011), all of which are described in detail in *section 1.2.* These uncertainties become amplified when the experimentally determined flow laws are extrapolated to mantle conditions.

Impurity content can range significantly among samples synthesized by different methods and is known to affect diffusional properties by changing the defect concentration and/or the state of chemical bonding (e.g., Yoshida et al., 2002). By using the same materials for different experiments, diffusion creep properties of fine-grained Fe-free olivine aggregates synthesized in our laboratory were determined with less influence from sample-derived uncertainties (Tasaka et al., 2013; Miyazaki et al., 2013; Nakakoji et al., 2018), as summarized in *section 1.3*. Based on their results as well as on consideration of the composition of olivine grain boundaries, I suspect elements other than Fe to play a critical role in diffusion creep of olivine as described in *section 1.4.*

The anisotropic elasticity of the Earth's mantle is mainly explained by crystallographic preferred orientation (CPO) of olivine that forms during mantle flow (Nicolas & Christensen, 1987). Because the CPO has long been considered to result uniquely from dislocation processes, diffusion creep has received less attention than dislocation processes. Recently, olivine CPO has been found to develop during diffusion creep under a condition that seems to correspond to the depth of seismically anisotropic oceanic upper mantle (Miyazaki et al., 2013). A subsequent study by Maruyama and Hiraga (2017a) showed the ubiquitous occurrence of rigid-body-like grain (lattice) rotation induced by grain-boundary sliding (GBS) during diffusion creep. Preferential GBS on low-index-plane grain boundaries (i.e., grain boundaries parallel to a particular low-index crystallographic plane (Hiraga et al., 1999)), which begins at $>0.92 \cdot T_s$ (T_s: solidus in K, corresponding to bulk eutectic temperature), promotes the rotation of low-index grain boundaries toward the shear direction, resulting in CPO (Maruyama & Hiraga, 2017b). Such findings motivated me to examine mantle viscosity in terms of olivine diffusion creep.

The purpose of this study is to establish a constitutive equation for diffusion creep in Fe-bearing olivine which includes the effect of the chemical composition. Non-dimensional flow law is used to quantify the effect, as described in *section 1.5*. Then I calculate the viscosity-depth profiles for the oceanic upper mantle based on the established flow law to exhibit the characteristics of the mantle deforming by the grain-boundary diffusion creep.

1.2. Previous experimental studies of diffusion creep of Fo_{90} olivine

Prior to this study, several studies have reported experimentally obtained strain rates for olivine in diffusion creep, including Karato et al. (1986), Beeman and Kohlstedt (1993), Hirth and Kohlstedt (1995), Mei and Kohlstedt (2000), and Faul and Jackson (2007). In this paper, I use KPF, BK, HK, MK, and FJ to refer to each of these previous studies,

respectively. All these studies used essentially the same deformation apparatus, i.e., a Paterson-type gas-medium apparatus. However, FJ showed that their strain-rate results are different by up to two orders of magnitude even after calibrating them to reference conditions. While it is difficult to attribute the discrepancies to experimental techniques, other possible origins include (i) different sources for the experimental samples as suggested by FJ, (ii) erroneously reported grain sizes (Hansen et al., 2011; Zhao et al., 2019), (iii) different experimental assemblies that affected oxygen fugacity (Cline et al., 2018), and (iv) uncertainties in the experimentally determined flow-law parameters (Korenaga & Karato, 2008). In the following, I discuss the above issues in detail.

1.2.1. Sample sources

Except for FJ, all the studies used pulverized natural olivine crystals from San Carlos, Arizona, USA. I refer to this type of aggregate as SC-olivine, hereafter (Table 1-1). FJ used reagent-derived sol-gels to synthesize olivine powder that was hot-pressed to obtain olivine aggregates. I refer to this type of aggregate as RG-olivine, hereafter. FJ found significantly greater strengths for this material, i.e., strain rates that were more than an order of magnitude lower compared to SC-olivine at the same conditions (i.e., grain size, temperature, and stress) in the diffusion creep regime. FJ attributed the strength of the RG-olivine to its 100% melt-free state, which is difficult to achieve in aggregates using natural crystals. Hand-picked natural olivine crystals are likely accompanied by small amounts of pyroxenes, spinel, and glass phases, all of which could contribute to the formation of melt at the experimental temperature and pressure conditions. Indeed, the presence of small amounts (<1 vol%) of melt were reported in KPF and HK, although its effect on strain rate was estimated to be negligible based on the finding that the strain rate was independent of the melt fraction up to at least 2 vol% (Hirth & Kohlstedt, 1995). In contrast, FJ showed a large weakening due to the introduction of 0.2 vol% basaltic melt in their RG-olivine. The strength of their melt-bearing RG-olivine was comparable to that of SC-olivine; thus, FJ concluded that melt plays a role in diffusion creep of SC-olivine.

1.2.2. Sample assemblies

In the studies considered here, all of the samples were surrounded by metals that were expected to buffer oxygen fugacity during the experiments. HK, MK, and most tests in BK used Ni jackets. KPF and one test in BK used Fe jackets, while FJ used $Fe_{30}Ni_{70}$-lined Fe jackets (Table 1-1). The f_{O_2} buffered by Fe is almost 4 orders of magnitude smaller than that of Ni at the experimental temperatures, while $Fe_{30}Ni_{70}$ is expected to produce an intermediate f_{O_2}. In *chapter 2*, I will discuss the minor effect of f_{O_2} on diffusion creep

rates based on the similarity of creep rates obtained from an f_{O_2} range of more than 6 orders of magnitude. Thus, I assume creep rate to be independent of f_{O_2} and do not distinguish the data based on f_{O_2}. However, f_{O_2} can control the water solubility of olivine (Bai & Kohlstedt, 1993) and hence changes the partition coefficient of water between olivine and melt, $KD_{H_2O}^{ol-melt}$, which in turn controls T_S in wet conditions (see later discussion in *section 3.1.2.2*). $KD_{H_2O}^{ol-melt}$ has been determined at the Ni/NiO buffer but not at Fe/FeO (Mei et al., 2002). Thus, I limit our analysis of wet olivine to the data of MK (Table 1-1) in this study.

1.2.3. Grain sizes

A caveat on the grain size reported in previous studies was first presented by Hansen et al. (2011), who re-examined grain sizes in the samples studied by HK using SEM-EBSD mapping. The mapping resolves smaller grains than is possible by measurements made on optical micrographs of etched surfaces, as conducted in HK. Hansen et al. (2011) obtained average grain sizes that were smaller by up to a factor of 2 than those reported by HK. Such grain size overestimates in HK could result in an underestimation of olivine strength by a factor of 8 in grain-boundary diffusion creep (Eq. (1-1) with p of 3), which accounts for some of the strength discrepancy between SC-olivine and RG-olivine. Similarly to Hansen et al. (2011), Zhao et al. (2019) recently remeasured grain sizes in the HK samples based on both EBSD mapping and optical micrographs and found that the grain sizes from both methods became comparable at ≥15 μm. Therefore, I limit our analysis to data for grain sizes of ≥15 μm in HK and MK to minimize uncertainties on the grain sizes (Table 1-1).

Another issue derives from grain sizes obtained from area-based and line-intercept-based methods. Commonly, the average intercept length is multiplied by a factor of 1.5 to convert the 2D size to a 3D grain size. Such a procedure was applied in KPF, HK, MK, and BK (although the specific value of the conversion factor was not described in BK). FJ used EBSD mapping and reported grain sizes by taking the average equivalent circle diameter for each grain multiplied by a factor of $4/\pi$ (= 1.27). I will show that the average intercept length is essentially identical to the area-based size in *section 2.1.4*. To compare creep data with grain sizes defined in the same manner, I used grain sizes that were simply measured without application of a conversion factor in this study, and I simply divided the reported values in KPF, HK, MK and BK by 1.5 and those in FJ by $4/\pi$ (= 1.27).

1.2.4. Comparisons using experimentally determined flow law parameters

All the previous diffusion creep data were acquired under confining pressures (P) ranging from 100 to 450 MPa. With an activation volume (V) of 4 cm^3/mol for Si grain-boundary self-diffusivity (Fei et al. 2016), the strain rate with the form of $\dot{\varepsilon} \propto \exp(-PV/RT)$ is predicted to decrease by 13% as P increases from 0.1 to 450 MPa. Thus, the pressure effect on the creep rates is neglected in the comparisons here. I used the corrected grain sizes, as explained above. The $\dot{\varepsilon}$ of KPF, BK, MK, HK, and FJ were normalized to reference conditions with d of 5 μm and σ of 50 MPa using stress and grain size exponents of 1 and 3, respectively; the data are plotted in Fig. 1-1. Even after grain size correction, the plot indicates the same conclusion reached by FJ: that is, SC-olivine is much weaker than melt-free RG-olivine and the strength of SC-olivine is equivalent to that of RG-olivine with added melt. Data from wet SC-olivine are also included in the figure. The wet olivine is ~5 times weaker than dry olivine, which agrees with the conclusion of MK.

Comparisons of creep data calibrated to certain conditions (such as grain size and stress) with given values of grain size and stress exponents to construct plots similar to Fig. 1-1 are widely used. However, constant values of the flow law parameters are not necessarily guaranteed for different experiments, especially when different source materials are used. On the one hand the previous experimental studies on SC-olivine reported the grain size exponent of 3 for diffusion creep (Hirth & Kohlstedt, 1995; Mei & Kohlstedt, 2000a). On the other hand Jain et al. (2018, 2019) conducted statistical analyses on previously obtained mechanical data of SC-olivine, including the results of HK, MK, and KPF and concluded that a grain size exponent of 2 instead of 3 is statistically plausible, depending on whether the value is retrieved from the entire data set or from individual data sets for each experiment. Such uncertainties in the experimentally determined flow law parameters make it difficult to compare the creep results along with their calibrations using the same flow law parameters, as in Fig. 1-1. To minimize such errors in comparing mechanical data, I will use a nondimensional stress and strain-rate space that allows us to compare essentially intact data from previous studies in *chapter 3*. Our analytical method using the nondimensional space is described in *section 1.5.*

1.3. Creep properties of fine-grained Fe-free olivine aggregates synthesized in our laboratory

Tasaka et al., (2013) analyzed the available experimental data for Fe-free olivine aggregates based on an assumed power-law relationship for high-temperature creep (Eq. (1-1)). Enstatite-bearing (from 0 to 50 vol%) Fe-free olivine aggregates with a grain size

of ~1 μm exhibit n of ~1.5 and p of ~2 at σ in a range of ~10 to ~150 MPa at T of 1260 to 1360˚C, but display an n value of ~3 for σ>~150 MPa (Tasaka et al., 2013). Nakakoji et al., (2018) later showed, based on deformation experiments specifically on olivine + 20 vol% enstatite at a wide range of stresses and temperatures, that the observed strain rates ($\dot{\varepsilon}_{\mathrm{obs}}$) are well described by

$$\dot{\varepsilon}_{\mathrm{obs}} = \left(\dot{\varepsilon}_{\mathrm{int}}{}^{-1} + \dot{\varepsilon}_{\mathrm{diff}}{}^{-1}\right)^{-1} + \dot{\varepsilon}_{\mathrm{disl}}, \quad (1\text{-}2)$$

where $\dot{\varepsilon}_{\mathrm{int}}$ is the strain rate due to interface-controlled creep, which dominates at < ~20 MPa with n = 2 and p = 1 (Eq. (1-1)), $\dot{\varepsilon}_{\mathrm{diff}}$ is the strain rate due to grain-boundary diffusion creep with n = 1 and p = 3, and $\dot{\varepsilon}_{\mathrm{disl}}$ is the strain rate due to dislocation processes. The combined operation of $\dot{\varepsilon}_{\mathrm{diff}}$ and $\dot{\varepsilon}_{\mathrm{int}}$ also explains the observed n and p values that were estimated in aggregates exhibiting superplasticity (i.e., tensile strains of > a few 100%) (Hiraga et al., 2010a). Although diffusion creep models typically assume that grain boundaries act as a perfect sink or source for vacancies, reactions at grain boundaries can limit creep rates, resulting in the occurrence of dependent interface-controlled and diffusion creep processes (Eq. (1-2)). Meanwhile, diffusion creep and dislocation creep are generally accepted to be independent processes that act in parallel, which results in a sigmoidal relationship between $\log \dot{\varepsilon}$ and $\log \sigma$, in which power law creep dominates at both lower and higher stresses than diffusion creep (Fig. 1-2a).

Maruymama & Hiraga (2017a) observed sample surfaces for aggregates of olivine + 5 and 20 vol% diopside during deformation and found that GBS, rigid-body grain rotation, and grain-neighbor switching operated as serial processes, in which a linear relationship held between σ and $\dot{\varepsilon}$. These observed microscale processes all compare well with processes predicted to occur during diffusion-controlled (accommodated) GBS creep (i.e., superplasticity) (Lee, 1970; Ashby & Verrall, 1973; Beere, 1978; Spingarn & Nix, 1978). The micro-process study of Maruyama & Hiraga (2017a) was aimed at understanding an unexpected result concerning the development of intense olivine crystallographic preferred orientation (CPO) in the aggregates (Miyazaki et al., 2013). Aggregates composed of grains with either tabular or equiaxed shapes developed significant CPO or random (or weak) CPO, respectively. The grain boundaries of the tabular grains became aligned parallel to a particular crystallographic plane (I refer to such boundaries as low-index plane GBs) at ≥1250˚C. These boundaries were estimated to have a lower viscosity by a factor of ~3 relative to that of general grain boundaries (Maruyama & Hiraga, 2017b). GBS preferentially occurred at low-index plane GBs, followed by grain rotation that acted

to align low-index GBs parallel to the shear plane. Miyazaki et al., (2013) estimated the development of low-viscosity low-index GBs in olivine to occur at temperatures of >0.92×T_s (where T_s is the mantle solidus) and interpreted observations of anisotropic seismic velocity in the uppermost upper mantle in terms of olivine CPO due to diffusion-controlled GBS creep.

1.4. Chemical effects on creep of fine-grained olivine aggregates

The influence of Fe on diffusional processes in olivine has been addressed by a number of other studies (e.g. Nakamura & Schmalzried, 1984; Wanamaker, 1994). Tasaka et al. (2013) showed that the strength of their Fe-free olivine aggregates compared well to that of Fe-bearing reagent-derived olivine in the diffusion creep field (Faul & Jackson, 2007). Considering that reagent-derived olivine is stronger by 1 to 2 orders of magnitude than aggregates derived from natural olivine during diffusion creep (Hirth & Kohlstedt, 1995a; Faul & Jackson, 2007), I suspect elements other than Fe to play a critical role in diffusion creep of olivine. Particularly in the case of grain-boundary diffusion creep, creep is easily influenced by grain-boundary segregation that occurs in a state of chemical equilibrium (Yoshida et al., 1997, 2002). Ca and Al are known to segregate at olivine grain boundaries (Hiraga et al., 2002, 2003, 2004). Miyazaki et al., (2013) attributed the development of low-index GBs above certain temperatures to a grain-boundary structural transition promoted by the segregation of such elements at near-solidus conditions.

1.5. Nondimensional combined flow law

In this study, I first focus on establishing a constitutive equation for high-temperature creep of undoped Fe-bearing olivine aggregates. As I discuss later, I conducted most deformation experiments under conditions where I could assume $\dot{\varepsilon}_{\mathrm{disl}} \approx 0$ in Eq. (1-2). Thus, the $\dot{\varepsilon}_{\mathrm{obs}}$ in this study likely follows

$$\dot{\varepsilon}_{\mathrm{obs}} = \left(\dot{\varepsilon}_{\mathrm{int}}{}^{-1} + \dot{\varepsilon}_{\mathrm{diff}}{}^{-1}\right)^{-1}, \quad (1\text{-}3)$$

where

$$\dot{\varepsilon}_{\mathrm{int}} = A_{\mathrm{int}} \cdot (\sigma^{n_{\mathrm{int}}}/d) \cdot \exp\left(-\frac{Q_{\mathrm{int}}}{RT}\right) \quad (1\text{-}4)$$

and

$$\dot{\varepsilon}_{\text{diff}} = A_{\text{diff}} \cdot (\sigma / d^{p_{\text{diff}}}) \cdot \exp\left(-\frac{Q_{\text{diff}}}{\text{R}T}\right), \quad (1\text{-}5)$$

where A_{int} and A_{diff} are A (Eq. (1-1)) for interface-controlled creep and diffusion creep, respectively, n_{int} is the stress exponent for interface-controlled creep, p_{diff} is the grain-size exponent for diffusion creep, and Q_{int} and Q_{diff} are Q (Eq. (1-1)) for interface-controlled creep and diffusion creep, respectively. In the above equations, I used a p value of 1 for interface-controlled creep (Eq. (1-4)) and an n value of 1 for diffusion creep (Eq. (1-5)), both of which have a strong theoretical basis with a number of supporting experiments (Coble, 1963; Ashby, 1969; Burton, 1972; Arzt et al., 1983; Wakai & Nagono, 1988; Owen & Chokshi, 1998; Berbon & Langdon, 1999).

Once I establish a constitutive equation for undoped olivine by determining other flow law parameters (i.e., A_{int}, n_{int}, Q_{int}, A_{diff}, p_{diff}, and Q_{diff} in Eqs. (1-4) and (1-5)), I can use it as a reference when comparing mechanical data for doped olivine to examine chemical effects on $\dot{\varepsilon}$. For this purpose, I created a nondimensional space for σ and $\dot{\varepsilon}$ (Bai & Raj, 2005, 2010; Nakakoji et al., 2018) that is defined by the reference constitutive equation. First I consider the quantities $(\sigma^{*\text{ref}}, \dot{\varepsilon}^{*\text{ref}})$ that satisfy $\dot{\varepsilon}_{\text{int}} = \dot{\varepsilon}_{\text{diff}}$ for the reference (= undoped) olivine (Eqs. (1-4) and (1-5); Fig. 1-2a):

$$\dot{\varepsilon}^{*\text{ref}} = A_{\text{int}} \frac{(\sigma^{*\text{ref}})^{n_{\text{int}}}}{d} \exp\left(-\frac{Q_{\text{int}}}{\text{R}T}\right) = A_{\text{diff}} \frac{\sigma^{*\text{ref}}}{d^{p_{\text{diff}}}} \exp\left(-\frac{Q_{\text{diff}}}{\text{R}T}\right).$$

Thus,

$$\sigma^{*\text{ref}} = \left[d^{1-p_{\text{diff}}} \frac{A_{\text{diff}}}{A_{\text{int}}} \exp\left(\frac{Q_{\text{int}} - Q_{\text{diff}}}{\text{R}T}\right)\right]^{\frac{1}{n_{\text{int}}-1}} \quad (1\text{-}6)$$

$$\dot{\varepsilon}^{*\text{ref}} = \left[d^{1-n_{\text{int}}p_{\text{diff}}} \frac{(A_{\text{diff}})^{n_{\text{int}}}}{A_{\text{int}}} \exp\left(\frac{Q_{\text{int}} - n_{\text{int}}Q_{\text{diff}}}{\text{R}T}\right)\right]^{\frac{1}{n_{\text{int}}-1}}. \quad (1\text{-}7)$$

Any $(\sigma, \dot{\varepsilon})$ are transformed to their nondimensional stress (σ_0) and strain rate $(\dot{\varepsilon}_0)$ using $(\sigma^{*\text{ref}}, \dot{\varepsilon}^{*\text{ref}})$ by:

$$\sigma_0 = \frac{\sigma}{\sigma^{*\text{ref}}} \text{ and } \dot{\varepsilon}_0 = \frac{\dot{\varepsilon}}{\dot{\varepsilon}^{*\text{ref}}}, \quad (1\text{-}8)$$

which allows us to compare all the data in a single σ_0-$\dot{\varepsilon}_0$ space (Fig. 1-2b). The

combined flow law of Eq. (1-3) follows as:

$$\dot{\varepsilon}_0 = [(\sigma_0{}^{n_{\mathrm{int}}})^{-1} + (\sigma_0)^{-1}]^{-1} \qquad (1\text{-}9)$$

in this nondimensional space (Fig. 1-2b).

1.6. Overview of this study

In *chapter 2,* I synthesized fine-grained (~1 μm) Fe-bearing olivine ($Mg_{1.8}Fe_{0.2}SiO_4$) aggregates that were variably doped with CaO ± Al_2O_3. One-atmosphere uniaxial compression experiments were conducted on the samples. I established constitutive equations for diffusion creep of undoped olivine, and found that Ca and Al enhanced creep rates. I attribute the rate enhancements to grain-boundary disordering promoted by grain-boundary segregation of the dopants at near-solidus conditions. I succeeded to establish a constitutive equation for diffusion creep in Fe-bearing olivine which includes the effect of the chemical composition through considering the disordering effect at near sample solidus.

In *chapter 3,* I estimated solidus temperatures of the samples used in the previous diffusion creep experiments. These temperatures were used to compare previously reported diffusion creep rates for olivine with my established diffusion creep law. I found that the law explains a difference of up to two orders of magnitude in olivine creep rates at the same temperatures, stresses, grain sizes, and water contents in the previous studies.

In *chapter 4,* the geotherm normalized by the mantle solidus was calculated for the oceanic upper mantle with water contents ranging from 0 to 300 μg/g, which predicts depths where grain-boundary diffusion creep is enhanced due to grain-boundary disordering. Constructed viscosity–depth profiles reveal a very thin mantle lithosphere beneath mid-ocean ridges, with development of the lithosphere away from the ridge, leaving a low-viscosity region below. Given a grain size of 1 mm and depending on the water content, a viscosity of $2–5\times10^{19}$ Pa·s is predicted for the low-viscosity mantle beneath 50-million-year-old seafloor.

Symbols with their descriptions and values used throughout this thesis are summarized in Appendix A.

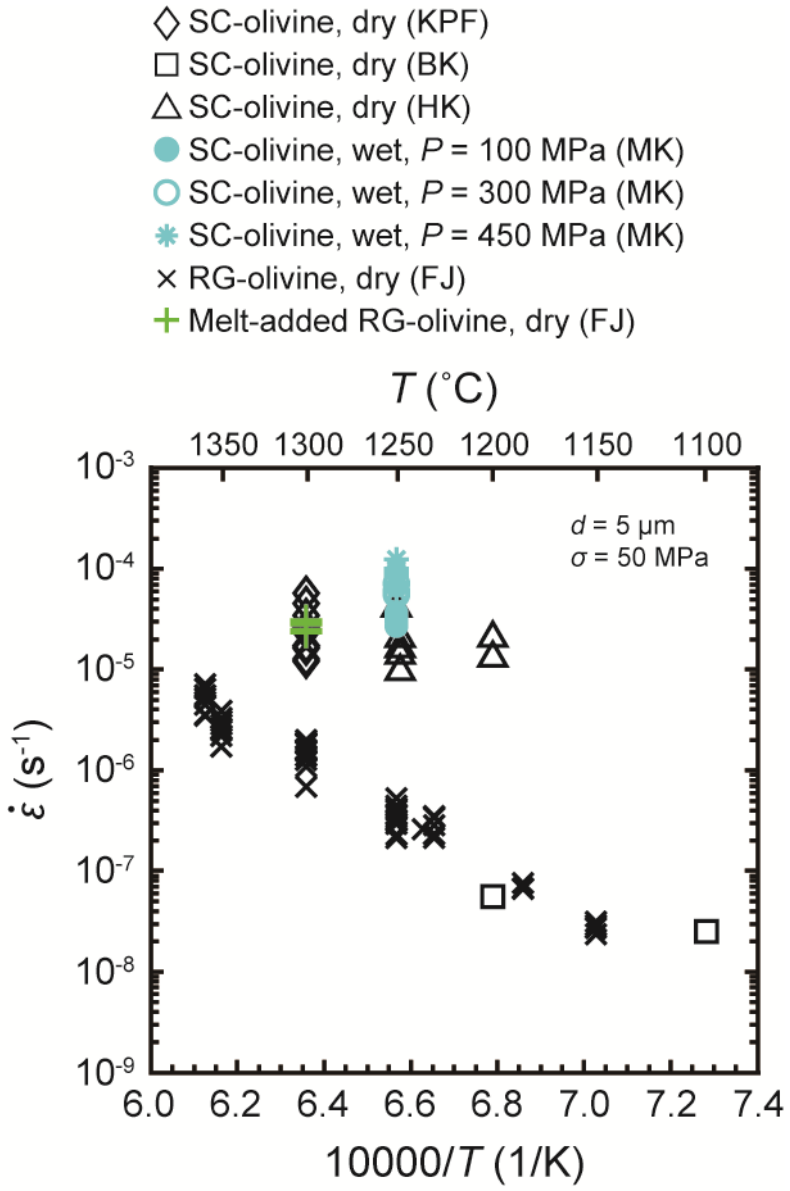

Fig. 1-1. Comparison of previous experimental results for olivine diffusion creep in Arrhenius space. All reported strain rates are calibrated to that at a grain size of 5 μm and stress of 50 MPa using stress and grain-size exponents of 1 and 3, respectively.

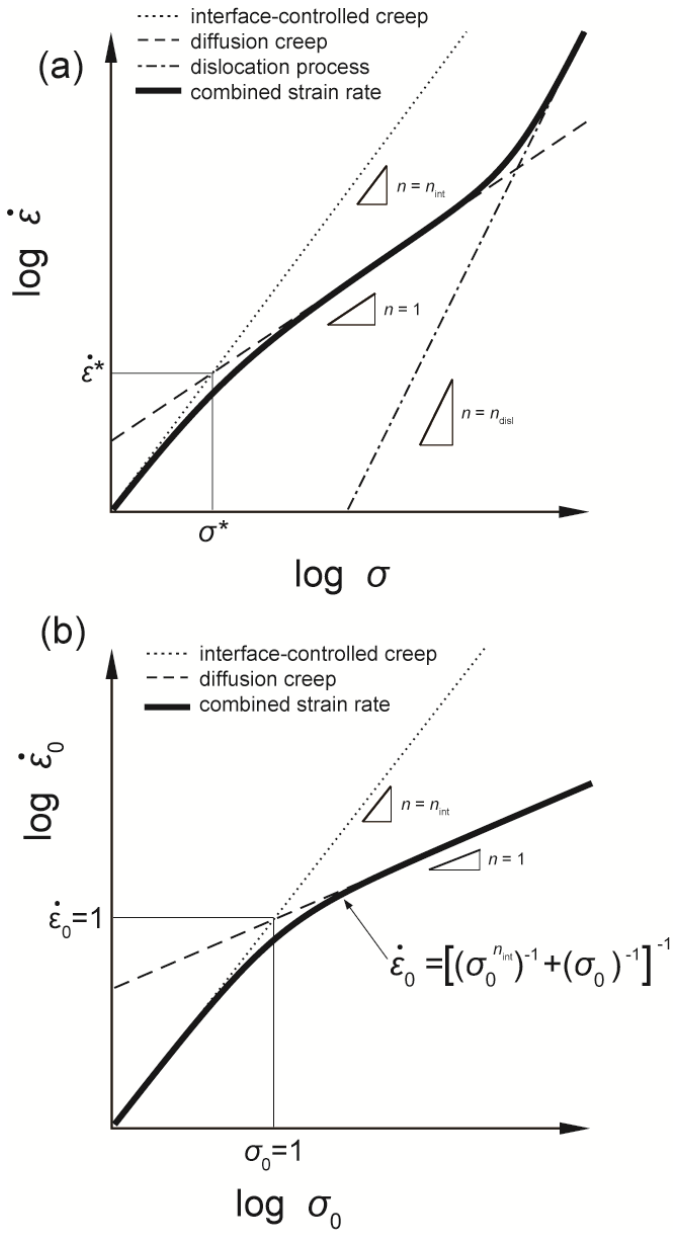

Fig. 1-2. Schematic curves of stress and strain rate with multiple deformation processes operating. (a) Strain rates of individual processes (interface-controlled creep, diffusion creep, and dislocation activity) are shown along with the combined strain rate, assuming that interface-controlled creep and diffusion creep are sequentially connected and diffusion creep and dislocation processes are connected in parallel. Quantities of $(\sigma^*, \dot{\varepsilon}^*)$ satisfy $\dot{\varepsilon}_{\mathrm{int}} = \dot{\varepsilon}_{\mathrm{diff}}$. We specifically refer to $(\sigma^*, \dot{\varepsilon}^*)$ of the undoped reference olivine as $(\sigma^{*\mathrm{ref}}, \dot{\varepsilon}^{*\mathrm{ref}})$ (Eqs. (1-6) and (1-7)). (b) Nondimensionalized strain rates of interface-controlled creep with a stress exponent of n_{int} and diffusion creep with a stress exponent of 1 are shown, as well as the combination of both, with respect to nondimensionalized stress (σ_0).

Table 1-1

Data on previous studies on diffusion creep of Fo_{90} olivine aggregates

References	Experiment no.	σ (MPa)	$\dot{\varepsilon}$ (s^{-1})	d (μm)[a]	T (°C)	P (MPa)	Sample sources	dry / wet	Metal for jackets	T_s (°C)	$C_{H_2O}^{ol}$ (μg/g)
KPF[b]	4746	65	1.0E-05	6.4	1300	300	SC[c]	dry	Fe	1160	-
		88	1.0E-05	8.0	1300	300	SC	dry	Fe	1160	-
	4759	90	3.5E-06	9.3	1300	300	SC	dry	Fe	1160	-
	4778	63	1.1E-05	9.3	1300	300	SC	dry	Fe	1160	-
	4821	25	1.0E-05	4.7	1300	300	SC	dry	Fe	1160	-
		41	1.0E-05	5.6	1300	300	SC	dry	Fe	1160	-
		21	3.5E-06	8.0	1300	300	SC	dry	Fe	1160	-
		58	1.0E-05	8.7	1300	300	SC	dry	Fe	1160	-
	4929	39	1.2E-05	4.6	1300	300	SC	dry	Fe	1160	-
		72	1.2E-05	7.3	1300	300	SC	dry	Fe	1160	-
BK[b]	14	99	2.6E-06	1.3	1100	300	SC	dry	Ni	1160	-
	14	53	3.1E-06	1.3	1200	300	SC	dry	Ni	1160	-
HK[b]	PI-146	58	1.7E-06	12.0	1248	300	SC	dry	Ni	1160	-
		29	4.0E-07	12.0	1248	300	SC	dry	Ni	1160	-
		56	1.3E-06	12.0	1248	300	SC	dry	Ni	1160	-
		55	1.1E-06	12.0	1248	300	SC	dry	Ni	1160	-
	PI-81	94	9.5E-06	10.0	1250	300	SC	dry	Ni	1160	-
		94	3.4E-06	11.2	1200	300	SC	dry	Ni	1160	-
		58	1.2E-06	11.6	1200	300	SC	dry	Ni	1160	-
MK[b]	PI-184	19.1	1.4E-06	10.3	1250	100	SC	wet	Ni	1025	13
		28.2	2.0E-06	10.3	1250	100	SC	wet	Ni	1025	13
		56.1	4.7E-06	10.3	1250	100	SC	wet	Ni	1025	13
		83.5	6.6E-06	10.3	1250	100	SC	wet	Ni	1025	13
	PI-204	27.5	1.7E-06	10.3	1250	100	SC	wet	Ni	1025	13
		28.3	3.9E-06	10.3	1250	300	SC	wet	Ni	1007	34
	PI-295	28.4	4.8E-06	10.1	1250	450	SC	wet	Ni	1013	46
		52.3	8.5E-06	10.1	1250	450	SC	wet	Ni	1013	46
		74.3	1.3E-05	10.1	1250	450	SC	wet	Ni	1013	46
		94.8	2.8E-05	10.1	1250	450	SC	wet	Ni	1013	46
		72.6	1.5E-05	10.1	1250	450	SC	wet	Ni	1013	46
		26.1	3.8E-06	10.1	1250	450	SC	wet	Ni	1013	46
	PI-308	46.8	3.3E-06	10.7	1250	100	SC	wet	Ni	1025	13
		67.4	4.2E-06	10.7	1250	100	SC	wet	Ni	1025	13
		89.9	5.4E-06	10.7	1250	100	SC	wet	Ni	1025	13
	PI-351	38.4	5.2E-06	10.9	1250	300	SC	wet	Ni	1007	34
		58.6	6.6E-06	10.9	1250	300	SC	wet	Ni	1007	34
		82.5	8.7E-06	10.9	1250	300	SC	wet	Ni	1007	34
	PI-569	36.8	8.0E-06	10.5	1250	450	SC	wet	Ni	1013	46
		58.8	1.1E-05	10.5	1250	450	SC	wet	Ni	1013	46
		82.2	1.7E-05	10.5	1250	450	SC	wet	Ni	1013	46

[a]Corrected grain sizes (see text).

[b]KPF: Karato et al. (1986); BK: Beeman & Kohlstedt (1993); HK: Hirth & Kohlstedt (1995); MK: Mei & Kohlstedt (2000)

[c]SC: San Carlos olivine

Table 1-1, Continued.

References	Experiment no.	σ (MPa)	$\dot{\varepsilon}$ (s^{-1})	d (μm)[a]	T (°C)	P (MPa)	Sample sources	dry / wet	Metal for jackets	T_s (°C)	$C^{ol}_{H_2O}$ (μg/g)
FJ[b]	6503	24.5	1.4E-06	2.15	1230	300	RG[c]	dry	$Fe_{30}Ni_{70}$	1540	-
		24.8	1.2E-06	2.21	1230	300	RG	dry	$Fe_{30}Ni_{70}$	1540	-
		32.6	1.6E-06	2.27	1230	300	RG	dry	$Fe_{30}Ni_{70}$	1540	-
		51.9	2.9E-06	2.32	1230	300	RG	dry	$Fe_{30}Ni_{70}$	1540	-
		68.0	4.3E-06	2.36	1230	300	RG	dry	$Fe_{30}Ni_{70}$	1540	-
		79.8	4.8E-06	2.40	1230	300	RG	dry	$Fe_{30}Ni_{70}$	1540	-
		89.2	5.4E-06	2.43	1230	300	RG	dry	$Fe_{30}Ni_{70}$	1540	-
	6509	28.9	1.1E-06	4.34	1300	300	RG	dry	$Fe_{30}Ni_{70}$	1540	-
		59.4	2.8E-06	4.38	1300	300	RG	dry	$Fe_{30}Ni_{70}$	1540	-
		80.5	4.2E-06	4.41	1300	300	RG	dry	$Fe_{30}Ni_{70}$	1540	-
		89.6	4.8E-06	4.44	1300	300	RG	dry	$Fe_{30}Ni_{70}$	1540	-
	6519	22.7	2.2E-06	3.39	1300	300	RG	dry	$Fe_{30}Ni_{70}$	1540	-
		43.3	4.7E-06	3.48	1300	300	RG	dry	$Fe_{30}Ni_{70}$	1540	-
		64.2	6.8E-06	3.53	1300	300	RG	dry	$Fe_{30}Ni_{70}$	1540	-
		86.4	9.3E-06	3.57	1300	300	RG	dry	$Fe_{30}Ni_{70}$	1540	-
	6526	81.5	1.2E-06	3.52	1236	300	RG	dry	$Fe_{30}Ni_{70}$	1540	-
	6527	57.9	2.2E-07	3.51	1185	300	RG	dry	$Fe_{30}Ni_{70}$	1540	-
		77.5	3.2E-07	3.57	1185	300	RG	dry	$Fe_{30}Ni_{70}$	1540	-
		79.5	2.5E-07	3.75	1185	300	RG	dry	$Fe_{30}Ni_{70}$	1540	-
	6530	14.2	2.6E-06	3.64	1360	300	RG	dry	$Fe_{30}Ni_{70}$	1540	-
		15.2	3.5E-06	3.34	1360	300	RG	dry	$Fe_{30}Ni_{70}$	1540	-
		28.7	6.6E-06	3.82	1360	300	RG	dry	$Fe_{30}Ni_{70}$	1540	-
		29.7	8.4E-06	3.39	1360	300	RG	dry	$Fe_{30}Ni_{70}$	1540	-
		60.3	1.6E-05	3.91	1360	300	RG	dry	$Fe_{30}Ni_{70}$	1540	-
		61.1	2.1E-05	3.42	1360	300	RG	dry	$Fe_{30}Ni_{70}$	1540	-
		91.6	2.6E-05	3.96	1360	300	RG	dry	$Fe_{30}Ni_{70}$	1540	-
	6532	15.8	6.8E-07	2.30	1250	300	RG	dry	$Fe_{30}Ni_{70}$	1540	-
		25.9	9.5E-07	2.49	1250	300	RG	dry	$Fe_{30}Ni_{70}$	1540	-
		41.3	1.7E-06	2.60	1250	300	RG	dry	$Fe_{30}Ni_{70}$	1540	-
		60.3	2.9E-06	2.66	1250	300	RG	dry	$Fe_{30}Ni_{70}$	1540	-
		85.6	4.4E-06	2.72	1250	300	RG	dry	$Fe_{30}Ni_{70}$	1540	-
	6534	14.9	6.9E-07	2.55	1250	300	RG	dry	$Fe_{30}Ni_{70}$	1540	-
		19.4	7.8E-07	2.71	1250	300	RG	dry	$Fe_{30}Ni_{70}$	1540	-
		27.6	1.1E-06	2.82	1250	300	RG	dry	$Fe_{30}Ni_{70}$	1540	-
		38.9	1.6E-06	2.89	1250	300	RG	dry	$Fe_{30}Ni_{70}$	1540	-
		53.4	2.3E-06	2.95	1250	300	RG	dry	$Fe_{30}Ni_{70}$	1540	-
		75.6	3.7E-06	2.98	1250	300	RG	dry	$Fe_{30}Ni_{70}$	1540	-
	6540	21.8	8.4E-07	3.53	1300	300	RG	dry	$Fe_{30}Ni_{70}$	1540	-
		21.6	1.1E-06	3.75	1300	300	RG	dry	$Fe_{30}Ni_{70}$	1540	-
		38.8	2.1E-06	3.99	1300	300	RG	dry	$Fe_{30}Ni_{70}$	1540	-
		40.1	2.0E-06	4.09	1300	300	RG	dry	$Fe_{30}Ni_{70}$	1540	-
		53.8	2.9E-06	4.15	1300	300	RG	dry	$Fe_{30}Ni_{70}$	1540	-
		76.0	4.7E-06	4.20	1300	300	RG	dry	$Fe_{30}Ni_{70}$	1540	-
	6542	17.8	1.6E-06	3.61	1350	300	RG	dry	$Fe_{30}Ni_{70}$	1540	-
		23.7	2.3E-06	3.82	1350	300	RG	dry	$Fe_{30}Ni_{70}$	1540	-
		30.1	3.0E-06	3.94	1350	300	RG	dry	$Fe_{30}Ni_{70}$	1540	-
		42.1	4.5E-06	4.03	1350	300	RG	dry	$Fe_{30}Ni_{70}$	1540	-
		56.4	6.3E-06	4.08	1350	300	RG	dry	$Fe_{30}Ni_{70}$	1540	-
		74.4	8.7E-06	4.12	1350	300	RG	dry	$Fe_{30}Ni_{70}$	1540	-
		96.6	1.3E-05	4.15	1350	300	RG	dry	$Fe_{30}Ni_{70}$	1540	-
	6583	27.9	1.9E-07	2.14	1150	300	RG	dry	$Fe_{30}Ni_{70}$	1540	-
		37.4	2.0E-07	2.21	1150	300	RG	dry	$Fe_{30}Ni_{70}$	1540	-
		53.9	3.3E-07	2.27	1150	300	RG	dry	$Fe_{30}Ni_{70}$	1540	-
		75.6	4.8E-07	2.30	1150	300	RG	dry	$Fe_{30}Ni_{70}$	1540	-
	6563	52.2	2.3E-07	24	1300	300	Melt-added RG	dry	$Fe_{30}Ni_{70}$	1160	-
		70.8	3.3E-07	24	1300	300	Melt-added RG	dry	$Fe_{30}Ni_{70}$	1160	-
		85.2	4.5E-07	24	1300	300	Melt-added RG	dry	$Fe_{30}Ni_{70}$	1160	-
		91.6	5.3E-07	24	1300	300	Melt-added RG	dry	$Fe_{30}Ni_{70}$	1160	-

[a]Corrected grain sizes (see text).

[b]FJ: Faul & Jackson (2007)

[c]RG: reagent-derived olivine

Chapter 2

2. Deformation experiments at 1 atm

2.1. Methods

2.1.1. Sample synthesis

I synthesized 8 different aggregates for use in high-temperature deformation tests, which are summarized as: (i) Fe-bearing (Fo90) olivine aggregates with different amounts of pyroxene, (ii) Fe-bearing (Fo90) olivine aggregates doped with different amounts of CaO ± Al_2O_3, and (iii) CaO-doped Fe-free olivine (Table 2-1). All aggregates were prepared by vacuum sintering of nano-sized olivine powder (Koizumi et al., 2010). I followed the same procedure reported in Miyazaki et al. (2013) for the synthesis of Fe-free olivine aggregates. For Fe-bearing olivine aggregates, I added Fe_2O_3 particles with an average particle size of <50 nm (Sigma-Aldrich) to well-mixed nano-sized powders of $Mg(OH)_2$ and colloidal SiO_2 with an average particle size of <50 nm. The resultant olivine has an Fe/(Fe+Mg) molar ratio of 0.9 (i.e., Fo90), comparable to the mineral composition of olivine in the upper mantle. In further samples, powders of $CaCO_3$ with an average particle size of 80 nm and purity of >99.9% and Al_2O_3 with an average particle size of 100 nm and purity of >99.99% (Taimei Chemicals) were added to synthesize CaO ± Al_2O_3-doped aggregates. The powders were well mixed by ball milling for >24 hr using iron-cored plastic balls and ethanol. After drying, the mixed powders were calcined at 1030 ˚C for 3 hr for Fe-free samples in air and 870 to 980˚C for 3 hr for undoped and CaO ± Al_2O_3-doped Fe-bearing samples in Ar + 2% H_2 gas using an alumina tube furnace. I measured the bulk chemistry of the calcined powders on an X-ray fluorescence (XRF) spectrometer (Philips PW-2400) installed at the Earthquake Research Institute at the University of Tokyo. The obtained CaO and Al_2O_3 concentrations corresponded to the concentrations I targeted when mixing the original source powders for the aggregate syntheses to within <10% (Table 2-1).

The calcined powders were then shaped into a cylindrical form using a tungsten carbide die. Vacuum-packed compacts were inserted into a water-medium pressure vessel for cold isostatic pressing (CIP) at 200 MPa for 10 min. Sintering was carried out under a vacuum of 10^{-3}–10^{-2} Pa at temperatures of 1160–1250 ˚C in an alumina tube furnace for 2–20 hr. A flow of Ar + 2% H_2 gas was used during heating to the sintering temperature to prevent sample oxidation. There was no gas flow during the sample cooling, resulting in the formation of a very thin (<10 μm) oxidized layer on the sample surface. This layer disappeared during the deformation experiments, which were conducted in where olivine

was stable. All samples used for deformation tests were shaped as right cylinders with a diameter of ~5 mm and 10-mm height.

The synthesized aggregates all exhibit a relatively homogeneous grain size and foam structure (Fig. 2-1). Intra-granular pores that make up <1 vol% were observed. A pyroxene phase, which fixes the silica activity in the aggregates, was identified in all aggregates under a scanning electron microscope (SEM) (Fig. 2-1). The olivine and pyroxene grains are homogenously distributed. I found at least a few pyroxene grains in samples with nominal pyroxene fractions (f_{px}) of 0 in SEM. I identified enstatite and diopside phases in aggregates with low (0.1–0.3 wt%) and high (5.0 wt%) CaO concentrations, respectively, in X-ray diffraction (XRD, Rigaku SmartLab). The amount of pyroxene in each aggregate was estimated based on the XRF results by assuming that all excess SiO_2 was consumed to form pyroxene (Table 2-1). I refer to the experimental samples hereafter based on f_{px} and/or doping. All undoped samples are Fe-bearing with different f_{px}, so I distinguish these samples based on f_{px}. For example, an undoped Fe-bearing sample containing 30 vol% pyroxene is referred to as the undoped f_{px} = 0.3 sample (Table 2-1). I refer to the doped samples based on the doping conditions. The concentrations of CaO and Al_2O_3 are abbreviated. For example, I refer to the Fo90 olivine sample doped with 0.3 wt% CaO and 0.5 wt% Al_2O_3 and containing 30 vol% pyroxene as the $Ca_{0.3}Al_{0.5}$-doped sample (Table 2-1). The $Ca_{0.3}Al_{0.5}$-doped sample essentially contains 3 times as much CaO and Al_2O_3 as the $Ca_{0.1}Al_{0.2}$-doped sample with the same f_{px}. Only one type of Fe-free aggregate was prepared and used for deformation experiments in this study, so I specifically refer to it as the $Ca_{5.2}$-doped Fe-free sample (Table 2-1).

The olivine grains in doped aggregates tend to have anisotropic shapes (Figs. 2-1d, f, and g) that resemble the tabular grains in Fe-free olivine + diopside aggregates reported by Miyazaki et al. (2013). These grains are characterized by straight grain boundaries that probably lie parallel to major olivine crystallographic planes (i.e., facets). Among samples with the same f_{px}, grain shape anisotropy seems to be stronger in samples with heavier doping. Grain sizes are larger in lower-f_{px} aggregates, which is well explained by a Zener-pinning effect of the secondary phase (pyroxene) on the grain growth of the primary phase (olivine) (Hiraga et al., 2010b). All of the samples exhibit log-normal grain size distributions (Fig. 2-2). I conducted the deformation experiments as well as the aggregate syntheses under dry conditions, so that the aggregates had little chance of incorporating water. I confirmed the “dry” state of the aggregates using Fourier transform infrared spectroscopy (FTIR) (Appendix B).

2.1.2 Deformation experiments

All deformation experiments were conducted at 0.1 MPa pressure using a uniaxial deformation testing machine (Shimadzu AG-X plus) with a box furnace attached, installed at the Earthquake Research Institute, the University of Tokyo (Fig. 2-3). A gas mixture of CO_2 + 5% H_2 was used to maintain the oxygen partial pressure at about one-fifth of that buffered by Ni-NiO (NNO) (Deines et al., 1974). After most of the deformation tests, oxidization of iron wool and the preservation of a metallic appearance in nickel foil that were placed near the sample indicated that this partial pressure was achieved. The experiment on Fe-free sample (KG-60) was conducted in air.

I collected force-displacement-time data every second. A load cell directly attached to the loading rod measured the compressional force and displacement was measured at the crosshead of the apparatus. The load was partially supported by the bellows, which accommodated displacement of an upper arm of the testing machine against an alumina tube (Fig. 2-3); however the bellows stiffness of 4 N/mm was negligible compared to the strength of the aggregates in this study. Thus, the load cell essentially measures the force directly applied to the sample without any intervening dissipating forces, such as friction, and I was able to measure the force and displacement very precisely. The load measurement is accurate to within ±0.4% of the applied force and displacement rates are within ±0.1% of the set speed. The differential stress was determined from the compressive force and surface area changes determined by assuming that compression was uniform and the sample volume was constant. Such assumptions are supported by preservation of the cylindrical shape of the samples and the absence of changes in porosity before and after the experiments. Displacement speeds were converted to strain rates by taking into account the sample length at a given moment during the tests. The strain (ε) was determined from the crosshead displacement as $\varepsilon = -\ln\left(\frac{h}{h_0}\right)$, where ε is the true strain, h_0 is the initial sample height and h is the instantaneous sample height during the experiment. A correction was applied for the stiffness of the deformation rig. I read the strain rate after it became independent with time (i.e., had reached a steady state). The sample cylinder was sandwiched between SiC discs (ϕ = 25 × 10-mm thick). I placed alumina discs (ϕ = 25 × 4 mm) between the SiC discs and SiC rods (pistons) (ϕ = 40 mm) to avoid direct contact between them (Fig. 2-3). No reaction between the SiC discs and the samples was detected. Temperature was measured using an R-type thermocouple (Pt and Pt-Rh) located 1–2 mm from the sample. Temperature was kept constant within 2˚C during the experiments.

Two types of stepped tests were conducted: (i) deformation tests with a stepped load

(I refer to these as stepped-load tests hereafter) at constant temperature, and (ii) tests with a stepped temperature at constant loads (referred to as stepped-temperature tests hereafter). One experiment (KH-71) was conducted at a constant temperature (1250˚C) with a stepped displacement rate instead of changing load, and I regard it as a stepped-load test in the *Results* section. I changed load and/or temperature after achieving a strain of around ε = 0.01 during the tests. The total ε achieved in most experiments is ~0.1, while an ε of 0.7 was achieved for KH-71, which was aimed at examining the development of olivine CPO due to deformation as well as mechanical properties (Table 2-2). Typical load and displacement versus time data for a stepped-load test are presented in Fig. 2-4. Most experiments started by holding the samples without load at the highest temperatures applied in subsequent deformation tests. This annealing step performed with different durations allowed us to conduct experiments on samples with various grain sizes and little grain growth during the tests.

Only stepped-temperature tests were conducted for Fe-free aggregates because stress-strain rate relationships for this material have already be reported elsewhere (Miyazaki et al., 2013; Maruyama & Hiraga, 2017a), where *n* exhibited ~1 over a wide range of stress and temperature (i.e., 10–100 MPa and 1200–1350˚C). These studies used aggregates with different grain sizes for experiments at different temperatures, which prevented us from obtaining a reliable value of the activation energy from the experimental data. By performing stepped-temperature tests in this study on the same material used by Miyazaki et al. (2013), I intended to measure the temperature dependence of strain rate at a constant grain size and stress.

2.1.3. Annealing experiments

I conducted annealing experiments separately from the deformation tests to determine the initial (starting) grain sizes (d_{ini}) in the deformation experiments and to constrain T_{s} of each type of aggregate used in this study. The aggregates were annealed at the same temperatures and durations (≥2 h) that were applied before loading during the deformation experiments and quenched rapidly. We judged the presence or absence of a melt phase in the aggregates at elevated temperatures based on the sample microstructures.

2.1.4. Sample characterization

Sections of all samples were examined in an SEM equipped with a field emission gun (JEOL-7001F installed at the Nano-Manufacturing Institute, the University of Tokyo), particularly for measuring grain sizes and melt fractions in the samples. The deformed samples were sectioned parallel to the direction of compression for microstructural

characterization. A 15-minute mechanochemical polishing step with colloidal silica was performed in order to observe melt (glass) in the samples. The melt fraction was determined based on its area fraction in SEM images taken in secondary electron imaging (SEI) mode. Grain size was analyzed in sections that were thermally etched after polishing. Etching temperatures were >50˚C lower than the highest temperatures experienced by the sample and were held for 0.5 h under a controlled atmosphere; this enabled the sample microstructures to become visible without being modified during etching. I measured the cross-sectional area of >100 olivine grains, which is large enough to determine an average grain size in each sample (Fig. 2-5), in SEM-SEI images for each sample using ImageJ software (NIH). The diameter of each grain was estimated from the value of the equivalent-circle diameter, i.e., $2\sqrt{S_i/\pi}$ (where S_i is the area of *i*-th grain). The number-weighted diameter corresponds to the grain size in this study. For some aggregates, I analyzed the frequency of the diameter normalized by the grain size (APPENDIX C). I consider the olivine grain size to represent the grain size of the samples based on the assumption of olivine-controlled bulk deformation. In *chapter 3*, I will examine creep data from different research groups in which grain sizes were obtained by the line-intercept method. I discuss different methods of grain sizes measurement in APPENDIX D.

Some deformed samples exhibited larger grain sizes after deformation than beforehand. This grain growth may account for strain hardening during deformation. The growth is expected to follow the combined static and dynamic grain growth law of Holm et al. (1977):

$$d_\varepsilon = (kt + {d_{\mathrm{ini}}}^m)^{1/m} \cdot \exp(\alpha\varepsilon), \qquad (2\text{-}1)$$

where d_ε and d_{ini} are the grain sizes of the deformed and initial samples, t is the duration of grain growth, k is the grain growth coefficient under static conditions, m is the grain growth exponent, which is assumed to be 4, ε is strain, and α is the dynamic grain growth constant. The applicability of this law has been demonstrated elsewhere (e.g., Hiraga et al., 2010a, b; Tasaka et al., 2013; Nakakoji et al., 2018). I gave precedence to the measured grain sizes by leaving the value of α as a variable defined as $\alpha = \frac{1}{\varepsilon}\ln\frac{d_\varepsilon}{d_s}$, where d_s is the grain size of the statically annealed (reference) sample. For stepped-load experiments, I used Eq. (2-1) to adjust the values of α and k to fit the initial, reference, and final grain sizes (d_{fin}) observed after deformation experiments (Tables 2-2 and 2-3). Then the grain sizes of deformed samples were estimated using the values of α and k.

For stepped-temperature tests, the grain size of deformed samples was simply estimated as $d_\varepsilon = d_{\mathrm{ini}} \cdot \exp(\alpha\varepsilon)$ based on the observed lack of grain growth in the reference samples (Table 2-3).

Crystallographic orientations of olivine grains were measured on the mechanochemically polished (for 0.5 hr) surfaces of deformed samples. Electron backscatter diffraction (EBSD) data was obtained using a JEOL JSM-7000F SEM equipped with a Digi View digital EBSD camera. The Kikuchi bands of the diffraction patterns were indexed automatically using the OIM7 (TSL/EDAX) software package. The crystallographic orientation data were viewed in lower hemisphere projections.

2.2. Results

2.2.1. Microstructures

2.2.1.1 Deformed samples

The microstructural characteristics identified in the starting materials, including (i) intra-granular pores of <1 vol%, (ii) homogeneous grain size and foam structure, and (iii) homogenous distributions of olivine and pyroxene grains (Fig. 2-1), were essentially preserved after the deformation tests (Fig. 2-6). The grain sizes of most deformed samples are comparable to their starting materials as well as their reference samples, although some samples exhibited grain growth during the experiments (Tables 2-2 and 2-3). No change in grain shape was detected, however the long axes of olivine grains were found to have aligned perpendicularly to the compression axis in the highly deformed $Ca_{0.3}Al_{0.5}$-doped sample (KH-71) (Fig. 2-6f). I analyzed the CPO of olivine specifically in this sample and found a *b*-axis ([010]) alignment toward the compression axis (// Z direction), and *a*- and *c*- girdles in the X-Y plane (Fig. 2-6h).

2.2.1.2. Occurrence of melting

I examined the presence and absence of a melt phase (glass) in sample sections where only mechanochemical polishing was applied (Fig. 2-7). The inter-granular melt is easily distinguished from pores by its much lower dihedral angle (<60°). The melt tends to occur at triple-junctions of olivine grains. The $Ca_{0.1}Al_{0.1}$-doped aggregate deformed at 1350˚C contains melt, while the same aggregate is melt-free at ≤1300˚C (Fig. 2-7a). The $Ca_{0.1}Al_{0.2}$-doped aggregate is melt-free even at 1350˚C (Fig. 2-7b). The $Ca_{0.3}Al_{0.5}$-doped aggregate contains melt at ≥1250˚C, and the melt fraction increases with temperature (Fig. 2-7c). The $Ca_{5.0}$-doped aggregate deformed at 1350˚C contains melt, but is melt-free at ≤1300˚C. Based on these observations, we made estimates of T_s for each aggregate, which are listed in Table 2-1. Many melt-free triple junctions exist even in samples

identified as containing the largest amount of melt (Fig. 2-7c).

2.2.2. Deformation experiments

2.2.2.1. Stepped-load tests

The σ and $\dot{\varepsilon}$ results obtained from different types of aggregates are plotted on a log-log field in Fig. 2-8. A positive correlation is found for all samples. The numbers beside each point correspond to the order of load (stress) steps applied in single tests. Normally, I increased stress stepwise from 5–10 MPa to 90–140 MPa and then decreased stress. I obtained the same $\dot{\varepsilon}$ at the same σ for different steps in most cases, although I occasionally obtained lower $\dot{\varepsilon}$ values in later steps. Such strain hardening occurred in samples that exhibited large grain growth during the tests. For example, $\dot{\varepsilon}$ decreased from 1.23×10^{-5} (step 1) to 4.61×10^{-6} /sec (step 5) at a stress of 100 MPa during test KH-152, where grain size increased from 1.7 to 2.5 μm (Fig. 2-8a) (Table 2-2). On the basis of a power-law relationship of the type $\dot{\varepsilon} \propto \sigma^n$ (Eq. (1-1)), I observed an apparent stress exponent, n_{app} of 1–2 in all experiments. Overall, the results from undoped samples show larger n_{app} values than the results from doped samples (Fig. 2-8).

2.2.2.2. Stepped-temperature tests

The $\dot{\varepsilon}$ values obtained during stepped-temperature tests are plotted in Arrhenius space in Fig. 2-9 and listed in Table 2-3. All tests on undoped samples were conducted at a constant stress of 100 MPa (Fig. 2-9a). For doped samples, we generally applied a σ of either 50 or 100 MPa (and occasionally 10 or 40 MPa) during single tests. The stress values are indicated by the symbol styles (Fig. 2-9b). The order of temperature steps applied in each test correspond to the numbers beside each point. I obtained the same $\dot{\varepsilon}$ in different steps with the same temperatures in single tests on undoped samples, which is consistent with the minor changes in grain size before and after the tests in these samples (Fig. 2-9a). A small decrease in $\dot{\varepsilon}$ in later steps at the same temperatures and σ was found for some doped samples, specifically those that exhibited significant grain growth during tests (Fig. 2-9b). For example, $\dot{\varepsilon}$ decreased from 9.10×10^{-6} (at step 2) to 4.55×10^{-6} /sec (at step 16) when a stress of 50 MPa was repeated in test KH-142, in which grain size changed from 0.67 to 0.97 μm (Fig. 2-9b, Table 2-3).

Overall, $\dot{\varepsilon}$ increases with increasing temperature following an Arrhenius relationship. The stepped-temperature tests on undoped samples were conducted at a constant σ; thus, the $\dot{\varepsilon}$ of each sample can be reasonably fit by an Arrhenius relationship where the slope gives a value for Q (Eq. (1-1)). We obtained Q values of 530 ± 20, 480 ± 10, and 464 ± 6 kJ/mol for samples with f_{px} = 0, f_{px} = 0.1, and f_{px} = 0.3, respectively, based on

least-squares fits (Fig. 2-9a).

2.3. Analytical results

2.3.1. Stress dependence of strain rate

I detected grain growth in some deformation experiments (Tables 2-2 and 2-3), which likely explains the hardening observed at the same stress levels repeated later in the deformation tests. To minimize grain growth effects on the extracted stress exponent (i.e., *n* in Eq. (1-1)), I compared two sets of (σ_i, $\dot{\varepsilon}_i$) and (σ_{i+1}, $\dot{\varepsilon}_{i+1}$) values from stepped-load tests, which were obtained before and after changing loads, respectively (Fig. 2-8) (Nakakoji et al., 2018). *n* values are usually obtained by fitting σ and $\dot{\varepsilon}$ from more than 2 points over a relatively wide stress range to reduce the effect of uncertainty in $\dot{\varepsilon}$ on n; however, I gave precedence to determining changes in the stress exponent with stress rather than determining its precise value. I obtained this apparent stress exponent, n_{app} from:

$$n_{\mathrm{app}} = \frac{\log \dot{\varepsilon}_{i+1} - \log \dot{\varepsilon}_i}{\log \sigma_{i+1} - \log \sigma_i}, \qquad (2\text{-}2)$$

which is plotted against $\bar{\sigma}$ (= $\sqrt{\sigma_i \sigma_{i+1}}$) in Fig. 2-10. The step numbers of the analyzed data pairs for the undoped f_{px} = 0.1 sample at 1300˚C (KH-54) used to obtain each n_{app} are shown beside each point in the figure. n_{app} values determined from both the increasing and decreasing σ portions of each stepped-stress test are comparable at the same σ. Overall, n_{app} values are larger (up to 3) at low σ and smaller at higher temperatures and in doped samples. The value gradually decreases with increasing σ, while it reaches a nearly constant value of ~1 in a stress range of >20-100 MPa, depending on the sample and temperature.

2.3.2. Grain size dependence of strain rate

The observation that n_{app} approaches ~1 at around 100 MPa for all samples (Fig. 2-10) indicates that all samples deformed by a Newtonian creep mechanism at this stress level. The $\dot{\varepsilon}$ values obtained for different grain sizes at 100 MPa and a given temperature are compared in Figs. 2-11a and b. Here we analyze the results of both stepped-load and stepped-temperature tests based on Eq. (1-1) with $p_{\mathrm{app}} \equiv -\left(\frac{\partial \log \dot{\varepsilon}}{\partial \log d}\right)_{\sigma,T}$. Despite the limited range in grain size, we can describe $\dot{\varepsilon}$ of the undoped f_{px} = 0 samples at 1250˚C with a p_{app} of ~3 (Fig. 2-11a; Table 2-4). If I include $\dot{\varepsilon}$ data for the undoped f_{px} = 0.1

samples at the same temperature of 1250˚C, I find that all data at 1250˚C are well represented by a single curve with a p_{app} value of 3 (Table 2-4). Adding the data for the undoped f_{px} = 0.3 samples further supports this value of p_{app}, so I interpret the $\dot{\varepsilon}$ data from other temperatures with the a p_{app} of 3 (Fig. 2-11a). The limited grain size variations in doped samples make it difficult to determine their p_{app} values, although the $\dot{\varepsilon}$ data at 1150˚C also indicate the same p_{app} value of 3 (Fig. 2-11b). Overall, the $\dot{\varepsilon}$ at 100 MPa indicate sample deformation dominated by grain-boundary diffusion creep.

The increases in n_{app} values with decreasing σ below 50 MPa (Fig. 2-10) indicate a transition from grain-boundary diffusion creep to a different deformation process; hence, p_{app} likely changes. $\dot{\varepsilon}$ for undoped samples at 1250˚C is plotted against grain size in Fig. 2-11c and line-fits through the $\dot{\varepsilon}$ values for each σ indicate p_{app}. The $\dot{\varepsilon}$ data at 50 MPa are well explained by a p_{app} value of ~3, similar to that found for σ = 100 MPa, while the $\dot{\varepsilon}$ at a σ of 20 MPa are best explained by a p_{app} of ~2.5. The $\dot{\varepsilon}$ at σ of 10 MPa are best explained by an even smaller p_{app} value despite its large uncertainty.

2.3.3. Temperature dependence of strain rate

Q values are usually obtained by fitting plots of $1/T$ versus $\ln\dot{\varepsilon}$ with more than 2 points from a relatively wide temperature range to reduce the effect of uncertainties in $\dot{\varepsilon}$ on Q. However, in the analysis of temperature-stepped tests on undoped samples (Fig. 2-9a), the results of the n_{app} analyses (Fig. 2-10) support the determination of Q based on two sets of (T_i, $\dot{\varepsilon}_i$) and (T_{i+1}, $\dot{\varepsilon}_{i+1}$) values obtained before and after changing temperature, respectively (Fig. 2-9). This comparison is expected to characterize the temperature dependence of Q. I obtained an apparent activation energy, Q_{app} from:

$$Q_{\mathrm{app}} = -\mathrm{R} \cdot \left(\frac{\ln \dot{\varepsilon}_{i+1} - \ln \dot{\varepsilon}_i}{{T_{i+1}}^{-1} - {T_i}^{-1}}\right) \qquad (2\text{-}3)$$

and plotted it against $10^4 \times (1/\bar{T})$, where $1/\bar{T} = 0.5 \times \left(\frac{1}{T_i} + \frac{1}{T_{i+1}}\right)$, in Fig. 2-12. The step numbers of the analyzed data pairs, i.e., i-$i+1$, are shown beside each point. The Q_{app} values from undoped f_{px} = 0.1 and 0.3 samples plot well within the range of 445–495 kJ/mol and have no temperature dependence (Fig. 2-12). The mean value of Q_{app} is 470 kJ/mol, which is consistent with the Q value obtained by fitting the entire $1/T$ vs. $\ln\dot{\varepsilon}$ data set (Fig. 2-9). We obtained larger Q_{app} values for the f_{px} = 0 sample in the range 510–570 kJ/mol, with relatively large uncertainties.

2.3.4. Flow law parameters

The tests, especially KH-141 and KH-148, were conducted well within the range of conditions where $n_{\mathrm{app}} \approx 1$ and $p_{\mathrm{app}} \approx 3$ (Figs. 2-10 and 2-11), which is consistent with the observation of temperature-independent Q_{app} (Fig. 2-12). These combined results indicate that $Q_{\mathrm{app}} = Q$ for grain-boundary diffusion creep. Thus, I determined a Q_{diff} of 470 kJ/mol, which describes the results of both KH-141 and KH-148 (Figs. 2-9a and 2-12), and the p_{diff} value of 3 (Fig. 2-11a) in Eq. (1-5) and used it to find the best A_{diff} reference value for diffusion creep of olivine. As I discuss below, I attribute the larger Q_{app} values from experiment KH-149 (Fig. 2-12) to a small contribution from dislocation process to $\dot{\varepsilon}$ and I decided to exclude that result from the flow law parameter determinations. I obtained similar A_{diff} values of 1.12×10^{10} and 1.70×10^{10} μm^3·MPa^{-1}·s^{-1} from the results of KH-141 and KH-148, respectively. For future applications of my established constitutive equation to Earth's mantle in *chapter 4*, I simply use an A_{diff} value of 1.12×10^{10} μm^3·MPa^{-1}·s^{-1} determined from aggregates with an f_{px} comparable to that in the mantle.

Next, I find the A_{int} and Q_{int} values that best explain the data by minimizing $\sum_1^N \left[\log\left(\frac{\dot{\varepsilon}_{\mathrm{cal}}}{\dot{\varepsilon}_{\mathrm{obs}}}\right)\right]^2$, where $\dot{\varepsilon}_{\mathrm{cal}}$ is the calculated strain rate based on Eq. (1-3) using the flow law parameters for diffusion creep determined above and the σ, d, and T values at which $\dot{\varepsilon}_{\mathrm{obs}}$ was obtained. I imposed a value of $n_{\mathrm{int}} = 3$ based on the results of the n_{app} analysis (Fig. 2-10a) and theoretical predictions (Ashby, 1969; Burton, 1972; Arzt et al., 1983). A total of 90 ($= N$) mechanical data points for undoped samples were analyzed to obtain A_{int} and Q_{int} values of 2.12×10^{12} μm·MPa^{-3}·s^{-1} and 610 kJ/mol, respectively, that best explain the data. Plotted curves of Eq. (1-3) using the determined flow law parameters and the experimental conditions (i.e., d and T) for each stepped-load test correspond to the solid lines in Figs. 2-8a–c, which reproduce all of the experimental data well.

Ideally, I would determine flow law parameters from a single test, since this eliminates sample-to-sample and test-to-test variations that are often difficult to express in the experimental uncertainties (Korenaga & Karato, 2008). I can obtain mechanical data by changing one of the factors controlling creep rate, such as temperature in the stepped-temperature tests, where grain size is essentially kept constant (Fig. 2-9a). This approach differs from the previous Bayesian analysis to determine flow law parameters (Nakakoji et al., 2018) where >600 experimental data points for different grain sizes, stresses, and temperatures were analyzed at the same time. This statistical approach was essential due to variations in multiple creep rate-controlling factors during the deformation tests.

All $(\sigma, \dot{\varepsilon})$ values for undoped samples were transformed to $(\sigma_0,\ \dot{\varepsilon}_0)$ based on Eq. (1-8). The $(\sigma^{*\mathrm{ref}}, \dot{\varepsilon}^{*\mathrm{ref}})$ data are calculated from Eqs. (1-6) and (1-7) by substituting the d and T values at which each $(\sigma, \dot{\varepsilon})$ was acquired. I used the flow law parameters (i.e., A_{int}, A_{diff}, Q_{int}, Q_{diff}, n_{int}, and p_{diff}) as determined above. All calculated $(\sigma_0,\ \dot{\varepsilon}_0)$ are plotted in Fig. 2-13. The calculated $(\sigma_0,\ \dot{\varepsilon}_0)$ follow the predicted curve of Eq. (1-9) well with an n_{int} of 3:

$$\dot{\varepsilon}_0 = [(\sigma_0{}^3)^{-1} + (\sigma_0)^{-1}]^{-1} \qquad (2\text{-}4)$$

with misfits of a factor of <2. The result reinforces the validity of my established reference constitutive equation for olivine creep.

2.3.5. Ca and Al (doping) effects on creep rate

To investigate doping effects on creep rates, each $(\sigma, \dot{\varepsilon})$ from stepped-load tests on doped samples was normalized by $(\sigma^{*\mathrm{ref}},\ \dot{\varepsilon}^{*\mathrm{ref}})$, which was calculated from Eqs. (1-6) and (1-7) with the d and T values at which each $(\sigma, \dot{\varepsilon})$ was acquired. I refer to such normalized $(\sigma, \dot{\varepsilon})$ values for the doped samples as $(\sigma_{0\_\mathrm{ref}}^{\mathrm{doped}},\ \dot{\varepsilon}_{0\_\mathrm{ref}}^{\mathrm{doped}})$ hereafter, and they are plotted in σ_0 - $\dot{\varepsilon}_0$ space (Fig. 2-14a). The $(\sigma_{0\_\mathrm{ref}}^{\mathrm{doped}},\ \dot{\varepsilon}_{0\_\mathrm{ref}}^{\mathrm{doped}})$ data exhibit a power-law-like relationship at low σ_0 and a Newtonian-like relationship at high σ_0, as with the undoped samples. Overall, the $(\sigma_{0\_\mathrm{ref}}^{\mathrm{doped}},\ \dot{\varepsilon}_{0\_\mathrm{ref}}^{\mathrm{doped}})$ data plot either along the reference curve (Eq. (2-4)) or above it.

I introduced the term χ to describe the change in $\dot{\varepsilon}$ due to doping in normalized space:

$$\chi \equiv \frac{\dot{\varepsilon}_{0\_\mathrm{ref}}^{\mathrm{doped}}}{\dot{\varepsilon}_0\left(\sigma_{0\_\mathrm{ref}}^{\mathrm{doped}}\right)} = \dot{\varepsilon}_{0\_\mathrm{ref}}^{\mathrm{doped}} \cdot \left[\left(\sigma_{0\_\mathrm{ref}}^{\mathrm{doped}}\right)^{-3} + \left(\sigma_{0\_\mathrm{ref}}^{\mathrm{doped}}\right)^{-1}\right]. \qquad (2\text{-}5)$$

The χ value represents the relative creep rate of a doped sample to that of an undoped (reference) sample at the same experimental conditions (i.e., grain size, temperature, and stress). The calculated χ values based on Eq. (2-5) are plotted against σ_0 in Fig. 2-14b. Most χ values are ≥1. χ exhibits large values at low σ_0, while it decreases with increasing σ_0. Above certain values of σ_0, the χ values become independent of σ_0, reaching a constant value that is larger for results from the higher-temperature

experiments. At a given temperature, the χ values from the $Ca_{0.3}Al_{0.5}$-doped sample are systematically larger than those from the $Ca_{0.1}Al_{0.2}$-doped sample. Considering that both samples have the same f_{px}, the χ value appears to be a function of the amount of doping as well as temperature and stress.

Similarly, Fig. 2-15a contains a plot of ($\sigma_{0\_ref}^{doped}$, $\dot{\varepsilon}_{0\_ref}^{doped}$) that were converted from the (σ, $\dot{\varepsilon}$) data of stepped-temperature tests. In the analysis, I excluded data for steps 13 and 14 in KH-142, which may contain disequilibrium melt effects on the mechanical data. Most of the data plot either on the reference curve or above it. The calculated χ values for these experiments based on Eq. (2-5) are plotted in Fig. 2-15b. Most χ values are ≥1 and increase with increasing temperature. The ($\sigma_{0\_ref}^{doped}$, $\dot{\varepsilon}_{0\_ref}^{doped}$) and χ values from Fe-free samples are included in Figs. 2-15a and b. These values are calculated using the reference olivine creep rates determined for Fe-bearing olivine, assuming that Fe has little effect on olivine creep rates. I will discuss this point later in *section 2.4.2.2.*

2.4. Discussion

2.4.1. Samples and their states

I have analyzed the mechanical data from the samples on the basis of their doping properties (Figs. 2-8 to 2-11, and 2-13 to 2-15); however, there are other differences in the samples and their states, which are discussed along with their effects on creep rate below.

2.4.1.1. Oxygen fugacity

Because the same flowing CO_2/H_2 gas mixture was used for all experiments, the oxygen fugacity (f_{O_2}) varied with the experimental temperature; i.e., from 10^{-5} Pa at 1100˚C to 10^{-2} Pa at 1300˚C in this study (Deines et al., 1974). A previous experimental study of olivine dislocation creep reported the relationship $\dot{\varepsilon} \propto {f_{O_2}}^{1/5}$ (Keefner et al., 2011). The f_{O_2} at a constant gas ratio changes with temperature with an Arrhenius behavior such that the same oxygen fugacity exponent of 1/5 for diffusion creep predicts a reduction in Q_{diff} of ~140 kJ/mol at a fixed f_{O_2}. This result seems to account for the larger Q_{diff} value I obtained relative to the value reported in previous studies (i.e., Q_{diff} of ~315 kJ/mol by Hirth & Kohlstedt, 1995a). Further results will be discussed in *chapter 3*. However, the previously reported Q_{diff} value should also include fugacity effects in a similar manner due to the use of a Ni/NiO buffer in the experiments (Hirth & Kohlstedt, 1995a). The Fe^{2+}/Fe^{3+} ratio in olivine changes with f_{O_2}, resulting in changes in the concentration of

point defects, and hence, possibly creep rate. As I show later, my reference olivine diffusion creep compares well with the creep of Fe-free olivine in air (Nakakoji et al., 2018), which has an f_{O_2} more than 6 orders of magnitude larger than the f_{O_2} set by CO_2/H_2 gas in this study. This result is somewhat unexpected, but it indicates that f_{O_2} has little effect on olivine diffusion creep and hence Q_{diff}. Among the constituent elements of the undoped and doped samples, only Fe can change its valence state within the experimental f_{O_2} range. Having the same Fe concentrations in undoped and doped samples predicts similar responses of their creep rates to f_{O_2}. My measurement of doping effects on olivine creep is based on a comparison of $\dot{\varepsilon}$ in undoped and doped samples at the same experimental conditions (Eq. (2-5)); thus, the result will not change whether the creep rate depends on f_{O_2} or not.

2.4.1.2. Presence of pyroxene

The p_{app} value of 3 explains not only the grain-size dependence of $\dot{\varepsilon}$ in the f_{px} = 0 samples, but also for the f_{px} = 0.1 and 0.3 samples at 100 MPa (Fig. 2-11a). Since a p_{app} value of 3 is well supported by theoretical models of grain-boundary diffusion creep (e.g., Coble, 1963), the observation indicates that pyroxene has little effect on the creep rates in my samples. This is the same conclusion reached in the previous studies of creep in olivine aggregates with f_{px} varying from 0 to 0.4 (Tasaka et al., 2013; Nakakoji et al., 2018), which were synthesized in the same way (Koizumi et al., 2010). As a result, my established reference constitutive equation for olivine creep reproduces the mechanical data of samples with different f_{px} equally well (Figs. 2-8a–c and 2-13). My conclusion differs from the recent study by Zhao et al. (2019), who interpreted their experimental olivine + clinopyroxene creep results in terms of weakening due to the presence of interphase boundaries.

2.4.1.3. Presence of melt

Based on the estimated T_{s} for each aggregate (Table 2-1), only the $Ca_{0.3}Al_{0.5}$-doped sample at T ≥1250˚C was deformed in the presence of melt in this study. The $\dot{\varepsilon}$ values above T_{s} are not particularly large, and follow the trend of temperature dependence for $\dot{\varepsilon}$ below T_{s} (Fig. 2-9b). A similar temperature dependence was observed for other doped aggregates that were free from melting, indicating that melt has little effect on $\dot{\varepsilon}$. It was once predicted that the formation of an amount of melt as small as 0.1 vol%, comparable to the fraction in the doped sample at >T_{s}, would increase grain-boundary diffusion creep rates by a factor of ~5 (Takei & Holtzman, 2009). However, recent theoretical modeling of grain-boundary diffusion creep with and without melt, which incorporates

collaborative diffusion from neighboring grains, shows a much lower factor of 1.4 (Rudge, 2018). Recent creep experiments on analog materials of peridotite with well-controlled melt fractions support the finding of negligible weakening due to the formation of up to 2 vol% melt during grain-boundary diffusion creep (Yamauchi & Takei, 2016). Instead, they found a pre-melting effect on $\dot{\varepsilon}$ starting from 0.94×T_s, which continues above T_s. The sample weakening due to pre-melting is well represented by an increment of Q_{diff}, which can be large enough to mask the sample weakening due to the formation of partial melt. The $\dot{\varepsilon}$ values of doped samples seemingly respond to temperature in the same manner, which will be discussed later.

2.4.1.4. Chemistry of grain boundaries

In a state of chemical equilibrium, incompatible elements such as Ca and Al in olivine segregate at grain boundaries. This process is driven by ionic size and charge differences between the host ions and the solutes (Hiraga et al., 2004; Hiraga & Kohlstedt, 2007). The Fe concentration is constant across the olivine lattice and at grain boundaries, but Mg depletion at the boundaries indicates the occurrence of Mg↔Ca exchange and/or Al substitution at the grain boundaries (Hiraga et al., 2004). Thus, my doped and undoped aggregates, irrespective of their Fe content, can be thought of as aggregates with and without grain-boundary segregation, respectively. The equilibrium segregation is a result of element partitioning between grain boundaries and the lattice, which predicts stronger segregation for larger amounts of doping at a fixed grain size and mineral mode. Grain growth assists in forming grains with equilibrium concentration of dopants, and hence, grain boundaries with the equilibrium concentrations (Hiraga & Kohlstedt, 2007). Significant grain growth must have occurred during the sample synthesis where the sintering started and ended with <100 nm particle sizes and ~1 μm grain sizes, respectively. I consider grain boundaries with equilibrium concentrations in the initial sintered samples and even in the deformed samples. Grain boundaries are rapid diffusion paths and connected to pyroxenes which are the major host for Ca and Al. This situation is likely to result in grain boundaries with equilibrium concentrations of Ca and Al during the deformation. Such point is supported from the strain rates primarily determined by temperature without the influence of temperature history in stepped-temperature experiments (e.g. step 1 and 3 in KH-151 in Fig. 2-9; see Fig. F2f).

2.4.2. Deformation mechanisms

2.4.2.1. Combination of multiple deformation processes

The observed convex shape of the $\log\sigma$ and $\log\dot{\varepsilon}$ relationships (Fig. 2-8), in which the value of n_{app} decreases from ~3 to ~1 with increasing σ (Fig. 2-10), are well described by strain rates determined by a combination of power-law creep and Newtonian creep mechanisms (Fig. 1-2), which are connected sequentially (Eq. (1-3)). The combined occurrence of these mechanisms is consistent with the previous explanations for the deformation of Fe-free olivine aggregates at low to intermediate stress (Nakakoji et al., 2018). A similar convex-shaped $\log\sigma$ and $\log\dot{\varepsilon}$ relationship can also be produced by Newtonian creep with a threshold stress (σ_{th}), i.e., $\dot{\varepsilon} \propto (\sigma - \sigma_{\mathrm{th}})$; however, it predicts $n_{\mathrm{app}} \rightarrow \infty$ with decreasing σ (Nakakoji et al., 2018), which is not supported by my results (Fig. 2-10).

2.4.2.2. Grain-boundary diffusion creep

The microstructural observations include: (i) essentially no difference in grain shape before and after deformation (Figs. 2-1 and 2-6), (ii) dynamic grain growth (Tables 2-2 and 2-3), and (iii) CPO development in samples with anisotropic grain shape (Fig. 2-6h). These features are all consistent with previously identified microstructural characteristics of Fe-free olivine aggregates that exhibited superplasticity (Hiraga et al., 2010a; Miyazaki et al., 2013). It was concluded in earlier studies that Fe-free olivine aggregates deformed by a grain-boundary diffusion creep mechanism at intermediate stresses (σ of 90 to 160 MPa) (Nakakoji et al., 2018). Due to the large contribution of GBS to the total strain during creep (Maruyama & Hiraga, 2017a), which resulted in superplasticity of the aggregates, the deformation mechanism is perhaps more strictly referred to as grain-boundary-diffusion controlled (accommodated) GBS creep. However, as Maruyama & Hiraga (2017a) pointed out, there is no experimental evidence that necessarily indicates the presence of both diffusion creep and diffusion controlled-GBS creep mechanisms (Rust & Todd, 2011).

In addition to the microstructural characteristics, the n_{app} and p_{app} values I obtained of 1 and 3, respectively, (Figs. 2-10 and 2-11) support grain-boundary diffusion creep as the main deformation mechanism in Fe-bearing samples at σ of 50–100 MPa, which is essentially the same conclusion drawn for Fe-free aggregates in the previous studies (Tasaka et al., 2013; Nakakoji et al., 2018). Thus, it was considered reasonable to assume n and p values of 1 and 3, respectively, to determine other flow law parameters of olivine diffusion creep (Eq. (1-5)). Based on the analytical results (*section 2.3.4*), I propose a constitutive equation for grain-boundary diffusion creep of undoped (reference)

olivine aggregates:

$$\dot{\varepsilon}_{\mathrm{diff}}^{\mathrm{ref}} = 1.12 \times 10^{10}\ \mu\mathrm{m}^3/\mathrm{MPa/s} \cdot (\sigma/d^3) \cdot \exp\left(-\frac{470\ \mathrm{kJ/mol}}{\mathrm{R}T}\right). \quad (2\text{-}6)$$

I compare this equation with that for Fe-free aggregates established by Nakakoji et al. (2018) in Fig. 2-16. It should be noted that the grain size reported in Nakakoji et al. (2018) corresponds to a three-dimensional ($= d_{3\mathrm{D}}$) parameter; thus, I converted their reported $d_{3\mathrm{D}}$ to a two-dimensional grain size as defined in this study using the relationship $d_{3\mathrm{D}} = 1.77 \times d$ (see Nakakoji et al., 2018). Fe-free and Fe-bearing olivine are compared by plotting $\dot{\varepsilon}$ at a σ of 100 MPa and d of 1 μm in Arrhenius space (Fig. 2-16), which reveals them to be essentially the same throughout the experimental temperature range. The prediction of similar flow strengths for Fe-free and Fe-bearing olivine during grain-size-sensitive creep was speculated on in the previous study (Tasaka et al., 2013), which compared the strengths of Fe-free olivine and reagent-derived Fe-bearing olivine (Faul & Jackson, 2007).

Diffusion of the slowest constituent ion in a mineral is generally considered to control its creep rate. Si is the slowest ion for both grain-boundary and lattice diffusion in olivine (Dohmen et al., 2002; Farver & Yund, 2000; Fei et al., 2012, 2016). I compare my results with creep rates predicted from Si-self diffusion at grain boundaries in Fe-free olivine aggregates (Fei et al., 2016) that were synthesized in our laboratory (Koizumi et al., 2010). The reported values correspond to a grain-boundary width (δ) × grain-boundary diffusivity of Si (i.e., $\delta D_{\mathrm{GB\_Si}}$) that constitutes a grain-boundary diffusion creep law (Coble, 1963; Raj & Ashby, 1971; Ashby & Verrall, 1973; Ashby et al., 1978; Spingarn & Nix, 1978; Rudge, 2018) of the form

$$\dot{\varepsilon} = A'_{\mathrm{GB\_diff}} \frac{\sigma\beta(\delta D_{\mathrm{GB\_Si}})V_{\mathrm{m}}}{d^3 \mathrm{R}T}. \quad (2\text{-}7)$$

Here, β is a coefficient that describes a compound effect on self-diffusivity and is 7 for Si (see Nakakoji et al., 2018), and the molar volume, V_{m} is 4.36×10^{-5} m^3/mol for Fe-free olivine (Holland & Powell, 2011). A'_{diff} is a geometrical factor that varies by a factor of ~10 among models of diffusion creep (Coble, 1963; Raj & Ashby, 1971; Ashby & Verrall, 1973; Ashby et al., 1978; Spingarn & Nix, 1978; Rudge, 2018). Using the A'_{diff} values from classical diffusion creep models (Nabbaro, 1948; Herring, 1950; Coble, 1963) in Eq. (2-7) is known to underestimate $\dot{\varepsilon}_{\mathrm{diff}}$; instead, multiplying this A'_{diff} value

by ~10 gives reasonable $\dot{\varepsilon}_{\mathrm{diff}}$ values compared to those observed in various materials, including metals and ceramics (Wang, 2000). Here, I use $A'_{\mathrm{GB\_diff}}$ of 86, which was derived for a 2D grain size (see APPENDIX D), in Eq. (2-7) to calculate $\dot{\varepsilon}_{\mathrm{diff}}$ based on reported $\delta D_{\mathrm{GB\_Si}}$ values (Fei et al., 2016). The results are plotted in Fig. 2-16 and are in good agreement with $\dot{\varepsilon}$ determined from the creep experiments.

2.4.2.3. Interface-controlled creep

Power-law creep is commonly interpreted in terms of intragranular dislocation processes in Earth science. The required σ of >80 MPa for a Frank-Read source to produce lattice dislocations in ~1-μm-size olivine has been calculated elsewhere (Maruyama & Hiraga, 2017a; Nakakoji et al., 2018). This calculation is consistent with the appearance of power-law creep at σ>160 MPa in Fe-free olivine aggregates (Nakakoji et al., 2018). Maruyama and Hiraga (2017a) recently showed direct evidence of intra-granular deformation in sample surfaces of Fe-free aggregates where deformation was only identified in relatively large grains, >3 μm, at a σ of >80 MPa (see Fig. 8c in their paper). The larger Q_{app} values of 510–570 kJ/mol obtained from an undoped sample with a grain size of ~3.5 μm at a σ of 100 MPa (Fig. 2-12) likely reflects the contribution of lattice dislocation processes to $\dot{\varepsilon}$. The Q of (lattice) dislocation-accommodated creep previously identified in Fe-free aggregates was estimated as ~600 kJ/mol (Tasaka et al., 2013).

The above calculations and observations made predominantly for Fe-free olivine aggregates indicate that the observed power-law creep at low σ in this study is a consequence of interface-controlled creep rather than an intra-granular dislocation process. Grain-boundary dislocations are commonly assumed in models of power-law interface-controlled creep. Creep rate controlled by grain-boundary dislocation mobility predicts an n_{int} of 2 (Eq. (1-4)) (Ashby, 1969; Burton, 1972; Arzt et al., 1983), while an n_{int} of 3 is proposed if creep rate is a function of dislocation density (Arzt et al., 1983). All models agree with a p of 1. So far, I do not have a good explanation for the n_{int} values of 2 (Nakakoji et al., 2018) and 3 (this study) for Fe-free and Fe-bearing olivine, respectively.

Based on the efforts to determine flow law parameters for interface-controlled creep using the parameters p = 1 and n_{int} = 3 (*section 2.3.4*), I propose the following constitutive equation for interface-controlled creep of undoped (reference) aggregates:

$$\dot{\varepsilon}_{\mathrm{int}}^{\mathrm{ref}} = 2.12 \times 10^{12} \mu\mathrm{m/MPa^3/s} \cdot (\sigma^3/d) \cdot \exp\left(-\frac{610\ \mathrm{kJ/mol}}{\mathrm{R}T}\right). \quad (2\text{-}8)$$

Although the theoretical model that produces an n_{int} of 3 also predicts that $Q_{\mathrm{int}} = Q_{\mathrm{diff}}$ (Arzt et al., 1983), I was not able to reproduce my mechanical data with this constraint on Q. The Q_{int} value that best describes the data is even larger than the Q values determined for Si self-diffusion in the olivine lattice (i.e., 530 kJ/mol by Dohmen et al., 2002; 410 kJ/mol by Fei et al., 2012). The source of the large Q_{int} is not known at this time.

2.4.3. Nature of grain boundaries

The existence of grain-boundary dislocations assumed for interface-controlled creep remains controversial, especially for general (normal) grain boundaries in oxides (Carter & Norton, 2013). Grain-boundary dislocations are sites where vacancy formation and absorption are expected to take place (Ashby, 1969; Burton, 1972; Arzt et al., 1983). Such reactions, as well as mass transport at grain boundaries, are necessary micro-processes for grain-boundary diffusion creep. Both grain-boundary micro-processes act in series and are mutually coupled during creep. Thus, the transition from power-law to linear (Newtonian) creep with increasing σ is commonly interpreted based on a transition in the rate-controlling micro-process from reaction to mass transfer. Meanwhile, in Earth science, diffusion creep is generally accepted as Newtonian creep, which implicitly assumes an infinite rate of reaction compared to the rate of mass transport. As I discuss later, this assumption is valid in most of the mantle; thus, I simply distinguish between power-law interface-controlled creep and diffusion creep in this study.

The excellent reproduction of $\dot{\varepsilon}$ in undoped samples by the series-sequential sum of the rates of interface-controlled creep and grain-boundary diffusion creep (Eq. (1-3)) (Fig. 2-13) supports the occurrence of the grain-boundary micro-processes considered above. Thus, the χ values (Figs. 2-14b and 2-15b) likely represent the effectiveness of doping in influencing these grain-boundary processes. I concluded that Ca and Al segregate at olivine grain boundaries in doped aggregates (*section 2.4.1.4*). The majority of χ values >1 over all σ (Figs. 2-14b and 2-15b) indicates that segregation enhances both grain-boundary processes, i.e., reaction and mass transport. At a given σ_0 and temperature, χ values are larger for samples with greater doping. I discussed the occurrence of stronger segregation in such samples, which also supports the idea of enhanced grain-boundary processes due to segregation.

The χ values seem to be positively correlated with temperature at high temperatures (Figs. 2-14b and 2-15b), while χ values are ~1 at low temperatures, even in samples where strong segregation is expected. An equilibrium segregation model (McLean, 1957; Hiraga et al., 2004) predicts that partitioning of incompatible elements including Ca and

Al into olivine grain boundaries relative to olivine grain matrices (lattice) decreases with increasing temperature. At the same time, elemental concentrations in the grain matrices increase with temperature via elemental exchange between olivine and pyroxenes, which in turn increase concentrations of these elements at the grain boundaries. As a result, changes in grain-boundary chemistry with temperature are predicted to be small, which has been experimentally confirmed (Hiraga et al., 2004). Thus, the enhancement of grain-boundary processes due to segregation appears to be thermally activated above a certain temperature without a change in the grain-boundary chemistry. Even if grain boundaries were at chemical disequilibrium during the deformation experiments, such predicted small temperature dependent segregation would result in similar grain-boundary chemistry both at equilibrium and disequilibrium.

2.4.4. Grain boundaries at near-solidus conditions

The changes in χ with σ_0 at a constant temperature (Fig. 2-14b) indicate different χ values for interface-controlled and diffusion creep. Thus, enhancement of grain-boundary processes should be examined based on the decomposed χ value, i.e., χ_{int} and χ_{diff}, for interface-controlled and diffusion creep, respectively, which are related to $\dot{\varepsilon}_{0\_\mathrm{ref}}^{\mathrm{doped}}$ by

$$\left(\dot{\varepsilon}_{0\_\mathrm{ref}}^{\mathrm{doped}}\right)^{-1} = \left[\chi_{\mathrm{int}} \cdot \left(\sigma_{0\_\mathrm{ref}}^{\mathrm{doped}}\right)^{3}\right]^{-1} + \left[\chi_{\mathrm{diff}} \cdot \left(\sigma_{0\_\mathrm{ref}}^{\mathrm{doped}}\right)\right]^{-1}. \quad (2\text{-}9)$$

The χ is related to χ_{int} and χ_{diff} (Eqs. (2-4), (2-5), and (2-9)) by

$$\chi = \frac{\left[\left(\sigma_{0\_\mathrm{ref}}^{\mathrm{doped}}\right)^{2}+1\right]\cdot\chi_{\mathrm{diff}}}{\left(\sigma_{0\_\mathrm{ref}}^{\mathrm{doped}}\right)^{2}+(\chi_{\mathrm{diff}}/\chi_{\mathrm{int}})}. \quad (2\text{-}10)$$

I determined the χ_{int} and χ_{diff} values for $(\sigma_{0\_\mathrm{ref}}^{\mathrm{doped}}, \chi)$ that best explained the data of each stepped-load test (Fig. 2-14b). For $(\sigma_{0\_\mathrm{ref}}^{\mathrm{doped}}, \chi)$ from stepped-temperature tests, I assume that $\chi_{\mathrm{int}} >> \chi_{\mathrm{diff}}$ in Eq. (2-10) so that I extract only χ_{diff} values from the data. This point is well supported by the conclusion that $\dot{\varepsilon}_{\mathrm{obs}} \approx \dot{\varepsilon}_{\mathrm{diff}}$ at the stresses applied during the tests (Figs. 2-10b and 2-11b). Because of the strong temperature dependence of χ (Figs. 2-14b and 2-15b), the resulting χ_{int} and χ_{diff} values are plotted in

Arrhenius space (Figs. 2-17a and b). Similar χ_{diff} values were obtained from the results of stepped-temperature and stepped-load tests on the same samples (Fig. 2-17b). Overall, both χ_{int} and χ_{diff} values increase with temperature. The χ_{int} values of up to ~10^2 at the highest temperatures indicate a significant enhancement in the interface-controlled creep rate. Meanwhile, χ_{int} and χ_{diff} values decrease to ~1 or less with little temperature dependence at low temperatures, which is more clearly seen in χ_{diff} due to its large data set.

Grain-boundary disordering starting below T_{s}, often referred to as pre-melting and/or grain-boundary complexion, is known in various materials (Cantwell et al., 2014). As the disordering is promoted by grain-boundary segregation, the temperature at which disordering begins decreases for stronger segregation. Once grain-boundary disordering begins, its magnitude increases with temperature. A strong olivine CPO development during diffusion creep above a certain temperature was previously attributed to such grain-boundary disordering (Miyazaki et al., 2013). A CPO resulted from preferential GBS along low-index (crystallographic) plane grain boundaries that developed at the same temperature conditions as the CPO (Miyazaki et al., 2013; Maruyama & Hiraga, 2017b). After investigating the appearance of low-index grain boundaries at different chemical, temperature, and pressure conditions, a temperature of $\geq 0.92 \times T_{\mathrm{s}}$ was proposed as the condition for such boundaries to develop (Miyazaki et al., 2013). This conclusion is very similar to that proposed by Yamauchi & Takei (2016) for grain-boundary pre-melting, which starts from $0.94\times T_{\mathrm{s}}$.

Indeed, the enhancement of grain-boundary processes above certain temperatures identified through the χ_{int} and χ_{diff} values (Figs. 2-17a and b) appears to correlate with such grain-boundary disordering. Given that the source of the χ value is grain-boundary disordering, I predict the same Arrhenius-like behavior of χ_{int} and χ_{diff} values, i.e., χ_{int} and $\chi_{\mathrm{diff}} \propto \exp\left(-\frac{\Delta Q}{\mathrm{R}T}\right)$ where ΔQ is common to both χ_{int} and χ_{diff} (Fig. 2-17). The pre-melting effect on the diffusion creep rate was found to be an Arrhenius-type process and was quantified using ΔQ in Yamauchi & Takei (2016). I obtained a ΔQ value of 230 kJ/mol from χ_{diff} values of >1 from the $Ca_{0.3}Al_{0.5}$-doped sample, which exhibits Arrhenius behavior most clearly (Fig. 2-17b). This ΔQ value reasonably explains the temperature dependence of χ_{int} and other χ_{diff} values of >1 as shown by the colored lines in Figs. 2-17a and b. Here I define T_{enh}, which describes the temperature at which the enhancement of grain-boundary processes begins. In most cases, I see $\chi_{\mathrm{int}} >> \chi_{\mathrm{diff}}$ at a given temperatures, indicating that T_{enh} is different for interface-controlled and diffusion creep processes. Thus, I refer to T_{enh} for interface-controlled

creep and diffusion creep as $T_{\mathrm{enh\_int}}$ and $T_{\mathrm{enh\_diff}}$, respectively, hereafter. To determine $T_{\mathrm{enh\_int}}$ and $T_{\mathrm{enh\_diff}}$ for each sample, I take the point where the best-fit (colored) lines with slopes corresponding to ΔQ = 230 kJ/mol intersect with χ_{int} = 1 and χ_{diff} = 1, respectively. I made fits through all χ_{int} and χ_{diff} values of >1.5 except for χ_{diff} from the $Ca_{0.1}Al_{0.2}$-doped sample, which does not show a clear enhancement. Indeed, the fits for χ_{int} and χ_{diff} values using a common ΔQ value are not always perfect, resulting in large uncertainties associated with $T_{\mathrm{enh\_int}}$ and $T_{\mathrm{enh\_diff}}$.

As I discussed, the grain-boundary disordering starts from the temperature related to T_{s}. Thus, I compare the obtained $T_{\mathrm{enh\_int}}$ and $T_{\mathrm{enh\_diff}}$ with T_{s} of each aggregate except for the $Ca_{0.1}Al_{0.2}$-doped aggregate whose T_{s} was not constrained (Table 2-1) in Fig. 2-18. I simply used a T_{s} of 1382˚C for the Ca-doped Fe-free aggregate, which was estimated in the previous study of our research group (Miyazaki et al., 2013). Overall, both $T_{\mathrm{enh\_int}}$ and $T_{\mathrm{enh\_diff}}$ are positively correlated with T_{s}. I can describe $T_{\mathrm{enh\_diff}}$ as $0.92 \times T_{\mathrm{s}}$, which corresponds to the previously proposed grain-boundary structural transition point (Miyazaki et al., 2013), while a much smaller coefficient of 0.84 is required to explain $T_{\mathrm{enh\_int}}$ based on T_{s} (Fig. 2-18).

The $T_{\mathrm{enh\_diff}}$ of the $Ca_{5.2}$-doped Fe-free sample is 1250˚C (Fig. 2-17b). A strong olivine CPO develops starting at 1250˚C during diffusion creep of the same material (Miyazaki et al., 2013). The $T_{\mathrm{enh\_diff}}$ of the $Ca_{0.3}Al_{0.5}$-doped (Fe-bearing) sample is 1150˚C (Fig. 2-17b). This sample exhibits CPO when deformed at 1250˚C, where tabular olivine grains appear, which is indicative of the development of low-index plane grain boundaries (Figs. 2-6f and h) (Miyazaki et al., 2013; Maruyama & Hiraga, 2017b). Thus, both doped Fe-free and Fe-bearing aggregates exhibit similar microstructural and mechanical transitions with respect to temperature, but with different transition temperatures. This can be reasonably explained by the Fe-bearing sample having a lower T_{s} by more than 100˚C than the Fe-free sample (Fig. 2-18, Table 2-1).

As discussed above, a discrete source such as dislocations was usually assumed for reactions and a continuous path for mass transfer. Such different structural characteristics predict that limited (local) and extensive (widespread) grain-boundary disordering is required to enhance the rates of interface-controlled creep and diffusion creep, respectively. As a result, grain-boundary disordering, which increases with temperature, first affects interface-controlled creep and then diffusion creep with increasing temperature; thus, $T_{\mathrm{enh\_int}} < T_{\mathrm{enh\_diff}}$ (Fig. 2-18).

2.4.5. Extended olivine flow law

In the above, I interpret $\dot{\varepsilon}$ data for doped samples based on $\dot{\varepsilon}_{\rm int}^{\rm ref}$ and $\dot{\varepsilon}_{\rm diff}^{\rm ref}$, which are determined for the undoped (reference) olivine, as

$$\dot{\varepsilon}^{-1} = \left(\chi_{\rm int} \cdot \dot{\varepsilon}_{\rm int}^{\rm ref}\right)^{-1} + \left(\chi_{\rm diff} \cdot \dot{\varepsilon}_{\rm diff}^{\rm ref}\right)^{-1}. \quad (2\text{-}11)$$

where

$$\chi_{\rm int} = 1 \quad \text{at } T \le 0.84 \cdot T_{\rm s}, \quad (2\text{-}12)$$
$$\chi_{\rm int} = \exp\left[-\frac{\Delta Q}{\rm R} \cdot \left(\frac{1}{T} - \frac{1}{0.84 T_{\rm s}}\right)\right] \quad \text{at } T > 0.84 \cdot T_{\rm s}$$

and

$$\chi_{\rm diff} = 1 \quad \text{at } T \le 0.92 \cdot T_{\rm s}, \quad (2\text{-}13)$$
$$\chi_{\rm diff} = \exp\left[-\frac{\Delta Q}{\rm R} \cdot \left(\frac{1}{T} - \frac{1}{0.92 T_{\rm s}}\right)\right] \text{ at } T > 0.92 \cdot T_{\rm s},$$

where ΔQ = 230 kJ/mol. Curves representing Eq. (2-11) with $\chi_{\rm int}$ and $\chi_{\rm diff}$ determined by Eqs. (2-12) and (2-13) and representative experimental conditions (i.e., d, T, and $T_{\rm s}$) for each stepped-load test on doped samples correspond to the solid lines in Figs. 2-8d–f, showing good reproductions of most of the experimental data.

Now I can estimate $(\sigma^*, \dot{\varepsilon}^*)$ in doped olivine under any conditions (Eqs. (1-6) and (1-7)) (except for the $Ca_{0.1}Al_{0.2}$-doped sample, whose $T_{\rm s}$ was not well constrained (Table 2-1)) based on $\chi_{\rm int} \cdot \dot{\varepsilon}_{\rm int}^{\rm ref} = \chi_{\rm diff} \cdot \dot{\varepsilon}_{\rm diff}^{\rm ref}$. I obtain

$$\sigma^* = \left[d^{-2} \frac{\chi_{\rm diff}}{\chi_{\rm int}} \frac{A_{\rm diff}}{A_{\rm int}} \exp\left(\frac{Q_{\rm int} - Q_{\rm diff}}{\rm R T}\right)\right]^{\frac{1}{2}}, \quad (2\text{-}14)$$

$$\dot{\varepsilon}^* = \left[d^{-8} \frac{(\chi_{\rm diff})^3}{\chi_{\rm int}} \frac{(A_{\rm diff})^3}{A_{\rm int}} \exp\left(\frac{Q_{\rm int} - 3Q_{\rm diff}}{\rm R T}\right)\right]^{\frac{1}{2}}, \quad (2\text{-}15)$$

where $\chi_{\rm int}$ and $\chi_{\rm diff}$ satisfy Eqs. (2-12) and (2-13), respectively. Each (σ, $\dot{\varepsilon}$) of the doped samples is transformed to a nondimensional value ($\sigma_0^{\rm doped}$, $\dot{\varepsilon}_0^{\rm doped}$) using Eq. (1-8) by replacing $\sigma^{*\rm ref}$ and $\dot{\varepsilon}^{*\rm ref}$ with σ^* and $\dot{\varepsilon}^*$, respectively (Eqs. (2-14) and (2-15)). These calculated ($\sigma_0^{\rm doped}$, $\dot{\varepsilon}_0^{\rm doped}$) are plotted in Fig. 2-19 and essentially follow the predicted curve of Eq. (2-4), which demonstrates the ability of my equation to express the

effects of doping on olivine creep.

2.4.6. Conditions for interface-controlled creep

Interface-controlled creep dominates when $\sigma<\sigma^*$ (or $\dot{\varepsilon}<\dot{\varepsilon}^*$) (Eqs. (2-14) and (2-15)). The condition is rewritten as

$$\sigma \cdot d < \left[\frac{A_{\mathrm{diff}}}{A_{\mathrm{int}}}\frac{\chi_{\mathrm{diff}}}{\chi_{\mathrm{int}}}\exp\left(\frac{Q_{\mathrm{int}}-Q_{\mathrm{diff}}}{\mathrm{R}T}\right)\right]^{\frac{1}{2}} \qquad (2\text{-}16)$$

based on Eq. (2-14). I can think of Eq. (2-16) as an improved version of the relationship in Nakakoji et al. (2018), which was derived based on results for undoped Fe-free aggregates. Since $\frac{\chi_{\mathrm{diff}}}{\chi_{\mathrm{int}}}$ is a function of T_{s}, which can change significantly with different chemical and pressure conditions, I calculated $\sigma \cdot d$ (MPa·mm) for a T_{s} range of 1000 to 2000˚C (Fig. 2-20). The interface-controlled creep regime expands with decreasing temperature and/or increasing T_{s} due to $Q_{\mathrm{int}}>Q_{\mathrm{diff}}$ and $T_{\mathrm{enh\_int}}<T_{\mathrm{enh\_diff}}$.

In that study, they assumed the formation of a shear zone due to loading by the Hawaiian Islands (Nakakoji et al., 2018), which accumulates stresses of 100–200 MPa beneath the islands (Zhong & Watts, 2013). They predicted grain size to change systematically with depth (temperature) from 10 μm at 700˚C to 2 mm at 1350˚C in the zone, which explains the viscosity profile with depth beneath Hawaii Island (Watts & Zhong, 2000) based on grain-boundary diffusion creep of peridotite (Nakakoji et al., 2018). The quantity $\sigma \cdot d$ is calculated to be $\geq$1 MPa·mm even at the finest grain size in the zone, indicating diffusion creep at all depths (Fig. 2-20). Given a typical mantle grain size of 2 mm, interface-controlled creep is predicted to be dominant at σ of <0.02 MPa, indicating that interface-controlled creep plays little role in deformation of most of the mantle.

At a grain size and temperature of 10 μm and 1200˚C, respectively, a representative condition for a conventional creep experiment, interface-controlled creep becomes dominant at σ of <1 MPa (Fig. 2-20). No reliable data are experimentally obtained at such stresses, which explains why only a few studies (Sundberg & Cooper, 2008; Zhao et al., 2019) were performed on interface-controlled creep in minerals.

Some friction experiments suggest a superplastic deformation mechanism accommodated by diffusion to play a role during seismic faulting (De Paola et al., 2015). This idea was proposed based on extrapolation of the diffusion creep law established in micron-to-millimeter grain-size materials (calcite aggregates in their case) to grain sizes

of 10–100 nm. My identification of interface-controlled creep indicates that a simple extrapolation of the diffusion creep flow law to such very fine grain sizes overestimates the strain rate and/or underestimates the strength of the material.

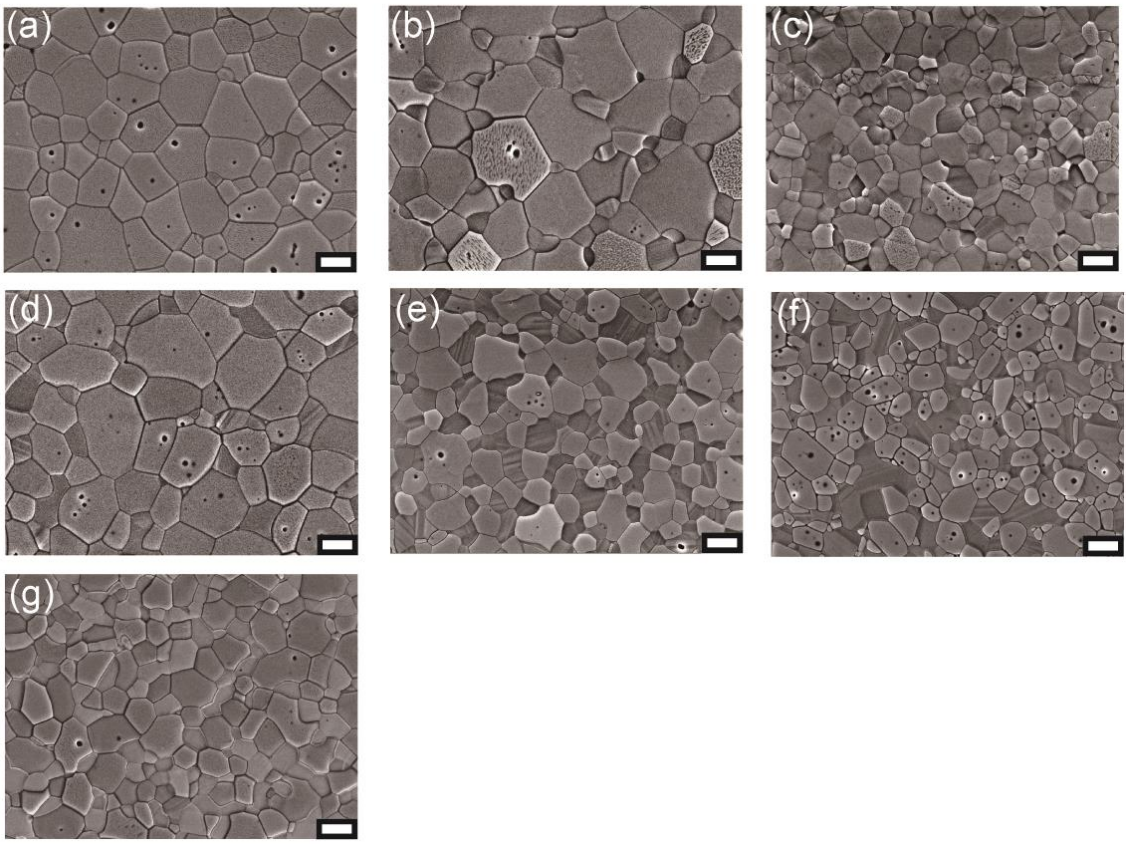

Fig. 2-1. Microstructures of the synthesized aggregates used for deformation experiments in this study. (a) Undoped f_{px} = 0 aggregate. (b) Undoped f_{px} = 0.1 aggregate. (c) Undoped f_{px} = 0.3 aggregate. (d) $Ca_{0.1}Al_{0.1}$-doped aggregate. (e) $Ca_{0.1}Al_{0.2}$-doped aggregate. (f) $Ca_{0.3}Al_{0.5}$-doped aggregate. (g) $Ca_{5.0}$-doped aggregate. Gray and dark-gray grains in (a)-(f) correspond to olivine and enstatite, respectively. Gray and light-gray grains in (g) correspond to olivine and diopside, respectively. Pores appear as small black dots in intra-granular regions in the images. Scale bar is 1 μm.

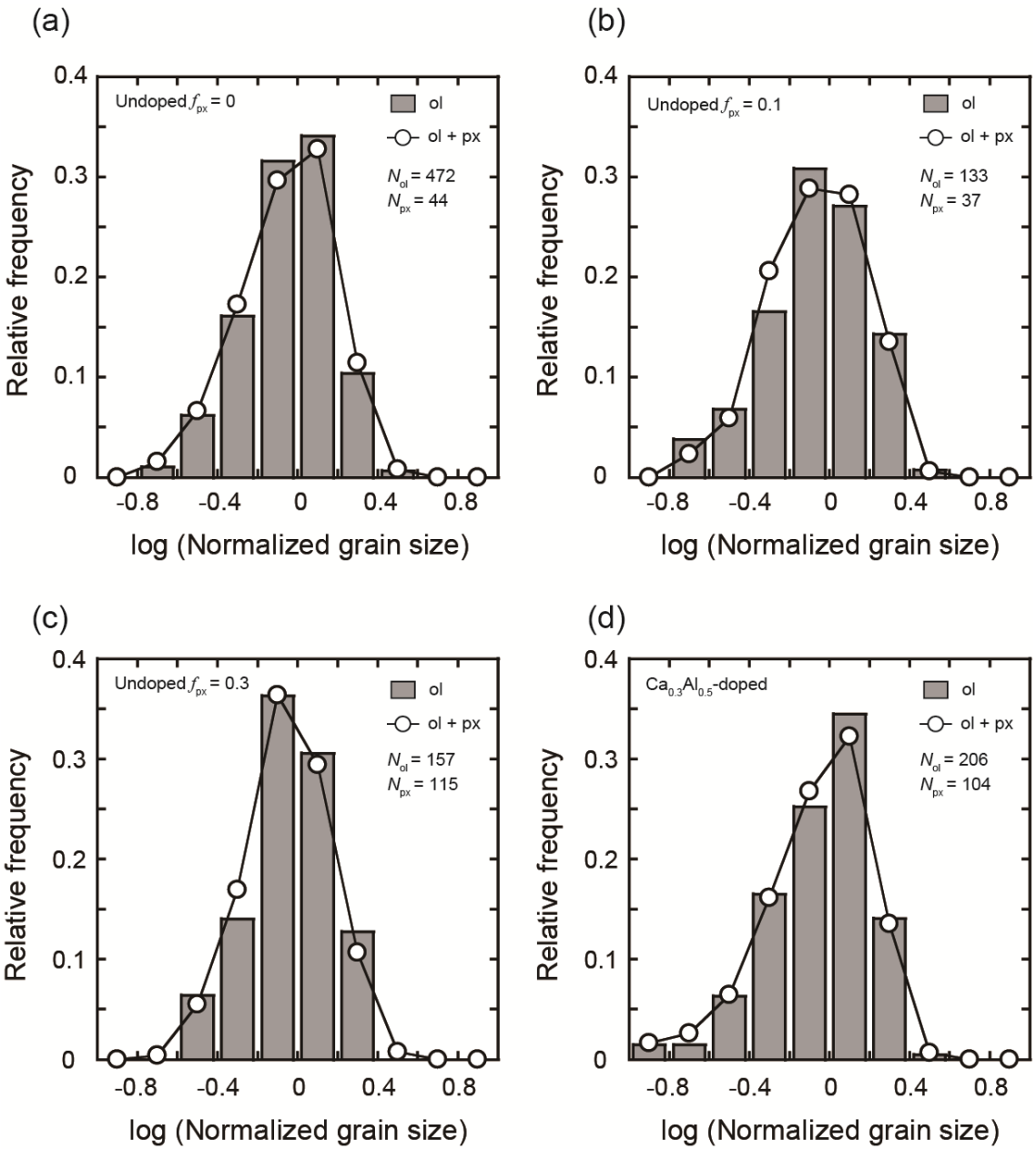

Fig. 2-2. Grain size distributions in the starting materials for deformation tests. Analyses of the relative frequency (probability) of the observed diameter of individual grains (d_i) normalized by d ($= \frac{1}{N}\sum_{i=1}^{N} d_i$ where N is the total number of grains) is shown for olivine alone (grey columns) and for olivine + pyroxene grains (open circles). (a) KH-14. (b) KH-81. (c) KH-87. (d) KH-71. *N*: number of analyzed grains.

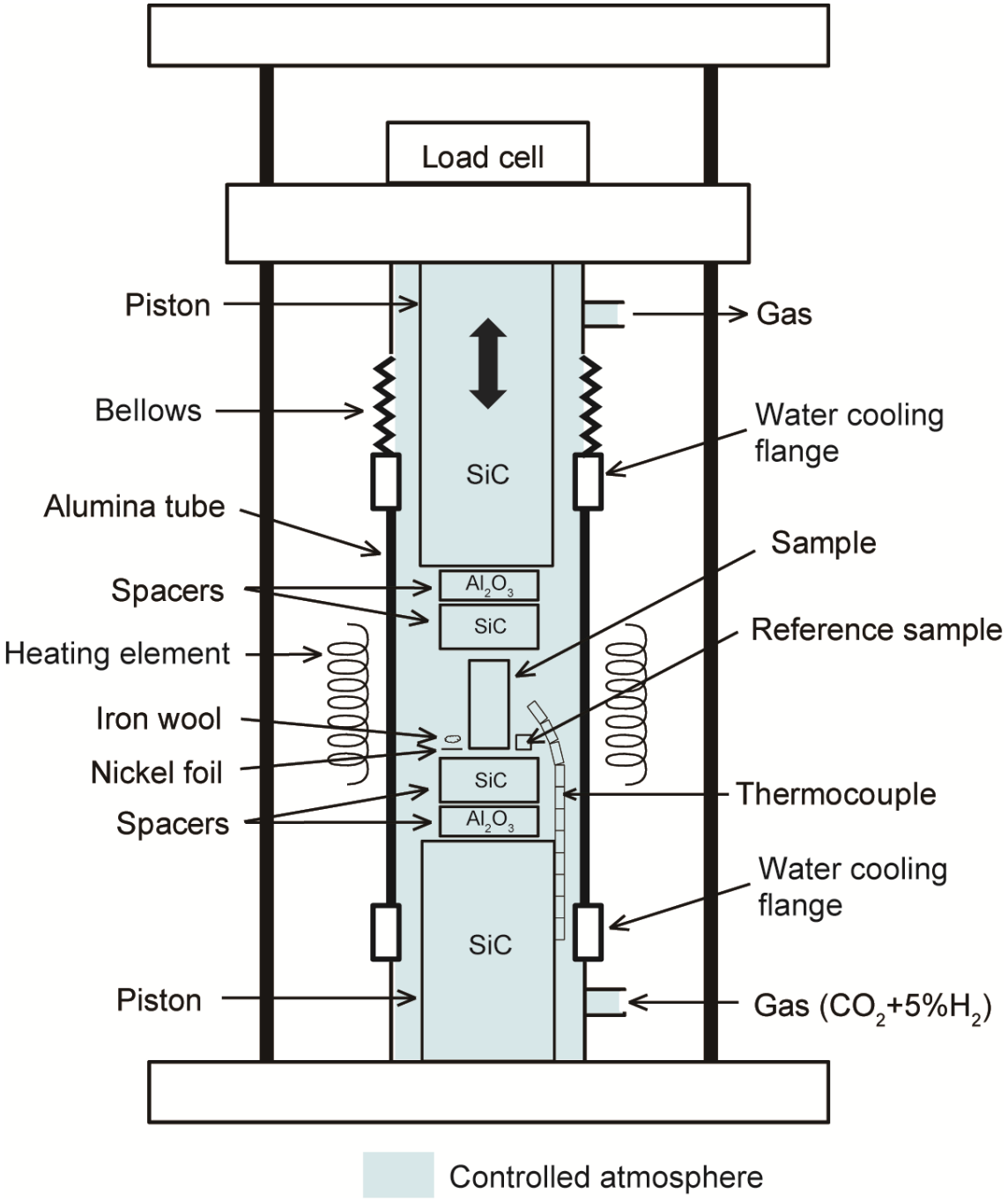

Fig. 2-3. Experimental apparatus for deformation experiments using a box furnace attached to a mechanical testing machine. The space filled with CO_2 + 5% H_2 gas is marked in light blue. The gas inlet and outlet are indicated by arrows. The upper and lower parts of the alumina tube are connected to the water-cooled flanges with a rubber O-ring in between. The upper SiC piston moves to provide a load on the sample during the test.

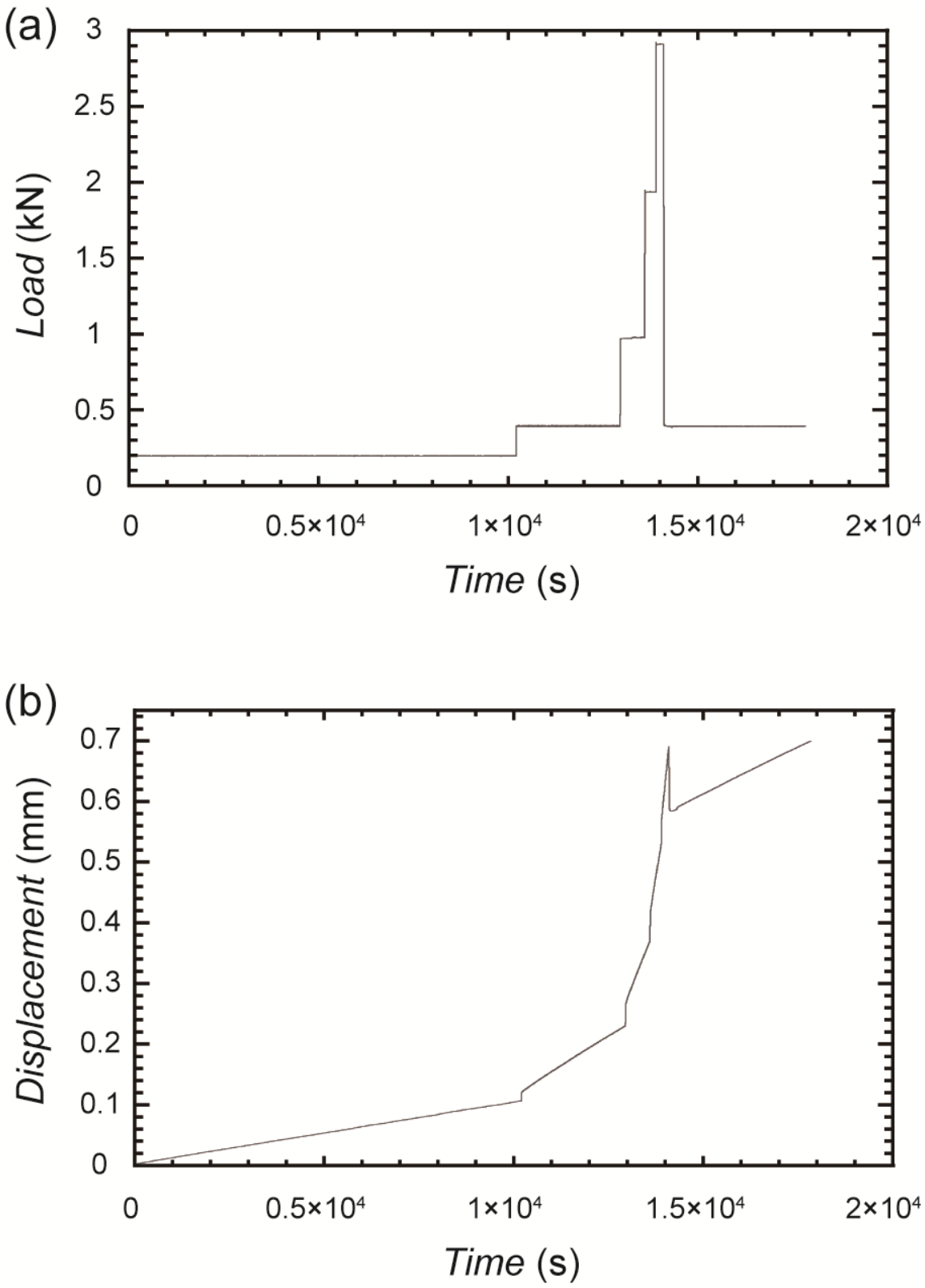

Fig. 2-4. Rheological data obtained during a stepped-load test (KH-53) at 1250˚C. (a) Load versus time curve. (b) Displacement versus time curve.

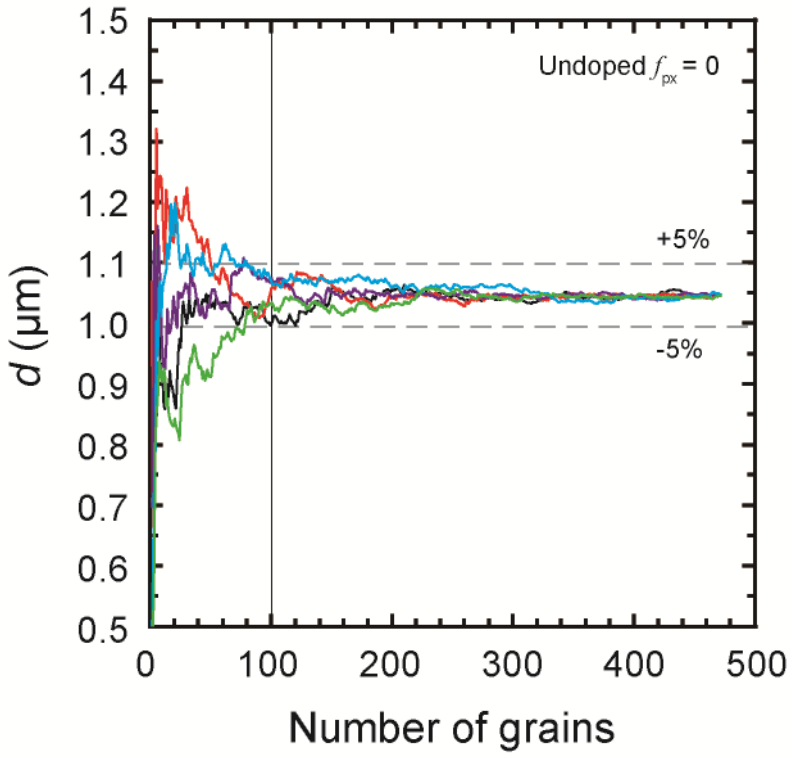

Fig. 2-5. Dependence of average grain size (i.e., ***d***) on the number of grains measured. Five different runs are shown of average grain size analyses based on randomly chosen grains from a data set with a total of 472 grains (in the initial sample of KH-14). The average grain sizes converge within ±5% of the average grain size of the total after analyzing >100 grains.

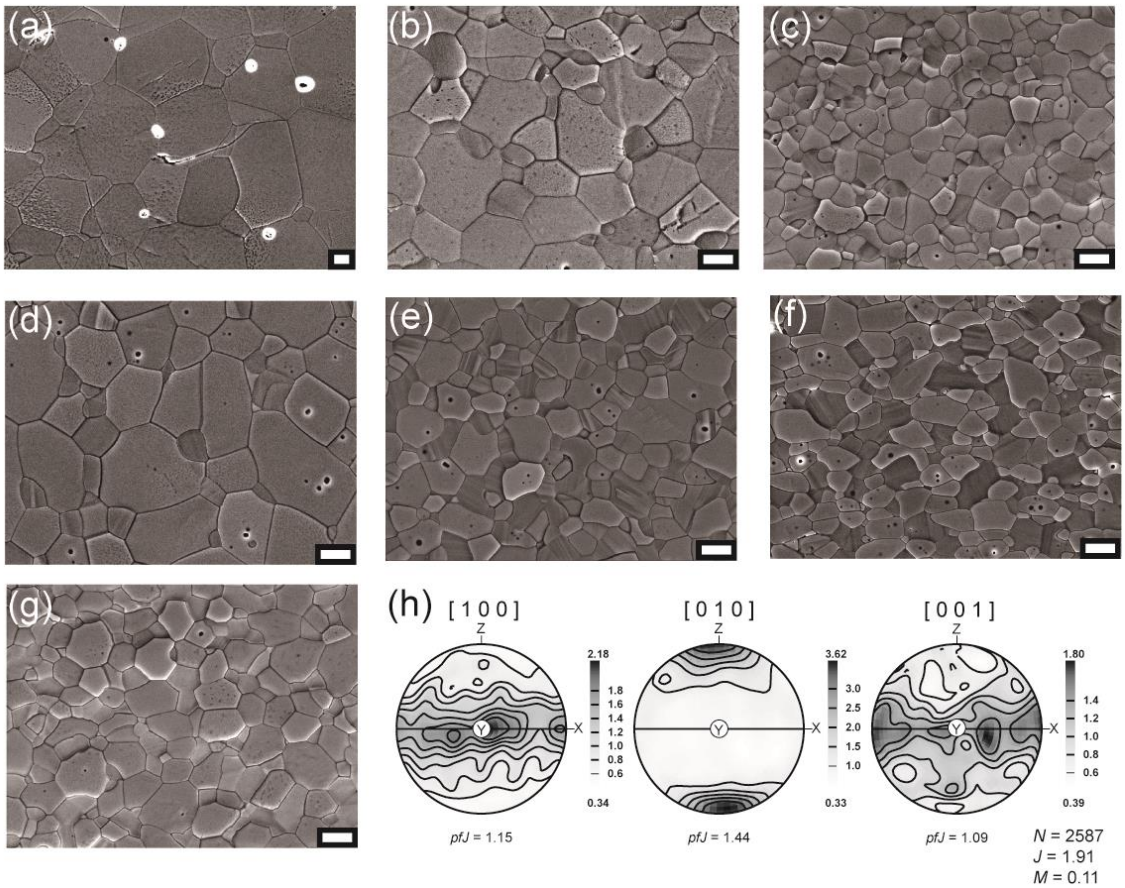

Fig. 2-6. Microstructures of deformed samples. (a) Undoped f_{px} = 0 sample (KH-138). (b) Undoped f_{px} = 0.1 sample (KH-148). (c) Undoped f_{px} = 0.3 sample (KH-87). (d) $Ca_{0.1}Al_{0.1}$-doped sample (KH-68). (e) $Ca_{0.1}Al_{0.2}$-doped sample (KH-72). (f) $Ca_{0.3}Al_{0.5}$-doped sample (KH-71). (g) $Ca_{5.0}$-doped sample (KH-172). Gray and dark-gray grains correspond to olivine and enstatite, respectively, in (a) through (f), while gray and light-gray grains correspond to olivine and diopside, respectively, in (g). Small black dots in intra-granular regions are pores. Cracks can be seen in (a). Scale bar is 1 μm. Compression axis is vertical. (h) Lower-hemisphere projections of the crystallographic orientations of olivine grains from the $Ca_{0.3}Al_{0.5}$-doped sample are shown in (f) (KH-71). *N*: number of analyzed grains; *J* refers to J index; *M* refers to M index; *pfJ* refers to the pfJ index.

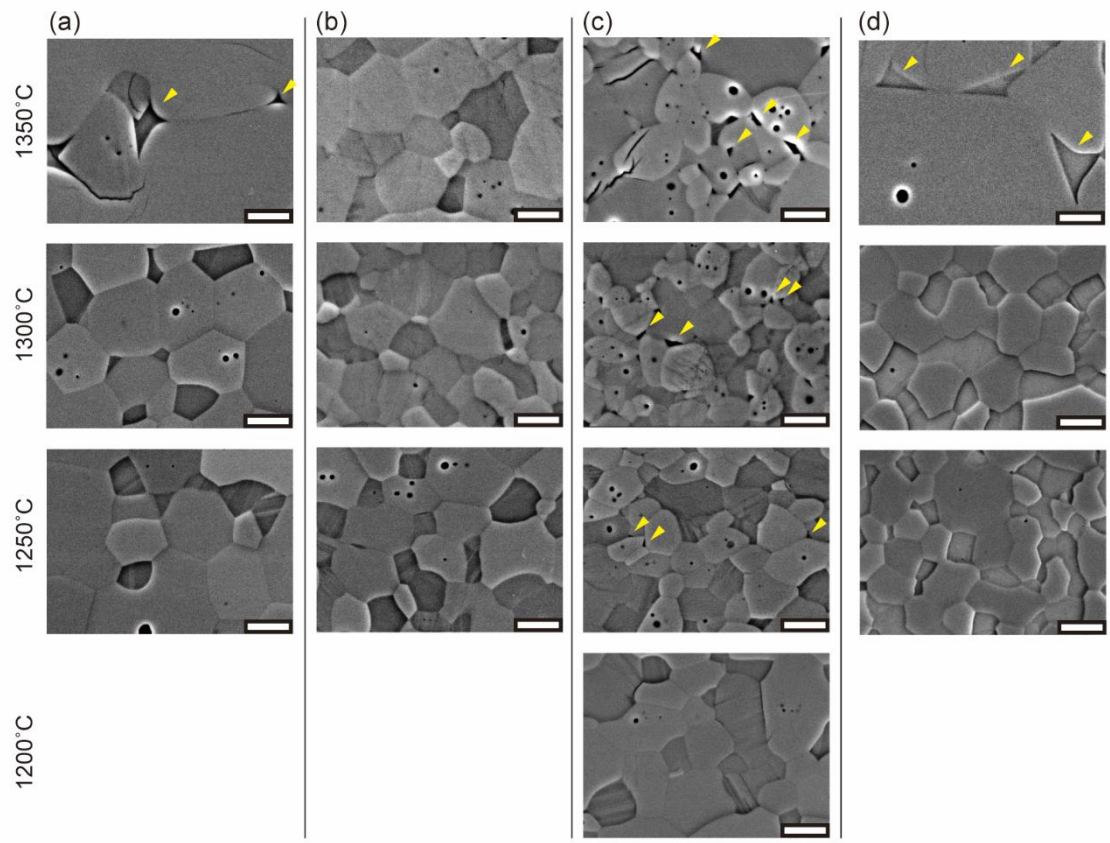

Fig. 2-7. Microstructures of doped aggregates after annealing at different temperatures. (a) $Ca_{0.1}Al_{0.1}$-doped aggregate. (b) $Ca_{0.1}Al_{0.2}$-doped aggregate. (c) $Ca_{0.3}Al_{0.5}$-doped aggregate. (d) $Ca_{5.0}$-doped aggregate. Temperatures are indicated on the left side. Melt (glass) is indicated by yellow arrows. Gray and dark-gray grains correspond to olivine and enstatite, respectively, in (a–c), while gray and light-gray grains correspond to olivine and diopside, respectively, in (d). Scale bar is 1 μm.

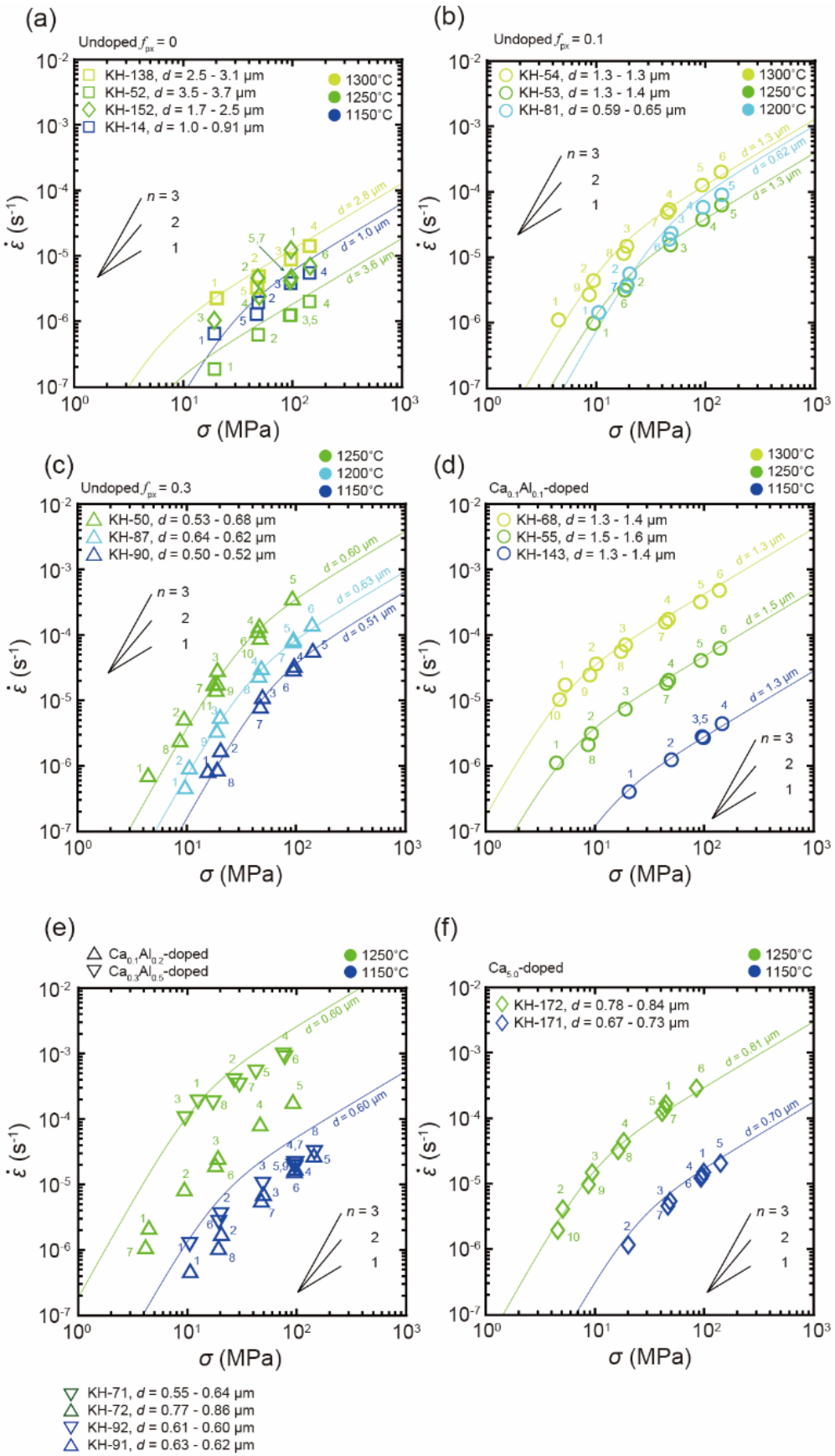
(a)
Undoped f_{px} = 0
KH-138, d = 2.5 - 3.1 μm
KH-52, d = 3.5 - 3.7 μm
KH-152, d = 1.7 - 2.5 μm
KH-14, d = 1.0 - 0.91 μm
1300°C
1250°C
1150°C
n = 3
2
1
d = 2.8 μm
d = 1.0 μm
d = 3.6 μm
(b)
Undoped f_{px} = 0.1
KH-54, d = 1.3 - 1.3 μm
KH-53, d = 1.3 - 1.4 μm
KH-81, d = 0.59 - 0.65 μm
1300°C
1250°C
1200°C
n = 3
2
1
d = 1.3 μm
d = 0.62 μm
d = 1.3 μm
(c)
Undoped f_{px} = 0.3
KH-50, d = 0.53 - 0.68 μm
KH-87, d = 0.64 - 0.62 μm
KH-90, d = 0.50 - 0.52 μm
1250°C
1200°C
1150°C
n = 3
2
1
d = 0.60 μm
d = 0.63 μm
d = 0.51 μm
(d)
$Ca_{0.1}Al_{0.1}$-doped
KH-68, d = 1.3 - 1.4 μm
KH-55, d = 1.5 - 1.6 μm
KH-143, d = 1.3 - 1.4 μm
1300°C
1250°C
1150°C
n = 3
2
1
d = 1.3 μm
d = 1.5 μm
d = 1.3 μm
(e)
$Ca_{0.1}Al_{0.2}$-doped
$Ca_{0.3}Al_{0.6}$-doped
1250°C
1150°C
n = 3
2
1
d = 0.60 μm
d = 0.60 μm
KH-71, d = 0.55 - 0.64 μm
KH-72, d = 0.77 - 0.86 μm
KH-92, d = 0.61 - 0.60 μm
KH-91, d = 0.63 - 0.62 μm
(f)
$Ca_{5.0}$-doped
1250°C
1150°C
KH-172, d = 0.78 - 0.84 μm
KH-171, d = 0.67 - 0.73 μm
n = 3
2
1
d = 0.81 μm
d = 0.70 μm
$\dot{\varepsilon}$ (s^{-1})
σ (MPa)

Fig. 2-8. Plots of strain rate as a function of stress during stepped-load tests. (a) Undoped f_{px} = 0 sample. (b) Undoped f_{px} = 0.1 sample. (c) Undoped f_{px} = 0.3 sample. (d) $Ca_{0.1}Al_{0.1}$-doped sample. (e) $Ca_{0.1}Al_{0.2}$-doped and $Ca_{0.2}Al_{0.5}$-doped samples. (f) $Ca_{5.0}$-doped sample. The slopes corresponding to three different stress exponents (n of 1, 2, and 3) are shown. The numbers beside each point correspond to the order of the load (stress) steps applied in a single test. Grain sizes estimated for the first and last steps in each test are included. Strain rates calculated for undoped samples based on Eq. (2-4) in (a–c) and for doped samples based on Eq. (2-11) in (d–f) at representative experimental conditions (i.e., d and T) with the determined flow law parameters are also shown. We did not calculate rates for tests KH-152, -72, and -91 due to a large change in grain size during the test for the former one and poorly constrained T_{s} for the latter two.

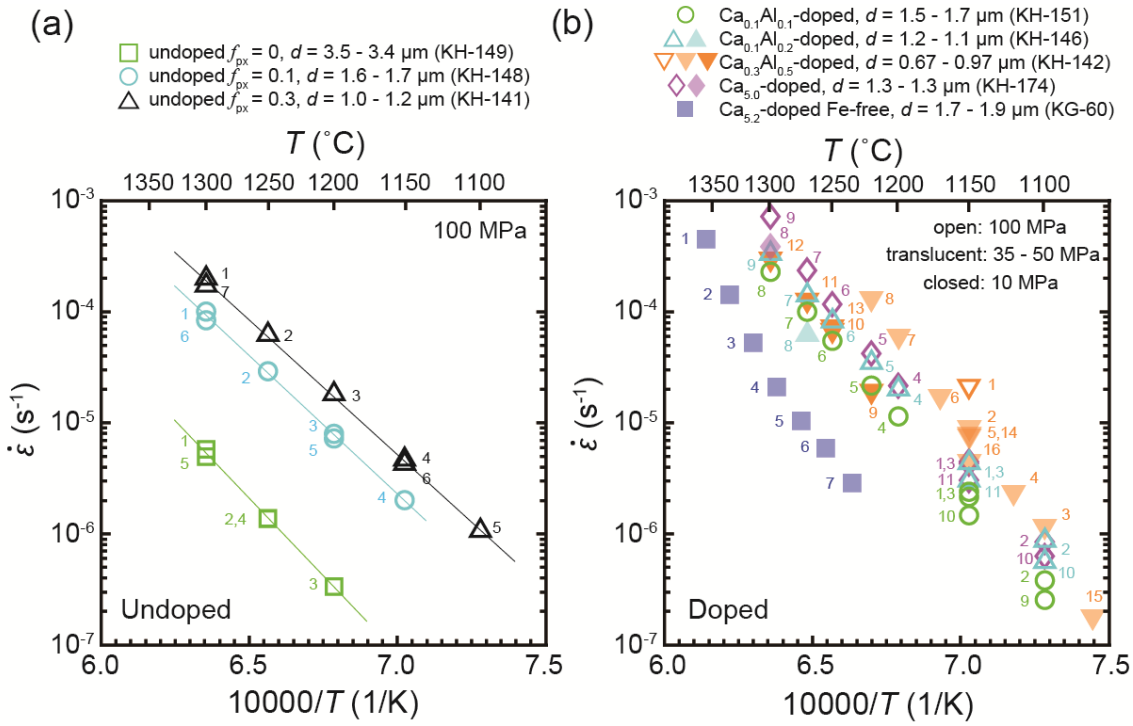

Fig. 2-9. Arrhenius plots of strain rate for stepped-temperature tests. (a) Undoped samples at a constant stress of 100 MPa. (b) Doped samples at stresses of 10–100 MPa. Stresses applied during tests are indicated by the symbol style. The numbers beside each point correspond to the order of the load (stress) steps applied in a single test. Grain sizes estimated for the first and last steps in each test are included. Linear least-squares fits to $\dot{\varepsilon}$ for each test on undoped samples are shown in (a).

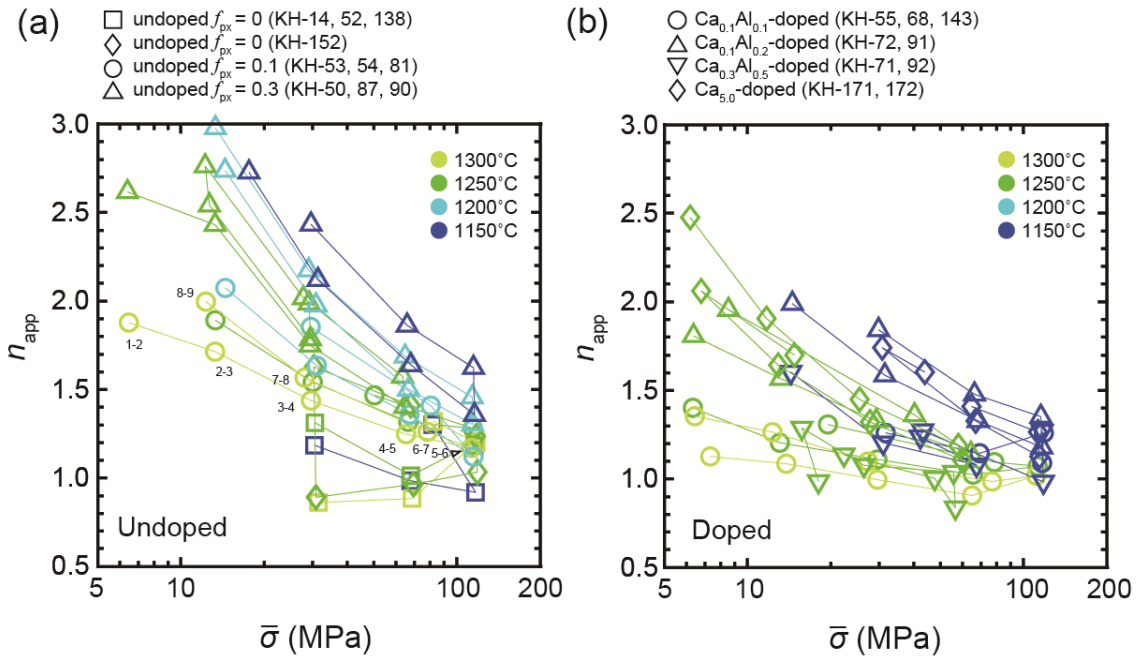

Fig. 2-10. The apparent stress exponent, n_{app} determined from two sets of stress and strain rate values as $n_{\mathrm{app}} = \frac{\log \dot{\varepsilon}_{i+1} - \log \dot{\varepsilon}_i}{\log \sigma_{i+1} - \log \sigma_i}$ versus the geometric average stress, $\bar{\sigma}$ (= $\sqrt{\sigma_i \sigma_{i+1}}$) for (a) undoped samples and (b) doped samples. σ_i and σ_{i+1} values are connected by lines in the figure. The numbers beside each point at 1300˚C (KH-54) correspond to those in Fig. 2-8b.

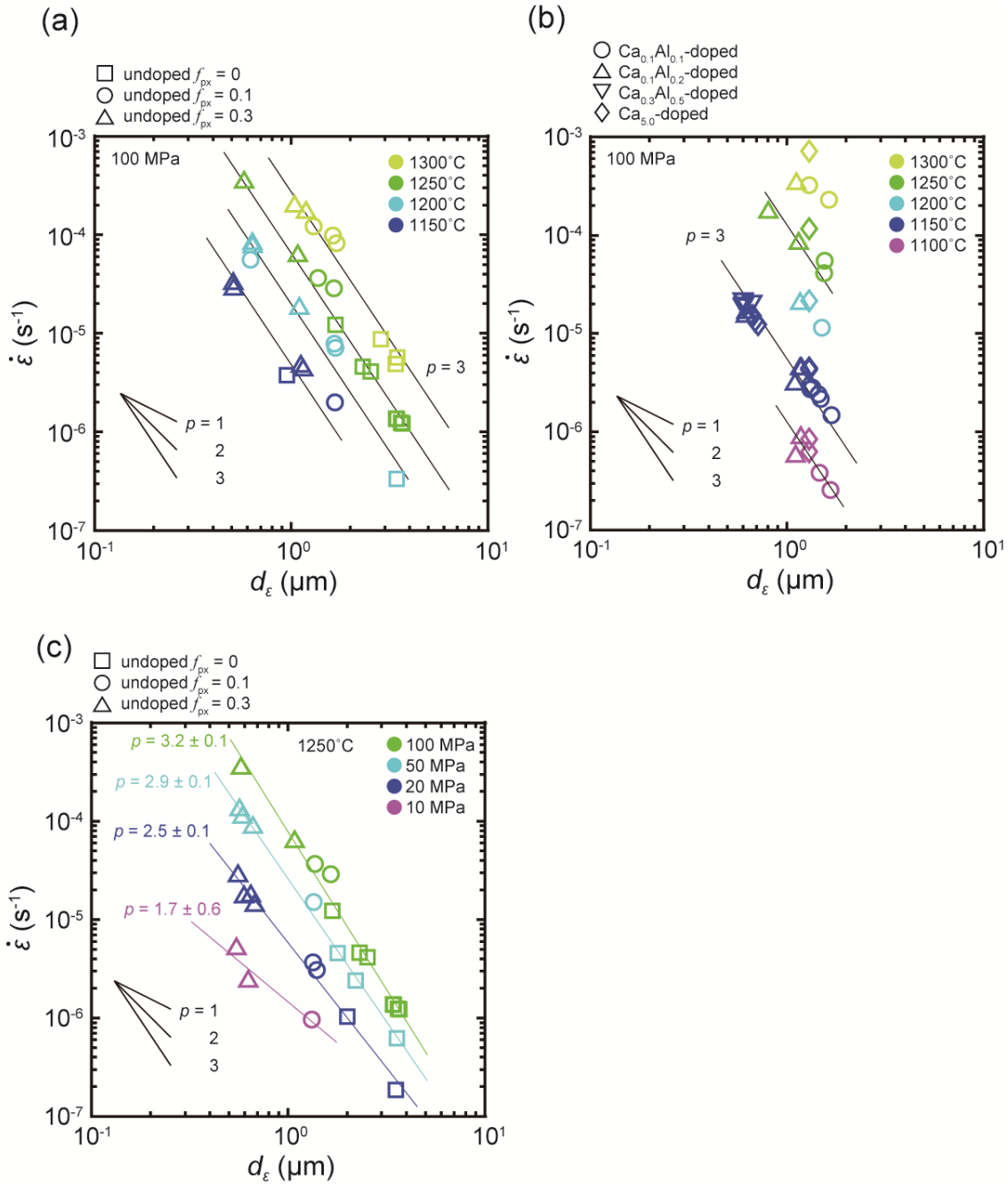

Fig. 2-11. Plots of strain rate as a function of estimated grain size (d_ε) during the creep tests (Eq. 2-1). The slopes corresponding to three different grain size exponents (p of 1, 2, and 3) are shown in each figure. (a) Strain rates of undoped samples at a stress of 100 MPa. (b) Strain rates of doped samples at a stress of 100 MPa. (c) Strain rates of undoped samples at stresses of 10, 20, 50, and 100 MPa. Lines obtained from least-squares fits for each stress are also shown in (c).

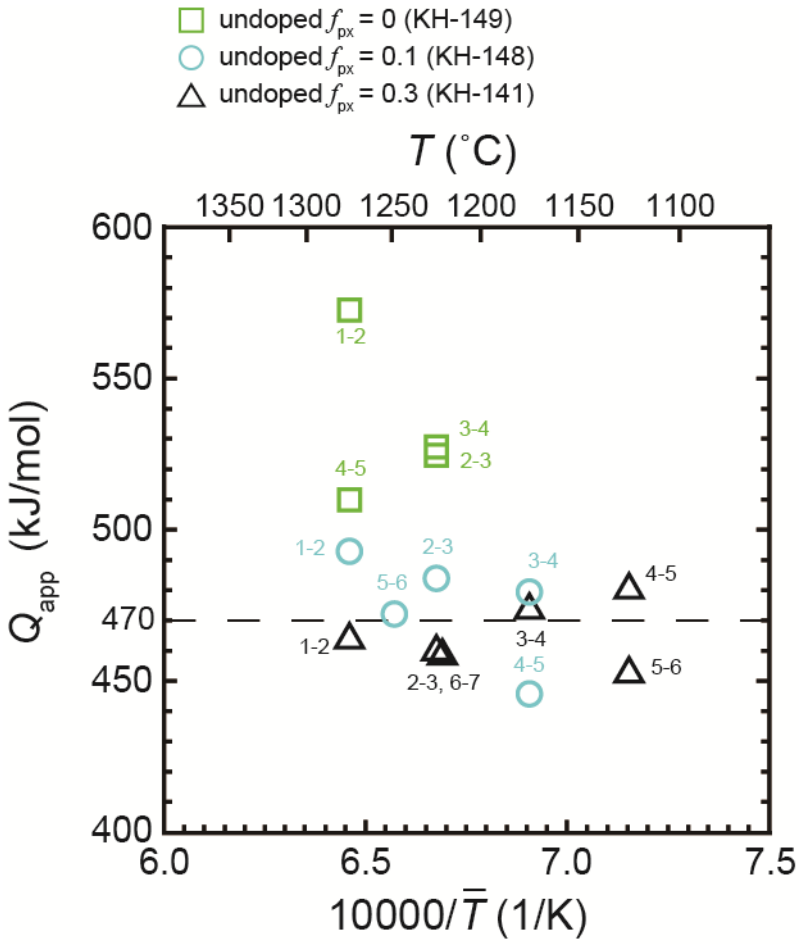

Fig. 2-12. The apparent activation energy, Q_{app} determined from two sets of temperature and strain rate values as $Q_{\text{app}} = -\text{R} \cdot \left(\frac{\ln \dot{\varepsilon}_{i+1} - \ln \dot{\varepsilon}_i}{T_{i+1}^{-1} - T_i^{-1}}\right)$ versus the arithmetic average inverse temperature, $1/\bar{T} = 0.5 \times \left(\frac{1}{T_i} + \frac{1}{T_{i+1}}\right)$ for undoped samples. The numbers beside each point correspond to those in Fig. 2-9a. The activation energy of 470 kJ/mol is indicated, which is consistent with the Q value obtained from least-squares fitting of the entire set of $\ln \dot{\varepsilon}$ vs. $1/T$ data.

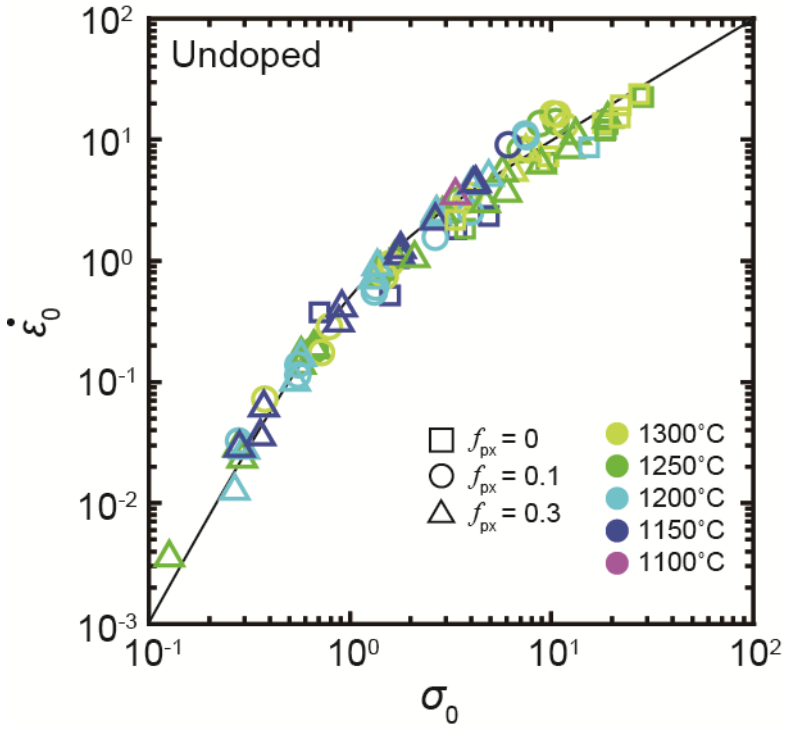

Fig. 2-13. Plot of nondimensionalized strain rate as a function of nondimensionalized stress calculated from all (σ, $\dot{\varepsilon}$) values of undoped samples. The predicted curve calculated from Eq. (2-4) is also shown in the figure.

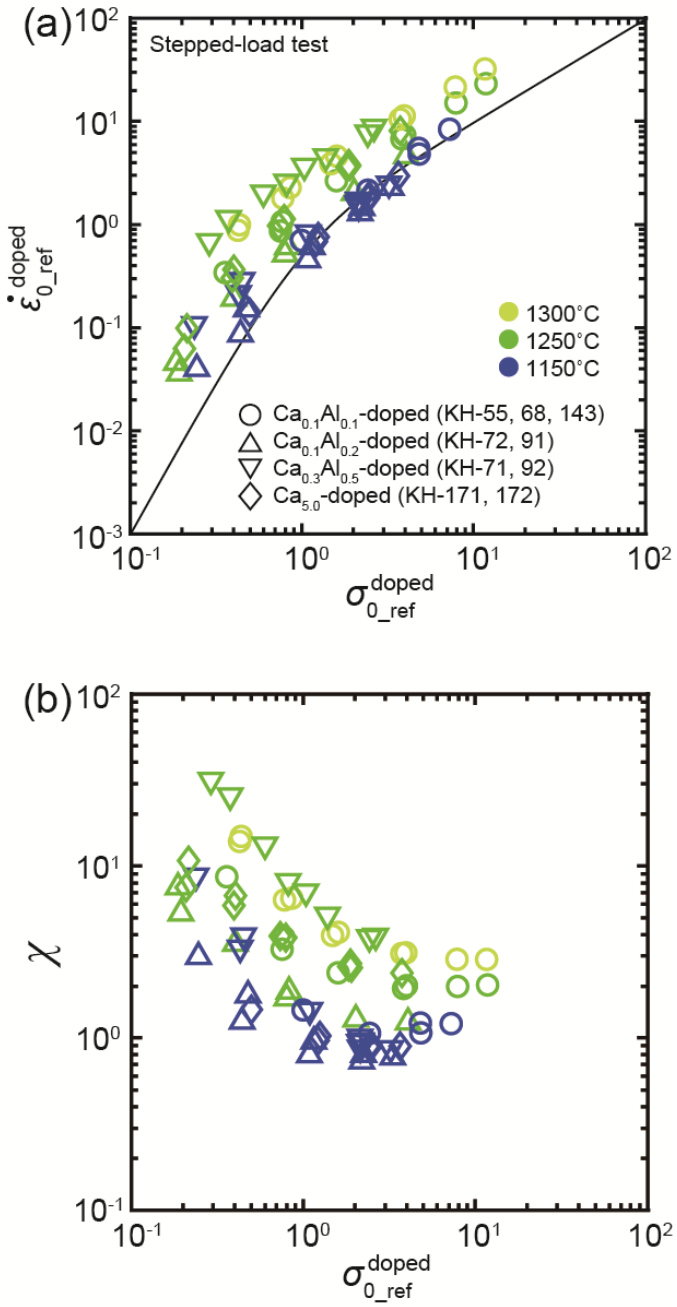

Fig. 2-14. Effect of doping on strain rates during stepped-load tests. (a) Plot of nondimensionalized strain rate ($\dot{\varepsilon}_{0\_ref}^{doped}$) as a function of nondimensionalized stress ($\sigma_{0\_ref}^{doped}$). Eq. (2-4) is also shown as a reference curve. (b) Plot of the change in strain rate due to doping, χ, as a function of $\sigma_{0\_ref}^{doped}$.

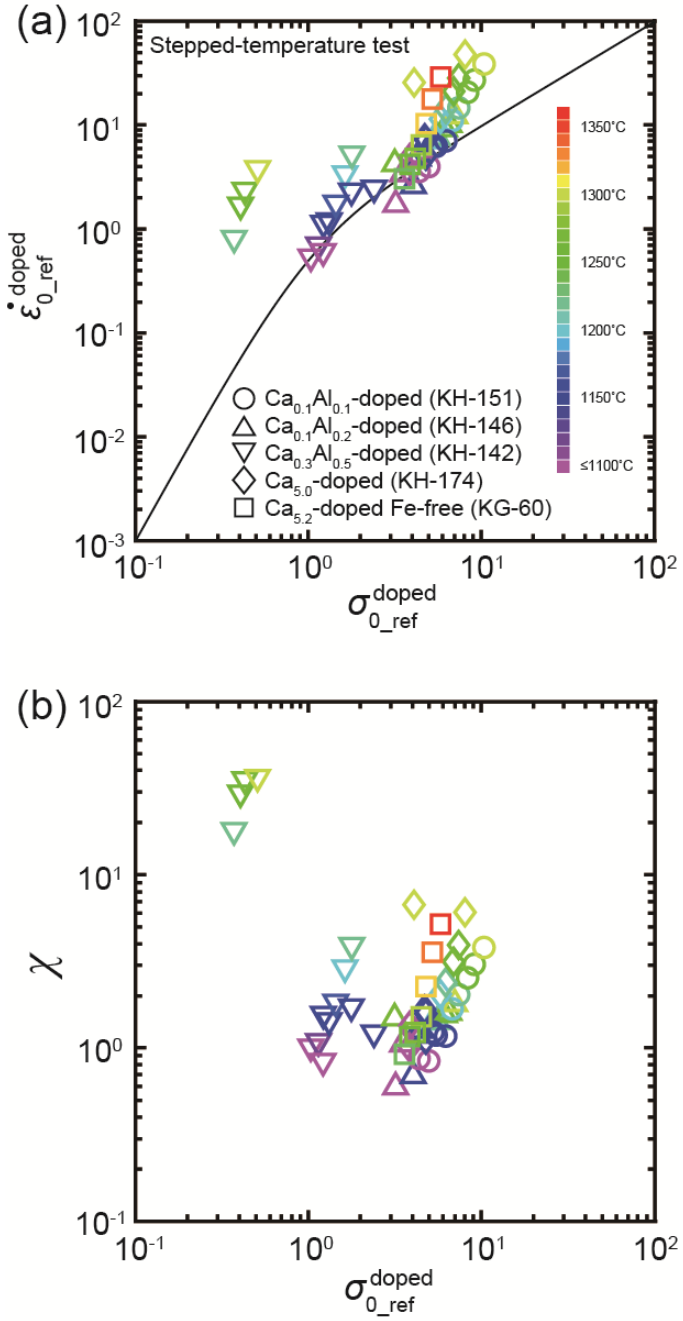

Fig. 2-15. Effect of doping on strain rates during stepped-temperature tests. (a) Plot of nondimensionalized strain rate ($\dot{\varepsilon}_{0\_ref}^{doped}$) as a function of nondimensionalized stress ($\sigma_{0\_ref}^{doped}$). Eq. (2-4) is also shown as a reference curve. (b) Plot of the change in strain rate due to doping, χ as a function of $\sigma_{0\_ref}^{doped}$.

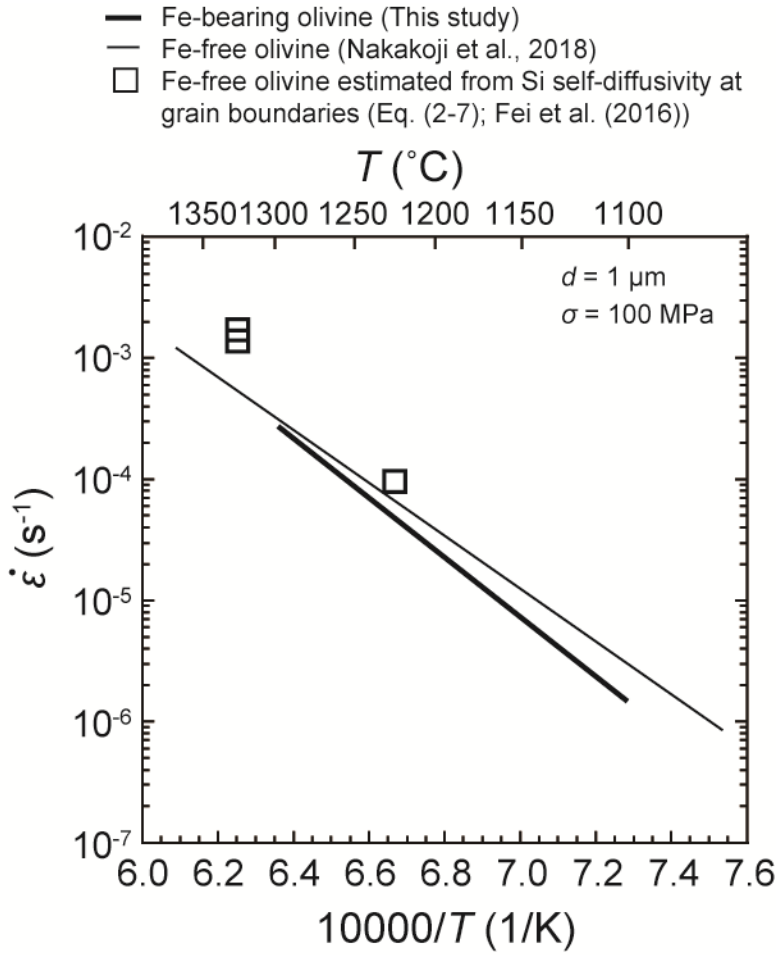

Fig. 2-16. Arrhenius plot of grain-boundary diffusion creep rates for Fe-bearing and Fe-free olivine aggregates. The thick line is calculated from Eq. (1-5) using the flow law parameters determined in this study. The thin line is calculated from Nakakoji et al. (2018) by converting their three-dimensional grain size into a two-dimensional grain size. Points are calculated based on Eq. (2-7) and the predicted self-diffusivity of Si at grain boundaries (Fei et al., 2016).

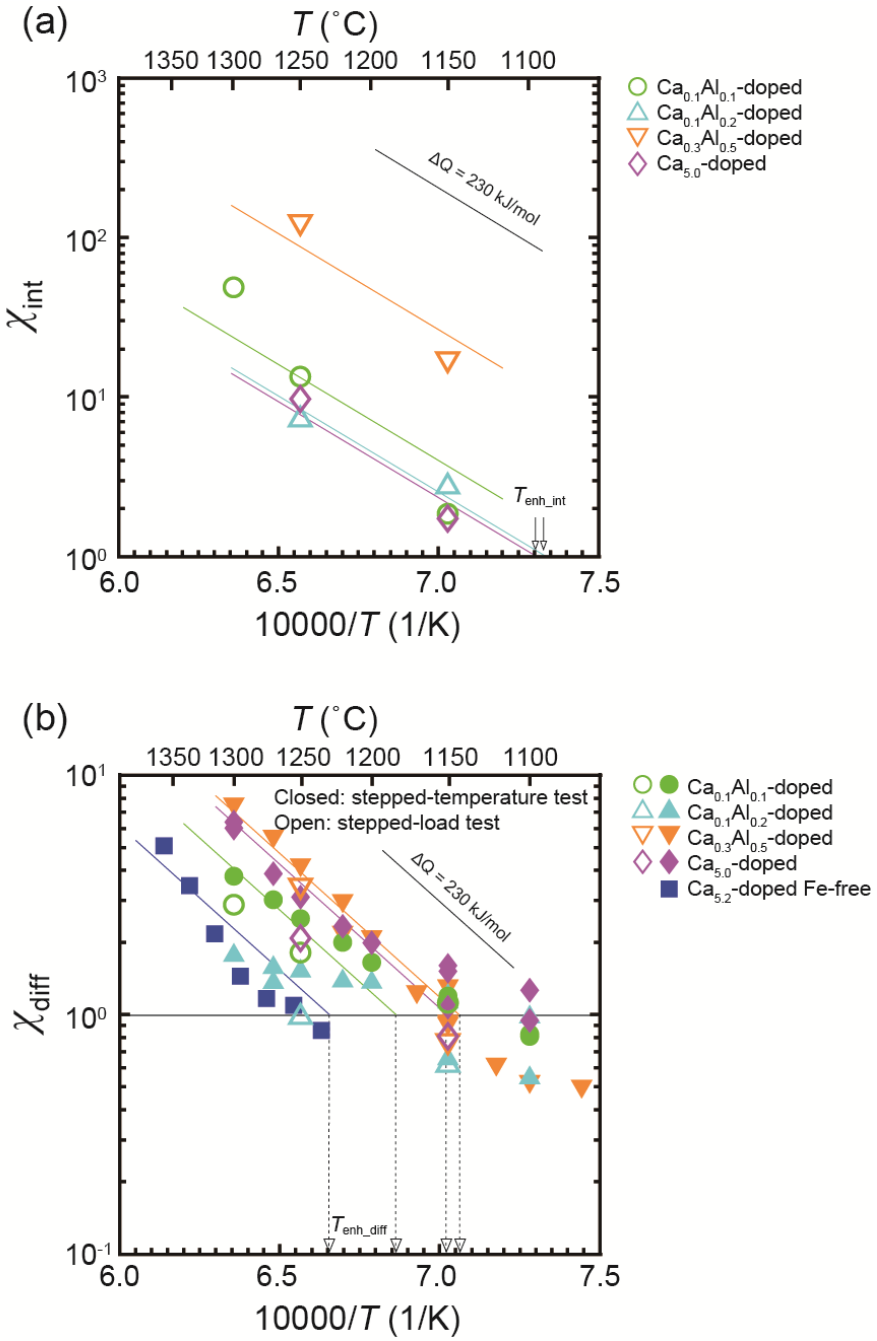

Fig. 2-17. Arrhenius plots of changes in strain rate due to doping for individual deformation processes: (a) interface-controlled creep and (b) diffusion creep. Black lines correspond to $\chi_{\mathrm{int,diff}} \propto \exp\left(-\frac{\Delta Q}{\mathrm{R}T}\right)$, where $\Delta Q = 230$ kJ/mol. Lines of best fit for each doped sample except the $Ca_{0.1}Al_{0.2}$-doped sample are shown as colored lines (see text for details). Temperatures above which doping enhances creep rates (T_{enh}) are indicated by arrows.

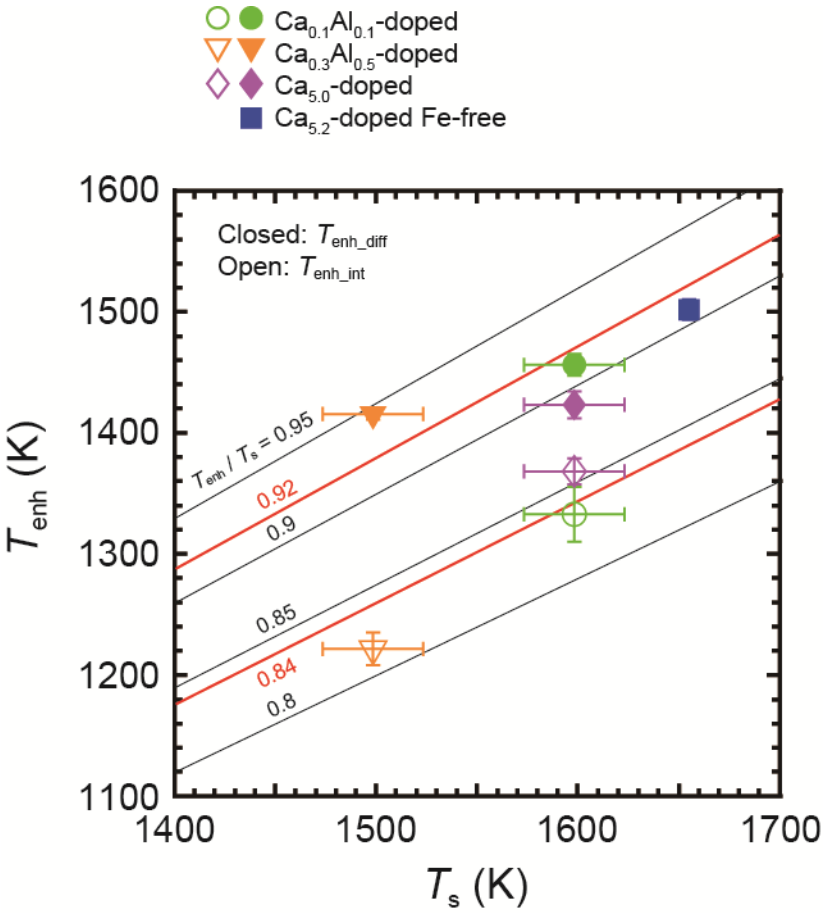

Fig. 2-18. Minimum temperatures for doping-enhanced creep rates (T_{enh}) plotted against sample solidus temperatures (T_s). Black lines correspond to $T_{enh}/T_s = 0.8$, 0.85, 0.9, and 0.95. Red lines correspond to $T_{enh}/T_s = 0.84$ and 0.92. Standard deviations are shown for T_{enh} symbols.

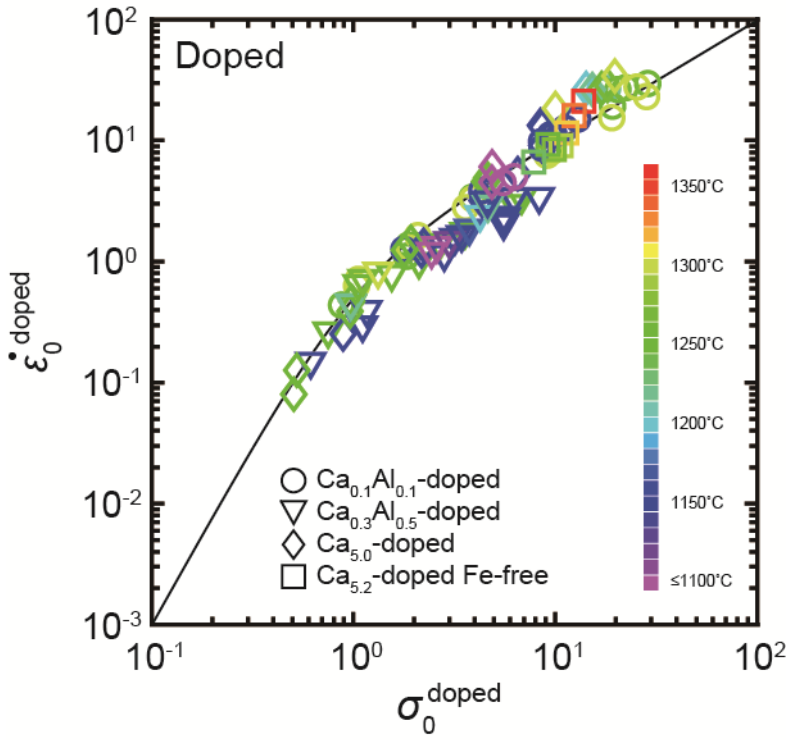

Fig. 2-19. Plot of nondimensionalized strain rate ($\dot{\varepsilon}_0^{\text{doped}}$) as a function of nondimensionalized stress (σ_0^{doped}) calculated from all (σ, $\dot{\varepsilon}$) values of doped samples based on Eqs. (1-8), (2-14), and (2-15) (see text for details). The predicted curve based on Eq. (2-4) is shown by the solid line in the figure.

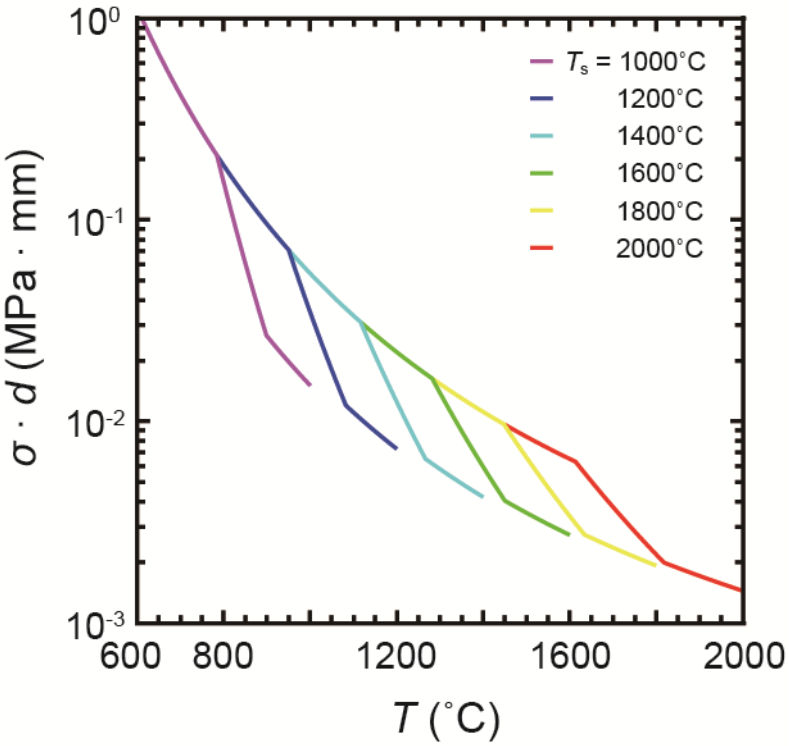

Fig. 2-20. Curves for equal rates of interface-controlled creep and grain-boundary diffusion creep corresponding to $\sigma \cdot d = \left[\frac{A_{\mathrm{diff}}}{A_{\mathrm{int}}}\frac{\chi_{\mathrm{diff}}}{\chi_{\mathrm{int}}}\exp\left(\frac{Q_{\mathrm{int}}-Q_{\mathrm{diff}}}{\mathrm{R}T}\right)\right]^{\frac{1}{2}}$. Curves for $T_{\mathrm{s}} =$ 1000, 1200, 1400, 1600, 1800, and 2000˚C are shown. The lower and upper areas divided by the curve correspond to the regimes of interface-controlled creep and grain-boundary diffusion creep, respectively.

Table 2-1. Olivine samples employed in this study.

Aggregate type	f_{px}	#Mg	CaO (wt%)	Al_2O_3 (wt%)	T_s (°C)
undoped f_{px} = 0	≤0.01	0.90	-	-	1540
undoped f_{px} = 0.1	0.1	0.90	-	-	1540
undoped f_{px} = 0.3	0.3	0.90	-	-	1540
$Ca_{0.1}Al_{0.1}$-doped	0.1	0.90	0.1	0.1	1325 ± 25
$Ca_{0.1}Al_{0.2}$-doped	0.3	0.90	0.1	0.2	> 1350
$Ca_{0.3}Al_{0.5}$-doped	0.3	0.90	0.3	0.5	1225 ± 25
$Ca_{5.0}$-doped	0.3	0.90	5.0	-	1325 ± 25
$Ca_{5.2}$-doped Fe-free	0.2	1.00	5.2	-	1382

Table 2-2. Experimental results of stepped-load tests.

Experiment no.	Samples	T (°C)	σ (MPa)	$\dot{\varepsilon}$ (s^{-1})	Cumulative ε	d_{ini} (μm)	d_{fin} (μm)	d_s (μm)	d_ε (μm)	Total duration (s)	k ($\mu m^4/s$)	α
						Values in parentheses are of pyroxene						
KH-14	undoped f_{px} = 0	1150	19.3	6.46E-07	0.017	1.0	0.91	1.1	0.997	32231	1.4E-05	-3.18
			48.6	1.93E-06	0.028				0.982			
			96.5	3.79E-06	0.042				0.951			
			143.6	5.46E-06	0.052				0.926			
			47.1	1.28E-06	0.060				0.912			
KH-50	undoped f_{px} = 0.3	1250	4.4	6.91E-07	0.019	0.51	0.68	0.57	0.532	12639	3.0E-06	1.13
			9.4	5.04E-06	0.028	(0.35)	(0.48)	(0.41)	0.546			
			19.0	2.79E-05	0.040				0.556			
			46.0	1.31E-04	0.055				0.566			
			92.3	3.48E-04	0.071				0.576			
			44.4	1.10E-04	0.086				0.586			
			17.6	1.70E-05	0.098				0.597			
			8.6	2.35E-06	0.109				0.627			
			18.9	1.74E-05	0.123				0.646			
			46.5	8.68E-05	0.145				0.662			
			18.5	1.39E-05	0.157				0.676			
KH-52	undoped f_{px} = 0	1250	19.4	1.85E-07	0.019	3.5	3.7	3.5	3.54	105390	0.0E+00	0.90
			48.7	6.19E-07	0.030				3.58			
			96.7	1.24E-06	0.041				3.62			
			143.9	2.00E-06	0.051				3.65			
			94.7	1.22E-06	0.062				3.69			
KH-53	undoped f_{px} = 0.1	1250	9.4	9.60E-07	0.024	1.3	1.4	1.3	1.32	28164	0.0E+00	0.91
			19.1	3.67E-06	0.035	(0.67)	(0.62)	(0.62)	1.34			
			47.8	1.51E-05	0.047				1.35			
			94.2	3.69E-05	0.058				1.37			
			140.4	6.15E-05	0.070				1.38			
			18.2	3.07E-06	0.081				1.40			
KH-54	undoped f_{px} = 0.1	1300	4.5	1.08E-06	0.021	1.3	1.3	1.3	1.30	22408	0.0E+00	0.00
			9.4	4.31E-06	0.030	(0.67)	(0.56)	(0.62)	1.30			
			19.0	1.44E-05	0.041				1.30			
			46.6	5.23E-05	0.053				1.30			
			93.1	1.24E-04	0.065				1.30			
			138.9	1.98E-04	0.075				1.30			
			44.7	4.74E-05	0.088				1.30			
			17.8	1.12E-05	0.099				1.30			
			8.6	2.62E-06	0.109				1.30			
KH-55	$Ca_{0.1}Al_{0.1}$-doped	1250	4.4	1.12E-06	0.028	1.3	1.6	1.6	1.48	27284	1.4E-04	0.00
			9.2	3.15E-06	0.037	(0.53)	(0.78)	(0.68)	1.52			
			18.8	7.45E-06	0.046				1.54			
			47.0	2.06E-05	0.057				1.54			
			92.7	4.13E-05	0.070				1.55			
			138.5	6.35E-05	0.081				1.55			
			44.9	1.85E-05	0.091				1.55			
			8.6	2.13E-06	0.101				1.59			
KH-68	$Ca_{0.1}Al_{0.1}$-doped	1300	5.3	1.75E-05	0.034	1.2	1.4	1.4	1.25	3874	4.6E-04	0.00
			10.2	3.66E-05	0.047	(0.73)	(0.79)	(0.86)	1.28			
			18.9	7.15E-05	0.060				1.29			
			46.7	1.76E-04	0.076				1.29			
			91.9	3.25E-04	0.091				1.30			
			136.7	4.87E-04	0.106				1.30			
			43.9	1.59E-04	0.123				1.30			
			17.2	5.68E-05	0.136				1.31			
			8.9	2.47E-05	0.149				1.33			
			4.7	1.04E-05	0.161				1.38			
KH-71	$Ca_{0.3}Al_{0.5}$-doped	1250	12.4	1.98E-04	0.063	0.56	0.64	0.52	0.550	3001	-8.4E-06	0.29
			26.6	4.20E-04	0.127	(0.52)	(0.54)	(0.61)	0.558			
			9.4	1.10E-04	0.159				0.560			
			75.0	1.03E-03	0.349				0.587			
			42.0	5.64E-04	0.426				0.598			
			77.3	9.40E-04	0.561				0.620			
			29.7	3.60E-04	0.667				0.634			
			17.0	1.91E-04	0.720				0.640			

Table 2-2. Continued.

Experiment no.	Samples	T (°C)	σ (MPa)	$\dot{\varepsilon}$ (s^{-1})	Cumulative ε	d_{ini} (μm)	d_{fin} (μm)	d_s (μm)	d_ε (μm)	Total duration (s)	k ($\mu m^4/s$)	α
						Values in parentheses are of pyroxene						
KH-72	$Ca_{0.1}Al_{0.2}$-doped	1250	4.4	2.04E-06	0.030	0.74	0.87	0.83	0.770	17577	9.9E-06	0.46
			9.3	7.90E-06	0.041	(0.52)	(0.68)	(0.69)	0.786			
			18.9	2.40E-05	0.052				0.794			
			45.9	7.80E-05	0.066				0.800			
			91.7	1.72E-04	0.080				0.806			
			17.9	1.86E-05	0.092				0.812			
			4.1	1.04E-06	0.102				0.859			
KH-81	undoped f_{px} = 0.1	1200	10.5	1.40E-06	0.027	0.56	0.65	0.61	0.594	14999	2.7E-06	0.66
			20.2	5.44E-06	0.038	(0.39)	(0.35)	(0.35)	0.608			
			48.4	2.27E-05	0.049				0.616			
			95.0	5.67E-05	0.061				0.621			
			140.9	8.82E-05	0.073				0.627			
			46.5	1.85E-05	0.086				0.633			
			19.0	3.52E-06	0.096				0.646			
KH-87	undoped f_{px} = 0.3	1200	10.5	9.04E-07	0.029	0.65	0.62	0.61	0.635	43830	-9.1E-07	0.14
			20.1	5.35E-06	0.040	(0.50)	(0.52)	(0.51)	0.633			
			48.0	2.99E-05	0.053				0.634			
			94.3	8.24E-05	0.064				0.635			
			140.1	1.38E-04	0.077				0.635			
			93.6	7.67E-05	0.089				0.636			
			45.6	2.28E-05	0.101				0.637			
			18.7	3.28E-06	0.112				0.636			
			9.6	4.50E-07	0.118				0.622			
KH-90	undoped f_{px} = 0.3	1150	15.5	7.95E-07	0.025	0.49	0.52	0.51	0.497	33699	3.0E-07	0.19
			20.3	1.66E-06	0.036	(0.41)	(0.42)	(0.43)	0.501			
			49.1	1.08E-05	0.048				0.505			
			95.8	3.23E-05	0.059				0.507			
			142.0	5.51E-05	0.071				0.508			
			94.2	2.83E-05	0.084				0.509			
			46.9	7.72E-06	0.095				0.511			
			18.9	8.45E-07	0.105				0.517			
KH-91	$Ca_{0.1}Al_{0.2}$-doped	1150	10.5	4.44E-07	0.021	0.62	0.62	0.65	0.626	40565	7.6E-07	-0.50
			20.3	1.65E-06	0.031	(0.47)	(0.43)	(0.49)	0.629			
			49.2	6.72E-06	0.043				0.627			
			96.3	1.64E-05	0.053				0.624			
			142.8	2.61E-05	0.065				0.622			
			94.8	1.50E-05	0.076				0.619			
			47.1	5.34E-06	0.086				0.617			
			19.1	1.01E-06	0.094				0.618			
KH-92	$Ca_{0.3}Al_{0.5}$-doped	1150	10.4	1.31E-06	0.033	0.64	0.60	0.57	0.612	26663	-2.3E-06	0.42
			20.0	3.74E-06	0.043	(0.58)	(0.63)	(0.56)	0.602			
			48.6	1.09E-05	0.055				0.601			
			95.1	2.25E-05	0.065				0.602			
			94.2	2.05E-05	0.078				0.604			
			19.2	2.86E-06	0.084				0.599			
			97.8	2.27E-05	0.098				0.597			
			144.4	3.33E-05	0.110				0.598			
			95.9	1.98E-05	0.123				0.600			
KH-138	undoped f_{px} = 0	1300	20.3	2.25E-06	0.056	2.1	3.2	3.0	2.54	12629	4.9E-03	0.65
			49.4	4.84E-06	0.067				2.75			
			97.2	8.80E-06	0.078				2.86			
			144.0	1.41E-05	0.087				2.92			
			47.7	3.28E-06	0.102				3.13			
KH-143	$Ca_{0.1}Al_{0.1}$-doped	1150	20.4	4.07E-07	0.019	1.3	1.3	1.2	1.31	88598	-8.8E-06	1.05
			49.7	1.25E-06	0.032	(0.53)	(0.54)	(0.58)	1.31			
			98.0	2.72E-06	0.043				1.32			
			145.1	4.46E-06	0.054				1.34			
			95.3	2.82E-06	0.072				1.35			

Table 2-2. Continued.

Experiment no.	Samples	T (°C)	σ (MPa)	$\dot{\varepsilon}$ (s^{-1})	Cumulative ε	d_{ini} (μm)	d_{fin} (μm)	d_s (μm)	d_ε (μm)	Total duration (s)	k ($\mu m^4/s$)	α
						Values in parentheses are of pyroxene						
KH-152	undoped f_{px} = 0	1250	97.3	1.23E-05	0.033	1.5	2.6	1.9	1.68	35717	2.2E-04	2.74
			48.2	4.57E-06	0.047				1.79			
			19.3	1.03E-06	0.060				2.00			
			49.9	2.40E-06	0.075				2.21			
			98.2	4.61E-06	0.087				2.31			
			145.5	6.92E-06	0.099				2.41			
			95.8	4.13E-06	0.114				2.54			
KH-171	$Ca_{5.0}$-doped	1150	97.9	1.52E-05	0.026	0.65	0.73	0.62	0.672	23741	-1.3E-06	1.68
			19.9	1.18E-06	0.038	(0.42)	(0.41)	(0.45)	0.671			
			48.1	5.49E-06	0.050				0.679			
			94.7	1.35E-05	0.061				0.689			
			139.6	2.09E-05	0.072				0.702			
			92.4	1.24E-05	0.085				0.715			
			46.0	4.64E-06	0.098				0.727			
KH-172	$Ca_{5.0}$-doped	1250	44.1	1.69E-04	0.031	0.76	0.84	0.75	0.775	12108	-1.4E-06	0.81
			5.0	4.17E-06	0.040	(0.58)	(0.52)	(0.56)	0.781			
			9.3	1.50E-05	0.049				0.787			
			18.1	4.48E-05	0.064				0.794			
			43.1	1.41E-04	0.077				0.803			
			83.9	2.95E-04	0.091				0.812			
			40.7	1.25E-04	0.104				0.820			
			16.1	3.26E-05	0.117				0.828			
			8.6	9.86E-06	0.128				0.834			
			4.5	1.98E-06	0.140				0.839			

Table 2-3. Experimental results of stepped-temperature tests.

Experiment no.	Samples	T (°C)	σ (MPa)	$\dot{\varepsilon}$ (s^{-1})	Cumulativeε	d_{ini} (μm)	d_{fin} (μm)	d_s (μm)	d_ε (μm)	Total duration (s)	α
						Values in parentheses are of pyroxene					
KH-141	undoped f_{px} = 0.3	1300	95.7	1.99E-04	0.035	1.0	1.2	1.2	1.04	30556	1.55
		1250	97.7	6.21E-05	0.053	(0.80)	(0.92)	(0.82)	1.08		
		1200	98.7	1.81E-05	0.065				1.10		
		1150	99.5	4.65E-06	0.076				1.12		
		1100	99.7	1.06E-06	0.084				1.13		
		1150	99.6	4.27E-06	0.094				1.15		
		1300	97.1	1.72E-04	0.117				1.19		
KH-142	$Ca_{0.3}Al_{0.5}$-doped	1150	97.1	2.14E-05	0.030	0.64	0.97	0.70	0.667	94418	1.61
		1150	48.5	9.10E-06	0.042	(0.58)	(0.93)	(0.61)	0.680		
		1100	50.0	1.17E-06	0.050				0.692		
		1120	50.0	2.39E-06	0.061				0.702		
		1150	49.9	7.90E-06	0.071				0.714		
		1170	49.4	1.75E-05	0.081				0.726		
		1200	48.5	6.07E-05	0.095				0.742		
		1220	48.1	1.33E-04	0.109				0.759		
		1220	9.9	1.95E-05	0.117				0.768		
		1250	9.4	6.89E-05	0.134				0.789		
		1270	9.0	1.29E-04	0.152				0.812		
		1300	9.1	3.03E-04	0.187				0.858		
		1250	9.4	7.43E-05	0.206				0.887		
		1150	49.6	7.59E-06	0.228				0.921		
		1070	49.9	1.79E-07	0.238				0.937		
		1150	49.6	4.55E-06	0.261				0.966		
KH-146	$Ca_{0.1}Al_{0.2}$-doped	1150	97.9	4.37E-06	0.031	1.2	1.1	1.1	1.19	128772	-0.47
		1100	99.6	8.72E-07	0.040	(1.1)	(1.1)	(1.1)	1.18		
		1150	99.5	4.38E-06	0.050				1.17		
		1200	98.5	2.02E-05	0.061				1.17		
		1220	98.1	3.50E-05	0.073				1.16		
		1250	97.6	8.29E-05	0.091				1.15		
		1270	97.3	1.42E-04	0.115				1.14		
		1270	47.6	6.17E-05	0.129				1.13		
		1300	96.5	3.36E-04	0.153				1.12		
		1100	96.5	5.65E-07	0.175				1.11		
		1150	99.3	3.05E-06	0.188				1.10		
KH-148	undoped f_{px} = 0.1	1300	96.2	1.00E-04	0.033	1.6	1.7	1.4	1.63	24913	0.63
		1250	98.2	2.90E-05	0.049	(0.64)	(0.68)	(0.76)	1.65		
		1200	99.3	7.92E-06	0.060				1.66		
		1150	99.5	2.00E-06	0.070				1.67		
		1200	99.3	7.19E-06	0.081				1.68		
		1300	97.4	8.35E-05	0.098				1.70		
KH-149	undoped f_{px} = 0	1300	98.4	5.73E-06	0.024	3.5	3.4	3.7	3.47	102211	-0.43
		1250	99.5	1.36E-06	0.034				3.45		
		1200	99.5	3.33E-07	0.047				3.44		
		1250	99.5	1.37E-06	0.058				3.42		
		1300	99.4	4.93E-06	0.069				3.40		
KH-151	$Ca_{0.1}Al_{0.1}$-doped	1150	98.1	2.41E-06	0.028	1.4	1.7	1.4	1.45	159677	1.33
		1100	99.6	3.83E-07	0.038	(0.83)	(0.87)	(0.84)	1.47		
		1150	99.5	2.17E-06	0.048				1.49		
		1200	99.3	1.15E-05	0.059				1.51		
		1220	98.5	2.18E-05	0.073				1.54		
		1250	97.9	5.52E-05	0.086				1.56		
		1270	97.7	1.01E-04	0.101				1.59		
		1300	97.2	2.31E-04	0.123				1.64		
		1100	99.8	2.56E-07	0.135				1.67		
		1150	99.6	1.48E-06	0.146				1.69		

Table 2-3. Continued.

Experiment no.	Samples	T (℃)	σ (MPa)	$\dot{\varepsilon}$ (s^{-1})	Cumulativeε	d_{ini} (μm)	d_{fin} (μm)	d_s (μm)	d_ε (μm)	Total duration (s)	α
						Values in parentheses are of pyroxene					
KH-174	$Ca_{5.0}$-doped	1150	97.8	4.47E-06	0.032	1.3	1.3	1.3	1.30	161381	0.00
		1100	99.5	8.44E-07	0.045	(0.78)	(0.92)	(0.87)	1.30		
		1150	99.4	4.30E-06	0.057				1.30		
		1200	98.6	2.16E-05	0.070				1.30		
		1220	98.1	4.21E-05	0.083				1.30		
		1250	97.6	1.17E-04	0.098				1.30		
		1270	97.1	2.36E-04	0.115				1.30		
		1300	48.3	3.88E-04	0.148				1.30		
		1300	95.2	7.22E-04	0.166				1.30		
		1100	99.3	6.29E-07	0.182				1.30		
		1150	99.3	3.04E-06	0.196				1.30		
KG-60	$Ca_{5.2}$-doped Fe-free	1356	44.3	4.51E-04	0.107	1.6	1.9	1.7	1.68	36578	0.53
		1335	39.6	1.42E-04	0.225	(1.0)	(0.94)	(1.3)	1.80		
		1315	38.3	5.28E-05	0.261				1.83		
		1295	37.8	2.10E-05	0.283				1.86		
		1275	37.4	1.05E-05	0.290				1.86		
		1255	37.2	5.97E-06	0.294				1.87		
		1235	37.2	2.87E-06	0.296				1.87		

Table 2-4. Analytical results on grain size sensitivity.

Temperature (°C)	Grain size exponent (p)			
	$f_{px} = 0$	$f_{px} \leq 0.1$	$f_{px} = 0.3$	All
1300		3.6 ± 0.3	-	3.3 ± 0.2
1250	3.0 ± 0.1	3.5 ± 0.2	-	3.2 ± 0.1
1200	-	2.9 ± 0.5	2.7 ± 0.1	2.9 ± 0.3
1150	-	-	2.4 ± 0.1	2.3 ± 0.3

Chapter 3

3. Solidus effects

3.1. Analytical methods

3.1.1. Nondimensional space

In *section 2.3.5*, I investigated the doping effect on creep rates using nondimensional stress (σ_0)-strain rate ($\dot{\varepsilon}_0$) space. In essentially the same way, I analyze the data reported in previous studies in this chapter. The σ_0-$\dot{\varepsilon}_0$ space allows all the experimental data to be compared without the need to calibrate them to reference conditions, such as a certain grain size and stress, as in Fig. 1-1.

Each (σ, $\dot{\varepsilon}$) reported in the previous studies (Table 1-1) was transformed to (σ_0, $\dot{\varepsilon}_0$) based on Eq. (1-8). The ($\sigma^{*\mathrm{ref}}$, $\dot{\varepsilon}^{*\mathrm{ref}}$) data are calculated from Eqs. (1-6), (1-7) by substituting the d and T values at which each (σ, $\dot{\varepsilon}$) was acquired (Table 1-1). In this calculation, I used the flow law parameters (i.e., A_{int}, A_{diff}, Q_{int}, Q_{diff}, n_{int}, and p_{diff}) determined for my undoped (= reference) olivine (Eq. (2-6) and (2-8)). I refer to such (σ_0, $\dot{\varepsilon}_0$) values from previous studies as ($\sigma_{0\_\mathrm{ref}}^{\mathrm{Data}}$, $\dot{\varepsilon}_{0\_\mathrm{ref}}^{\mathrm{Data}}$) hereafter. Here I introduce a term χ that describes the ratio of $\dot{\varepsilon}_{0\_\mathrm{ref}}^{\mathrm{Data}}$ to $\dot{\varepsilon}_0$ ($\sigma_{0\_\mathrm{ref}}^{\mathrm{Data}}$), which is obtained by substituting $\sigma_{0\_\mathrm{ref}}^{\mathrm{doped}}$ with $\sigma_{0\_\mathrm{ref}}^{\mathrm{Data}}$ in Eq. (2-5):

$$\chi \equiv \frac{\dot{\varepsilon}_{0\_\mathrm{ref}}^{\mathrm{Data}}}{\dot{\varepsilon}_0\,(\sigma_{0\_\mathrm{ref}}^{\mathrm{Data}})}. \qquad (3\text{-}1)$$

The χ is expected to be related to χ_{diff} and χ_{int} as Eq. (2-10) with substituting $\sigma_{0\_\mathrm{ref}}^{\mathrm{doped}}$ with $\sigma_{0\_\mathrm{ref}}^{\mathrm{Data}}$.

3.1.2. Sample solidus

3.1.2.1. Dry conditions

The T_{s} of dry samples is referred to as $T_{\mathrm{s}}^{\mathrm{dry}}$ hereafter. A $T_{\mathrm{s}}^{\mathrm{dry}}$ of 1540˚C was used for RG-olivine, which was estimated from the phase diagram for the MgO-FeO-SiO_2 system at 0.1 MPa (Bowen &, Schairer 1935) (Table 1-1). The $T_{\mathrm{s}}^{\mathrm{dry}}$ at a confining pressure (P) of 300 MPa should be higher than 1540˚C, which signifies that all FJ data was obtained at $< 0.92 \cdot T_{\mathrm{s}}$. The $T_{\mathrm{s}}^{\mathrm{dry}}$ of SC-olivine is assumed to be the same as $T_{\mathrm{s}}^{\mathrm{dry}}$ of spinel lherzolite, which is a function of P (in GPa) (Hirschmann, 2000):

$$T_{\mathrm{s}}^{\mathrm{dry}}(^{\circ}\mathrm{C}) = -5.104 \cdot P^2 + 132.899 \cdot P + 1120.661. \quad (3\text{-}2)$$

The $T_{\mathrm{s}}^{\mathrm{dry}}$ of SC-olivine at P = 300 MPa was calculated as 1160˚C based on Eq. (3-2). HK reported that SC-olivine to which basaltic glass was added was free from melt at 1150˚C, while a small amount of melt was discovered in glass-free SC-olivine (corresponding to SC-olivine in this paper) at 1200˚C and 300 MPa. Inter- and intra-granular melt-like components in mantle xenoliths from San Carlos were previously reported by Hiraga & Kohlstedt (2009). Contamination, especially by the intra-granular component in olivine, is likely inevitable during sample synthesis from SC-olivine. All of the above points support that the solidus of SC-olivine can be determined by Eq. (3-2). Because partial melting of spinel lherzolite produces basaltic melt, the $T_{\mathrm{s}}^{\mathrm{dry}}$ of melt-bearing RG-olivine is considered to correspond to the temperature determined by Eq. (3-2). All estimated $T_{\mathrm{s}}^{\mathrm{dry}}$ values are listed in Table 1-1.

3.1.2.2. Wet conditions

The T_{s} of wet samples is referred to as $T_{\mathrm{s}}^{\mathrm{wet}}$ hereafter. I estimated $T_{\mathrm{s}}^{\mathrm{wet}}$ of the wet SC-olivine of MK using the cryopscopic equation proposed by Hirschmann et al. (2009):

$$T_{\mathrm{s}}^{\mathrm{wet}}(\mathrm{K}) = \frac{T_{\mathrm{s}}^{\mathrm{dry}}}{1-\frac{\mathrm{R}}{M\Delta S_{\mathrm{perid}}^{\mathrm{fusion}}}\ln\left(1-X_{\mathrm{OH^-}}^{\mathrm{melt}}\right)}, \quad (3\text{-}3)$$

where $T_{\mathrm{s}}^{\mathrm{dry}}$ is the solidus of SC-olivine (Eq. (3-2)), M is the number of grams in one mole of silicate (59 g/mol), $\Delta S_{\mathrm{perid}}^{\mathrm{fusion}}$ is the entropy of fusion of (mantle) peridotite per unit mass (0.4 J/K/g) (Kojitani & Akaogi, 1997), and $X_{\mathrm{OH^-}}^{\mathrm{melt}}$ is the mole fraction of dissolved H_2O in melt. We can convert $C_{\mathrm{H_2O}}^{\mathrm{melt}}$ (weight fraction of H_2O in the melt reported in parts per million: μg/g) to $X_{\mathrm{OH^-}}^{\mathrm{melt}}$ using:

$$X_{\mathrm{OH^-}}^{\mathrm{melt}} = \frac{59C_{\mathrm{H_2O}}^{\mathrm{melt}}}{9\times10^6+50C_{\mathrm{H_2O}}^{\mathrm{melt}}}. \quad (3\text{-}4)$$

This relationship assumes that all the water is entirely dissociated to hydroxyl groups in the melt. $C_{\mathrm{H_2O}}^{\mathrm{melt}}$ is not reported in MK, thus, we estimated it from the weight fraction of water in the olivine (lattice), $C_{\mathrm{H_2O}}^{\mathrm{ol}}$ (in μg/g), and the partition coefficient of water between olivine and melt, $KD_{\mathrm{H_2O}}^{\mathrm{ol-melt}}$, which is a function of P (see Appendix E for its derivation):

$$KD_{\mathrm{H_2O}}^{\mathrm{ol-melt}} = 6 \times 10^{-4} \times \left(\frac{P\ (\mathrm{MPa})}{300}\right)^{0.5}. \quad (3\text{-}5)$$

The $C_{\mathrm{H_2O}}^{\mathrm{ol}}$ has been well examined at different experimental conditions and is known to follow (Zhao et al., 2004):

$$C_{\mathrm{H_2O}}^{\mathrm{ol}} = \mathrm{A} \cdot f_{\mathrm{H_2O}} \exp\left(-\frac{E+PV}{\mathrm{R}T}\right) \exp\left(\frac{\mathrm{B}X_{\mathrm{Fa}}}{\mathrm{R}T}\right). \quad (3\text{-}6)$$

where A is a coefficient (= 3.5 μg/g/MPa), $f_{\mathrm{H_2O}}$ is water fugacity (MPa), which can be approximated as P (at <500 MPa) under water-saturated conditions, $\mathrm{B} = 97$ kJ/mol, $E = 50$ kJ/mol, $V = 10 \times 10^{-6}$ m^3/mol, and X_{Fa} is the mole fraction of fayalite (X_{Fa} = 0.1 in this study). The A value includes a newly proposed calibration factor to convert the OH^- absorption in unpolarized FTIR (Fourier transform infrared) spectra to $C_{\mathrm{H_2O}}^{\mathrm{ol}}$ (Withers et al., 2012) and a unit conversion of 10^6 H/Si used in Zhao et al. (2004) to μg/g. I calculated $C_{\mathrm{H_2O}}^{\mathrm{ol}}$ values for the wet SC-olivine of MK using Eq. (3-6), which gives $T_{\mathrm{s}}^{\mathrm{wet}}$ values of 1025˚C, 1007˚C, and 1013˚C at P of 100, 300, and 450 MPa, respectively (Table 1-1).

3.2. Results

3.2.1. Comparisons

The calculated ($\sigma_{0\_\mathrm{ref}}^{\mathrm{Data}}$, $\dot{\varepsilon}_{0\_\mathrm{ref}}^{\mathrm{Data}}$) values of the previous studies are plotted in Fig. 3-1a. The data for the same temperatures and pressures in the same studies are distributed along slopes that correspond to $n \approx 1$ for $\dot{\varepsilon}_0 \propto {\sigma_0}^n$ in the σ_0-$\dot{\varepsilon}_0$ space. The data for the RG-olivine and SC-olivine of BK lie close to the reference curve (Eq. (2-4)), while the others plot well above the curve. The χ values based on Eq. (3-1) are plotted against $\sigma_{0\_\mathrm{ref}}^{\mathrm{Data}}$ in Fig. 3-1b. Despite the large variation in χ, values from the same temperatures and pressures in the same studies exhibit nearly constant values irrespective of $\sigma_{0\_\mathrm{ref}}^{\mathrm{Data}}$. The χ values from RG-olivine at all temperatures are ~1, while the χ values from melt-bearing RG-olivine are 20-30. The χ values from SC-olivine (excluding the BK results) range greatly, i.e., from 10 to 400. Larger χ values are found for wet SC-olivine for higher P at a constant temperature of 1250˚C (Fig. 3-1b).

3.2.2. Effect of sample solidus

The χ values described above were analyzed based on the experimental temperature normalized by the sample solidus (T/T_{s}), as shown in Fig. 3-2. I also show (T/T_{s}, χ)

values calculated from my undoped and doped olivine based on Eqs. (1-8) and (2-5) in the figure. I limited the plot to data collected from stepped-temperature tests that were aimed at deforming the samples well within the diffusion creep regime (see *chapter 2*). I used a T_s of 1540˚C (Bowen & Schairer, 1935) and the experimentally determined T_s for my undoped and doped olivine, respectively, all of which are listed in Table 2-1. The T/T_s of RG-olivine and my undoped olivine are all <0.9, while T/T_s is >1 for SC-olivine except for one datum of BK. The large differences in T_s of RG-olivine and SC-olivine resulted in few data at T/T_s of 0.9–1.1, which is filled by the data from my doped olivine. Overall, the results allow us to examine the relationship between χ and T/T_s at $T = T_s \pm 0.2 \cdot T_s$, which is a wide-enough range to understand the characteristics of olivine creep from sub-solidus to super-solidus conditions.

The χ values are independent of T/T_s with a value of ~1 at $T/T_s \leq 0.92$, while the values increase with T/T_s at $T/T_s > 0.92$, except for one datum of BK (Fig. 3-2). The predicted T/T_s-χ_{diff} curves (Eq. (2-13)) for representative T_s of 1000, 1160, and 1350˚C are included in the figure. The T/T_s-χ_{diff} relationship explains the majority of the (T/T_s, χ) values, including the values from wet SC-olivine, although the χ values from the SC-olivine of HK are much larger than the predictions.

3.3. Discussion

3.3.1. Applicability of olivine diffusion creep law

A single deformation mechanism, diffusion creep, dominated in all the previous experiments, which is well supported by the similar χ values from the same temperatures and pressures of the same studies (Fig. 3-1b) and the linear changes in $\dot{\varepsilon}_{0\_ref}^{Data}$ with $\sigma_{0\_ref}^{Data}$ (Fig. 3-1a). This conclusion is consistent with the results of substituting the experimental conditions in the T (K)-$\sigma \cdot d$ (MPa · mm) relationship for the mechanism of grain-boundary diffusion creep and interface-controlled creep (see Fig. 2-20). All the findings indicate that I can approximate the χ values from RG-olivine and SC-olivine as χ_{diff} values in Eq. (2-11) (Figs. 3-1 and 3-2).

The RG-olivine is pure in that it contains no elements other than Mg, Fe, Si. and O, at least above a ppm level. This is comparable to the chemical state of my undoped olivine (see *chapter 2*), but different from the state of SC-olivine. Although the mechanical data for my undoped olivine and RG-olivine were obtained in very different experimental environments, the ($\sigma_{0\_ref}^{Data}$, $\dot{\varepsilon}_{0\_ref}^{Data}$) values from RG-olivine closely follow the reference olivine curve (Fig. 3-1a) as well as their χ_{diff} values of ~1 (Fig. 3-1b), indicating that both olivines are identical in terms of their diffusion creep properties.

In *chapter 2*, I considered the origin of $\chi_{diff} >> 1$ to be grain-boundary disordering,

which starts to affect diffusion creep rates at a temperature of $0.92 \cdot T_s$. The disordering is promoted by grain-boundary segregation of incompatible elements such as Ca and Al, both of which are present in SC-olivine (Hiraga et al., 2003) (see the discussion in *chapter 2*). As seen in Fig. 3-2, all previous deformation experiments using SC-olivine were conducted at T/T_s>0.92, while all the experiments using RG-olivine were conducted at T/T_s<0.92. Thus, no previous experiments have been conducted across $0.92 \cdot T_s$, which partially explains why it has been difficult to identify the critical temperature of $0.92 \cdot T_s$ in previous studies. The χ_{diff} values from my doped olivine, which were obtained across $0.92 \cdot T_s$, do explain (or bridge) the different χ_{diff} values from RG-olivine and SC-olivine (Fig. 3-2).

The explanation of the creep rates of SC-olivine based on grain-boundary disordering is incompatible with the previous statistical determination of grain size exponent of 2 (Jain et al., 2018, 2019), which indicates lattice diffusion creep. I do not have a clear explanation on the different conclusions of diffusion creep mechanism; however I want to point out that the experimentally observed diffusion creep rates are too fast to be explained by the Si lattice self-diffusivity in olivine (Dohmen et al., 2002; Fei et al., 2012) even at T/T_s<0.92 (Nakakoji & Hiraga, 2018; Fig. 2-16).

The presence of melt contributes to mass transport and hence increases the creep rate. However, my χ_{diff}-T/T_s relationship holds even at T/T_s>1, which can be seen from the χ_{diff} values in Fig. 3-2. Strongly temperature-dependent chemical enhancement of grain-boundary processes, which continues when T/T_s>1, seems to overwhelm the melt-weakening effect when melt production rates increase slowly with T (see the discussion in *chapter 2*). Basaltic glass is enriched in incompatible elements, including Ca and Al, that segregate at olivine grain boundaries (Hiraga et al., 2002). Grain boundaries in melt-bearing RG-olivine are no longer pure in terms of such elements, resulting in it having a lower predicted strength based on my grain-boundary-disordering model (Eq. (2-13)) (Fig. 3-2). I see that the T/T_s-χ_{diff} relationship even explains the χ_{diff} values from wet SC-olivine (MK) at T/T_s of ~1.2. These χ_{diff} values occur at much higher T/T_s than those for which I confirmed the relationship to hold in *chapter 2*. The absence of any reported melt phase in MK does not rule out the presence of a very small amount of melt. This may be the reason that their data can be well explained by a grain-boundary-disordering model without invoking melt effects in their diffusion creep measurements. A more detailed examination of "wet" creep data based on a grain-boundary-disordering model will be performed in the next section.

I do not have a good explanation of why the SC-olivine of HK is weaker than its predicted strength, as well as one datum from BK that shows a lack of weakening even at

$T \gg 0.92 \cdot T_s$ (Fig. 3-2). Even for the same dry SC-olivine, the χ_{diff} values of SC-olivine from KPF are well explained by my model. I predict an activation energy of 700 kJ/mol for creep at $>0.92 \cdot T_s$, which is quite different from the values of 375 ± 35 and ~300 kJ/mol reported for dry and wet SC-olivine, respectively. These lower activation energies can be inferred from the negative trend of χ_{diff} with increasing T/T_s of dry SC-olivine (Fig. 3-2). Korenaga and Karato (2008) reported a possible range of activation energies, which is large enough to include both the previously estimated values and my predicted value of 700 kJ/mol. I was not able to extract χ_{diff} from the results of torsion experiments on fine-grained olivine aggregates (synthesized from Balsam Gap dunite; Jackson County, North Carolina) at temperatures between 1225 and 1285˚C (Gribb & Cooper, 1998); however, it is interesting to see that they obtained an activation energy of grain-boundary diffusion creep of 700 ± 30 kJ/mol and attributed such a high value to the sample enrichment in Ca, which segregates at olivine grain boundaries. Accurate measurements of the activation energy of diffusion creep of SC-olivine as well as grain size are expected in future studies. I also propose to examine whether SC-olivine creep becomes comparable to the reference olivine creep at T/T_s<0.92 (Eq. (2-6)), which corresponds to <1045˚C at 300 MPa for dry SC-olivine (Eq. (3-2)).

Each $(\sigma, \dot{\varepsilon})$ reported in the previous studies was normalized by $(\sigma^*, \dot{\varepsilon}^*)$ (Eqs. (2-14) and (2-15)) with the d and T values at which the $(\sigma, \dot{\varepsilon})$ was acquired (Table 1-1). I refer to such normalized $(\sigma, \dot{\varepsilon})$ values for the previous studies as $(\sigma_0^{Data}, \dot{\varepsilon}_0^{Data})$, which are plotted in Fig. 3-3. My data on undoped and doped olivine are included in this figure. In this plot, I use $\chi_{diff} = \chi_{int} = 1$ for the data from both my undoped and RG-olivine based on the conclusion that they have the same mechanical properties. Nearly all the data from the previous studies plot at $\sigma_0 \gg 1$, which indicates essentially zero contribution of interface-controlled creep in the mechanical data of the previous studies. The majority of the calculated $(\sigma_0^{Data}, \dot{\varepsilon}_0^{Data})$ follow the predicted σ_0-$\dot{\varepsilon}_0$ curve. I also plot the reported $\dot{\varepsilon}$ $(= \dot{\varepsilon}_{rep})$ versus its predicted $\dot{\varepsilon}$ $(= \dot{\varepsilon}_{pred})$ based on Eqs. (2-6), (2-8), (2-11), (2-12), and (2-13) by substituting the experimental temperature, grain size, stress, and sample solidus in Fig. 3-4. Despite some exceptions, I can reproduce different $\dot{\varepsilon}_{rep}$ ranging over almost 4 orders of magnitude. The misfits between the data and their predicted values seem to be independent of temperature, stress, and strain rate (Figs. 3-3 and 3-4), which supports the flow law parameters determined in *chapter 2*.

3.3.2. Water weakening

As a strongly incompatible element, water (hydrogen) is predicted to segregate at olivine grain boundaries (Hiraga & Kohlstedt, 2007). Water is also known to effectively reduce

T_s; thus, I can expect water to affect creep rates in a manner similar to Ca and Al. Indeed, I could interpret the χ_{diff} values of ~100 from wet SC-olivine by extrapolating the T/T_s-χ_{diff} relationship (Eq. (2-13)).

Classically, the effect of water on creep rates, often referred to as water weakening, is interpreted based on changes in point defect chemistry that occur when water is dissolved in olivine. Therefore, this weakening is expected to be a function of $C_{H_2O}^{ol}$ (Mei & Kohlstedt, 2000a). Referring to $\dot{\varepsilon}^{dry}$ and $\dot{\varepsilon}^{wet}$ for $\dot{\varepsilon}$ under water-free (dry) conditions and in the presence of water (wet), respectively, at the same grain sizes, temperatures, and stress, $\dot{\varepsilon}^{wet}/\dot{\varepsilon}^{dry}$ has been found to vary $\propto {f_{H_2O}}^r$ or ${C_{H_2O}^{ol}}^r$, where r is ~1 (Mei & Kohlstedt, 2000a). Here I use a representative (fixed) $\dot{\varepsilon}^{dry}$ of 4×10^{-7} s^{-1} at $\sigma = 29$ MPa, $d = 12$ μm, and $T = 1248$˚C from SC-olivine reported in HK (Table 1-1) and $\dot{\varepsilon}^{wet}$ at 1250˚C from wet SC-olivine reported in MK (Table1-1), which are calibrated to $\dot{\varepsilon}^{wet}$ at the same stress and grain size using stress and grain size exponents of 1 and 3, respectively. Such values were used to obtain $\dot{\varepsilon}^{wet}/\dot{\varepsilon}^{dry}$ which was plotted against the estimated $C_{H_2O}^{ol}$ at which $\dot{\varepsilon}^{wet}$ was measured (Eq. (3-6)) (Fig. 3-5). The $C_{H_2O}^{ol}$ values are listed in Table 1-1. The plots in Fig. 3-5 follow the relationship $\dot{\varepsilon}^{wet}/\dot{\varepsilon}^{dry} \propto C_{H_2O}^{ol}$ presented by Mei and Kohlstedt (2000a). I examine whether the T/T_s-χ_{diff} relationship (Eq. (2-13)) reproduces the previous results of $C_{H_2O}^{ol}$-$\dot{\varepsilon}^{wet}/\dot{\varepsilon}^{dry}$. Data from both dry and wet SC-olivine by HK and MK, respectively, were collected well above $0.92 \cdot T_s$ (Fig. 3-2) such that $\dot{\varepsilon}^{wet}/\dot{\varepsilon}^{dry}$ is related to T_s^{wet} (Eq. (2-13)) as

$$\frac{\dot{\varepsilon}^{wet}}{\dot{\varepsilon}^{dry}} = \exp\left[\frac{\Delta Q}{0.92 \cdot R} \cdot \left(\frac{1}{T_s^{wet}} - \frac{1}{T_s^{dry}}\right)\right], \qquad (3\text{-}7)$$

where T_s^{dry} = 1160˚C for SC-olivine (see *section 3.1.2.1*). T_s^{wet} can be expressed in terms of $C_{H_2O}^{ol}$ based on Eqs. (3-2)–(3-6) to obtain the $C_{H_2O}^{ol}$-$\dot{\varepsilon}^{wet}/\dot{\varepsilon}^{dry}$ curve shown in Fig. 3-5. My prediction overestimates the intensity of weakening at low $C_{H_2O}^{ol}$; however, $\dot{\varepsilon}^{wet}/\dot{\varepsilon}^{dry}$ at high $C_{H_2O}^{ol}$ and similar $C_{H_2O}^{ol}$ effects on olivine creep rates are well reproduced.

Recently, Fei et al. (2016) questioned the existence of water weakening based on a self-diffusion study. $\dot{\varepsilon}^{wet}/\dot{\varepsilon}^{dry}$ can be estimated from Si self-diffusivity at olivine grain boundaries, δD_{GB} (δ: grain-boundary width; D_{GB}: Si grain-boundary self-diffusivity) based on $\dot{\varepsilon}^{wet}/\dot{\varepsilon}^{dry} = \delta D_{GB}^{wet}/\delta D_{GB}^{dry}$, which should hold for diffusion creep. Fei et al. (2016) reported δD_{GB}^{wet} and δD_{GB}^{dry} in pyroxene-buffered Fe-free olivine at constant P of 8 GPa and T ranging from 927 to 1327˚C. Here I limit the use of their δD_{GB} to

1327˚C only, which permits us to predict $\dot{\varepsilon}^{\mathrm{wet}}/\dot{\varepsilon}^{\mathrm{dry}}$ based on T_{s}. I use the geometrical mean of the reported values of $\delta D_{\mathrm{GB}}^{\mathrm{dry}}$, which were obtained from an aggregate with $C_{\mathrm{H_2O}}^{\mathrm{ol}}$<1 μg/g (samples No. 5k2590B, 5k2590T, and H3735B). The measured $\delta D_{\mathrm{GB}}^{\mathrm{wet}}$ from various $C_{\mathrm{H_2O}}^{\mathrm{ol}}$ of ≥8 μg/g were normalized by the above value of $\delta D_{\mathrm{GB}}^{\mathrm{dry}}$; this ratio corresponds to $\dot{\varepsilon}^{\mathrm{wet}}/\dot{\varepsilon}^{\mathrm{dry}}$. Here $C_{\mathrm{H_2O}}^{\mathrm{ol}}$ corresponds to the reported values in Fei et al. (2016). I can see that $\dot{\varepsilon}^{\mathrm{wet}}/\dot{\varepsilon}^{\mathrm{dry}}$ is ~1 up to $C_{\mathrm{H_2O}}^{\mathrm{ol}}$ of 30 μg/g (Fig. 3-5). Based on the analytical results in Fig. 3-5, Fei et al. (2016) concluded a very small water-weakening effect in olivine. The $T_{\mathrm{s}}^{\mathrm{dry}}$ for the sample used in Fei et al. (2016) at P of 8 GPa is estimated as ~2000˚C based on phase equilibrium studies of the MgO-SiO_2 system (compiled by Gasparik, 2003). At 8 GPa and 1327 ˚C, $KD_{\mathrm{H_2O}}^{\mathrm{ol-melt}}$ in the system was approximated as 2×10^{-3} based on the experimentally determined $KD_{\mathrm{H_2O}}^{\mathrm{ol-melt}}$ values of 1.2×10^{-3} and 2.4×10^{-3} at P of 6 and 9 GPa, respectively, at 1325˚C (Bali et al., 2008). By substituting $T_{\mathrm{s}}^{\mathrm{dry}}$ and $C_{\mathrm{H_2O}}^{\mathrm{melt}}$ which is calculated from $C_{\mathrm{H_2O}}^{\mathrm{ol}}/KD_{\mathrm{H_2O}}^{\mathrm{ol-melt}}$, where $C_{\mathrm{H_2O}}^{\mathrm{ol}}$ is the reported value in Fei et al. (2016), into Eqs. (3-3) and (3-4), I obtain $T_{\mathrm{s}}^{\mathrm{wet}}$ for each $C_{\mathrm{H_2O}}^{\mathrm{ol}}$. The calculation reveals T/T_{s} of 0.78 even at $C_{\mathrm{H_2O}}^{\mathrm{ol}}$ of 100 μg/g, indicating that all the experiments of Fei et al. (2016) were conducted at $T/T_{\mathrm{s}} < 0.92$. Thus, I predict that $\dot{\varepsilon}^{\mathrm{wet}}/\dot{\varepsilon}^{\mathrm{dry}} = 1$ for their results (Eq. (2-13), Fig. 3-5).

Overall, my model is able to explain the contradictory conclusions on water weakening in the previous studies. I propose that the data of MK and Fei et al. are from olivine aggregates with and without grain-boundary disordering, respectively. Water weakening is a manifestation of the grain-boundary-disordering effect on the creep rate and its magnitude increases with water content through the reduction of T_{s}.

3.3.3. Comparison with pre-melting hypothesis by Yamauchi & Takei (2016)

The enhancement of diffusion creep rates through grain-boundary structural transitions was first demonstrated and linked to mechanical properties of the mantle by Yamauchi and Takei (2016). Using borneol + diphenylamine aggregates, which is a good analogue for eutectic peridotite (Takei, 2000), Yamauchi & Takei (2016) measured elasticity, anelasticity, and viscosity at temperatures ranging below and above T_{s}. They found that the temperature dependence of grain-boundary diffusion creep became larger at $>0.94 \cdot T_{\mathrm{s}}$ and interpreted this in terms of grain-boundary pre-melting or disordering (Cantwell et al., 2014). They parameterized the enhancement of the creep rate, which essentially corresponds to χ_{diff} in this study. Their semi-empirically derived equations to express the enhancement can be rewritten in a similar form to that of Eq. (2-13) as

$$\chi_{\mathrm{diff}} = 1 \qquad \text{at } T < 0.94 \cdot T_{\mathrm{s}} \qquad \text{(3-8a)}$$

$$\chi_{\mathrm{diff}} = \exp\left[-\frac{\Delta Q}{\mathrm{R}}\left(\frac{1}{T} - \frac{1}{0.94T_{\mathrm{s}}}\right)\right] \qquad \text{at } 0.94 \cdot T_{\mathrm{s}} \leq T < T_{\mathrm{s}} \qquad \text{(3-8b)}$$

$$\chi_{\mathrm{diff}} = \gamma \cdot \exp(\alpha\phi) \qquad \text{at } T \geq T_{\mathrm{s}} \qquad \text{(3-8c)}$$

where $\Delta Q = \frac{47}{3} \cdot \mathrm{R} \cdot T_{\mathrm{s}} \cdot \ln\gamma$, γ (= 5) represents the disordering effect at T_{s}, ϕ is the melt fraction, and α (≈ 30) represents the melt-fraction dependence (Mei et al., 2002; Zimmerman & Kohlstedt, 2004). Eq. (3-8c) represents the reduction of viscosity due to the melt phase. We can think of our relationship in Eq. (2-13) as a modified version of Eq. (3-8) by changing $0.94 \cdot T_{\mathrm{s}}$ to $0.92 \cdot T_{\mathrm{s}}$, ΔQ to a constant value of 230 kJ/mol, and applying Eq. (3-8b) instead of Eq. (3-8c) even at $T \geq T_{\mathrm{s}}$. We showed that ΔQ is constant for different T_{s} in *chapter 2*, while a similar ΔQ of 270 kJ/mol is obtained by using a representative T_{s} of 1000˚C in Eq. (3-8b). We also showed that the effect of melt is negligible compared to the grain-boundary-disordering effect on the creep rate at $T \geq T_{\mathrm{s}}$. A ϕ of ~0.1 is needed to explain χ_{diff} values of >100 from wet SC-olivine based on Eq. (3-8c) (Fig. 3-2), which seems to be inconsistent with the nominally melt-free conditions reported by MK.

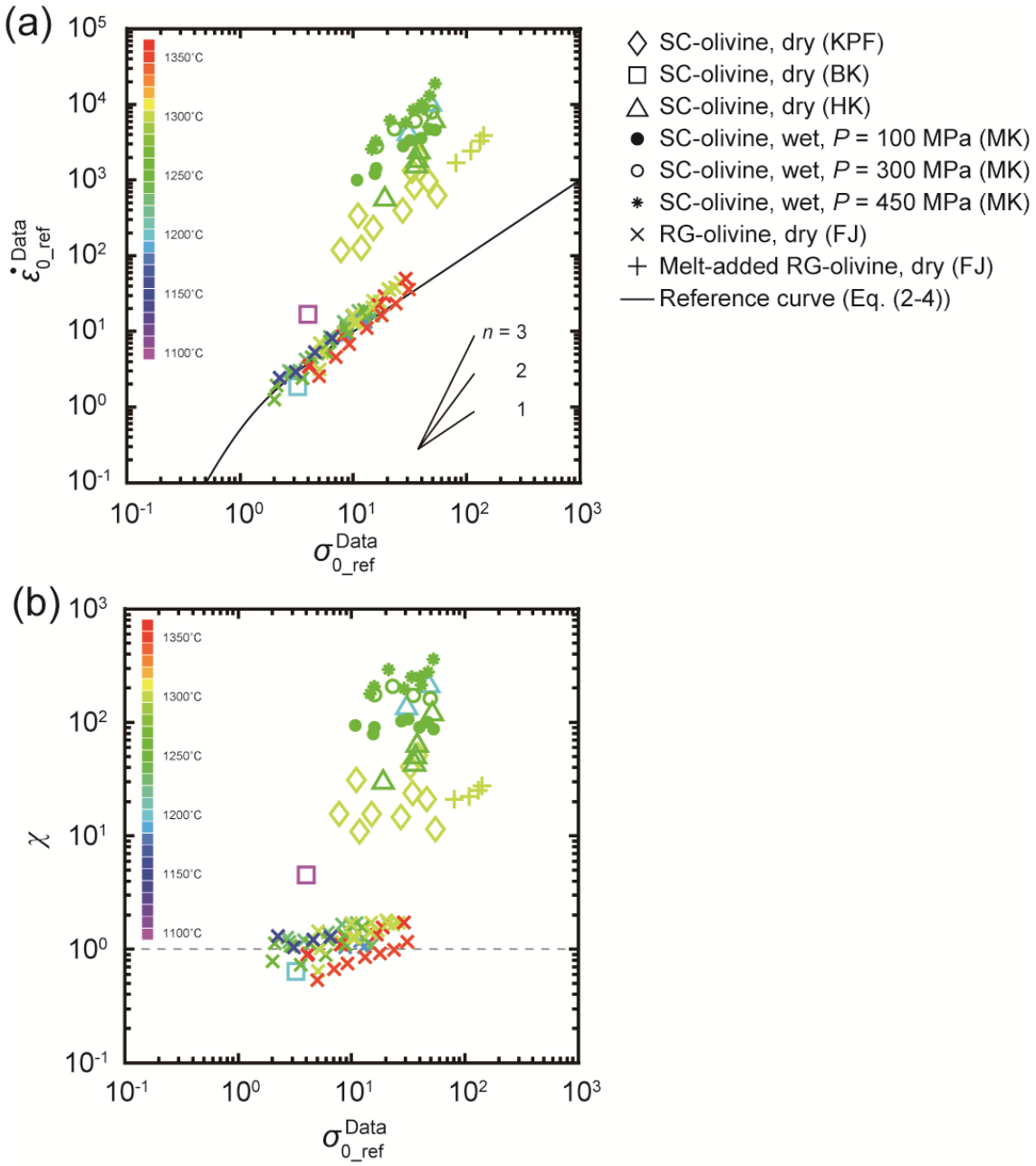

Fig. 3-1. Comparison of the previous experimental results. (a) Plot of nondimensionalized strain rate ($\dot{\varepsilon}_{0\_ref}^{Data}$) as a function of nondimensionalized stress ($\sigma_{0\_ref}^{Data}$) calculated from the previously reported (σ, $\dot{\varepsilon}$) values. The reference curve calculated from Eq. (2-4) is also shown. (b) Plot of χ values (Eq. (3-1)) versus $\sigma_{0\_ref}^{Data}$.

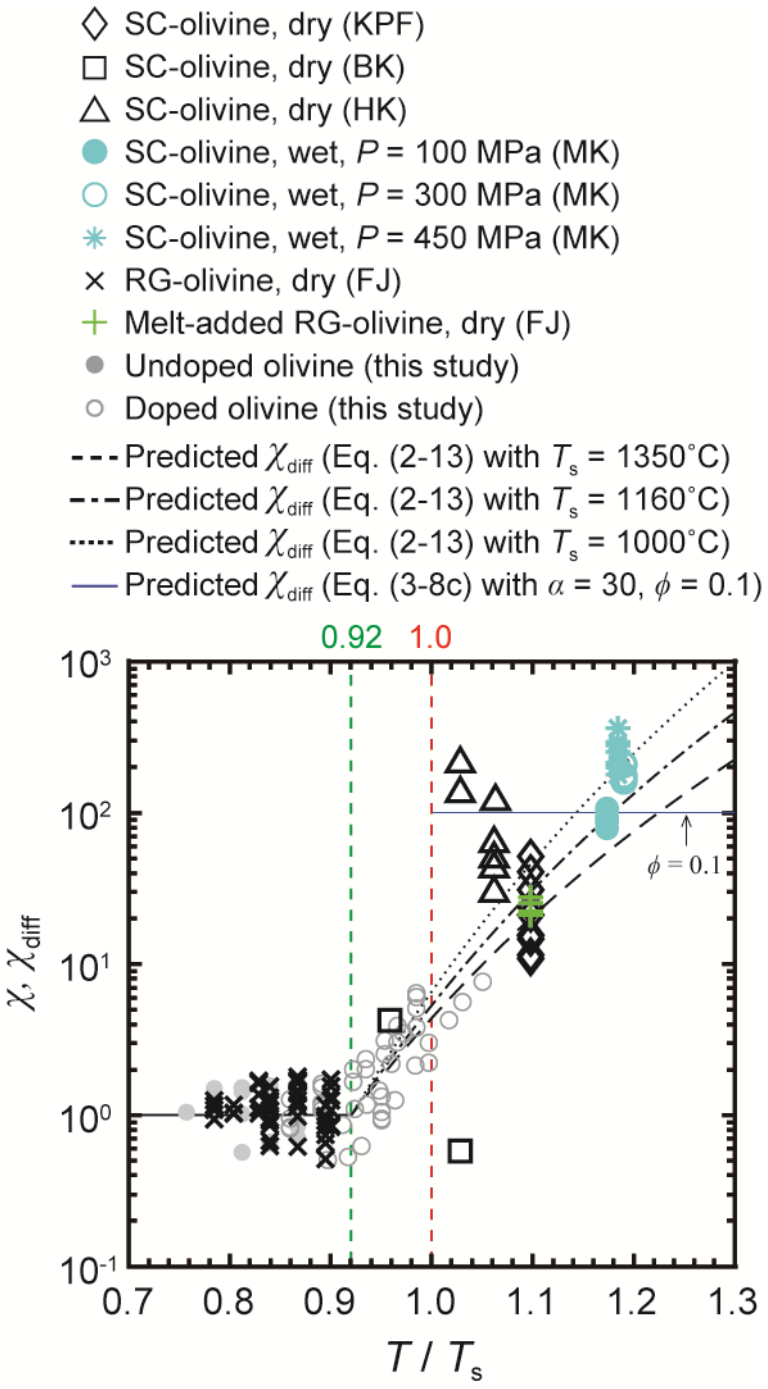

Fig.3-2. Plot of χ as a function of experimental temperature normalized by the sample solidus (T/T_s). Data from our undoped and doped olivine given in *chapter 2* are included. The predicted T/T_s-χ_{diff} relationships (Eq. (2-13)) for T_s of 1000, 1160, and 1350˚C are shown. The predicted χ_{diff} of the creep rate affected by the presence of a ϕ = 0.1 melt fraction above T_s (Eq. (3-8c)) is shown by a blue line.

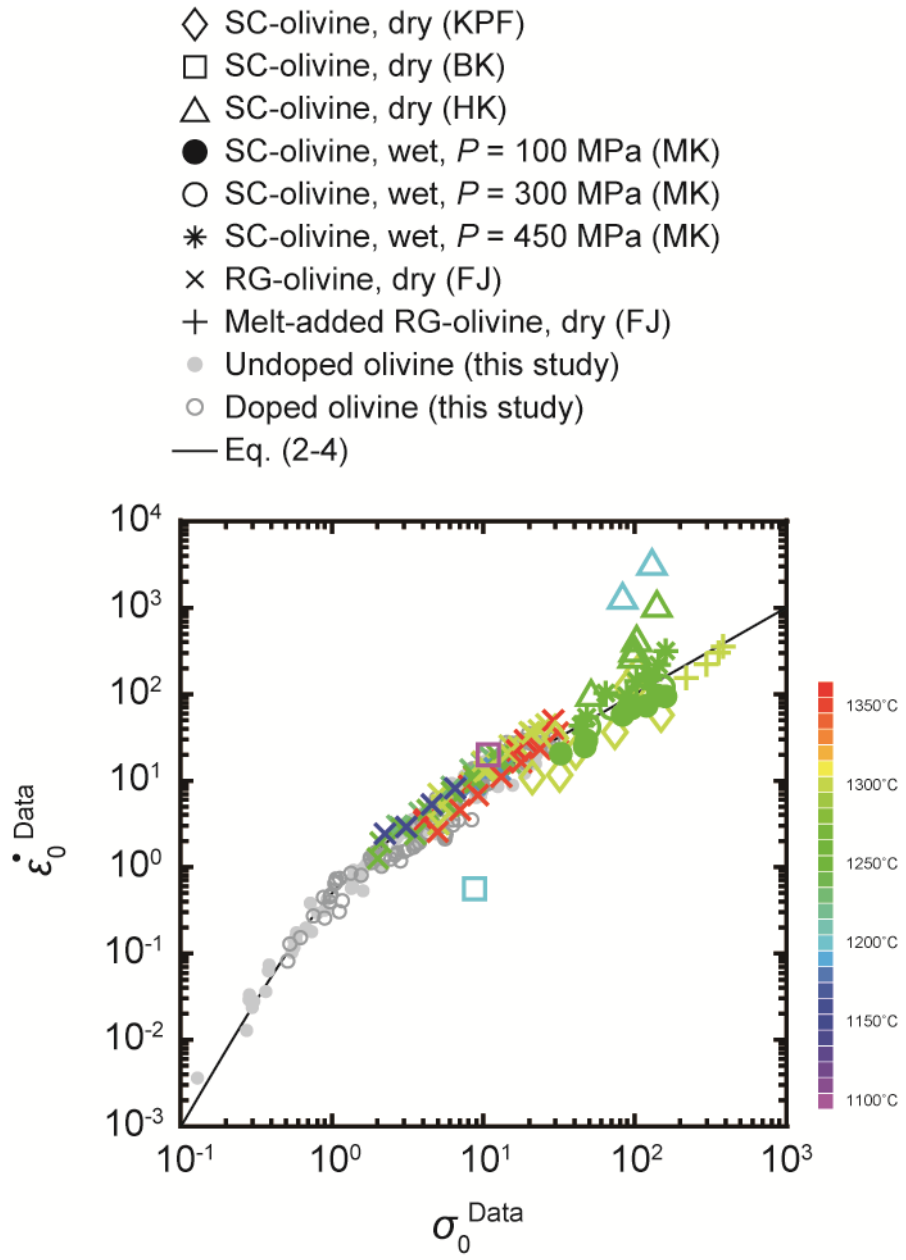

Fig.3-3. Plot of nondimensionalized strain rate ($\dot{\varepsilon}_0^{\mathrm{Data}}$) versus nondimensionalized stress (σ_0^{Data}) for the previously reported (σ, $\dot{\varepsilon}$) values. The ($\sigma_0^{\mathrm{Data}}, \dot{\varepsilon}_0^{\mathrm{Data}}$) were calculated based on Eqs. (1-8), (2-14) and (2-15) (see text for details). The curve calculated from Eq. (2-4) is included.

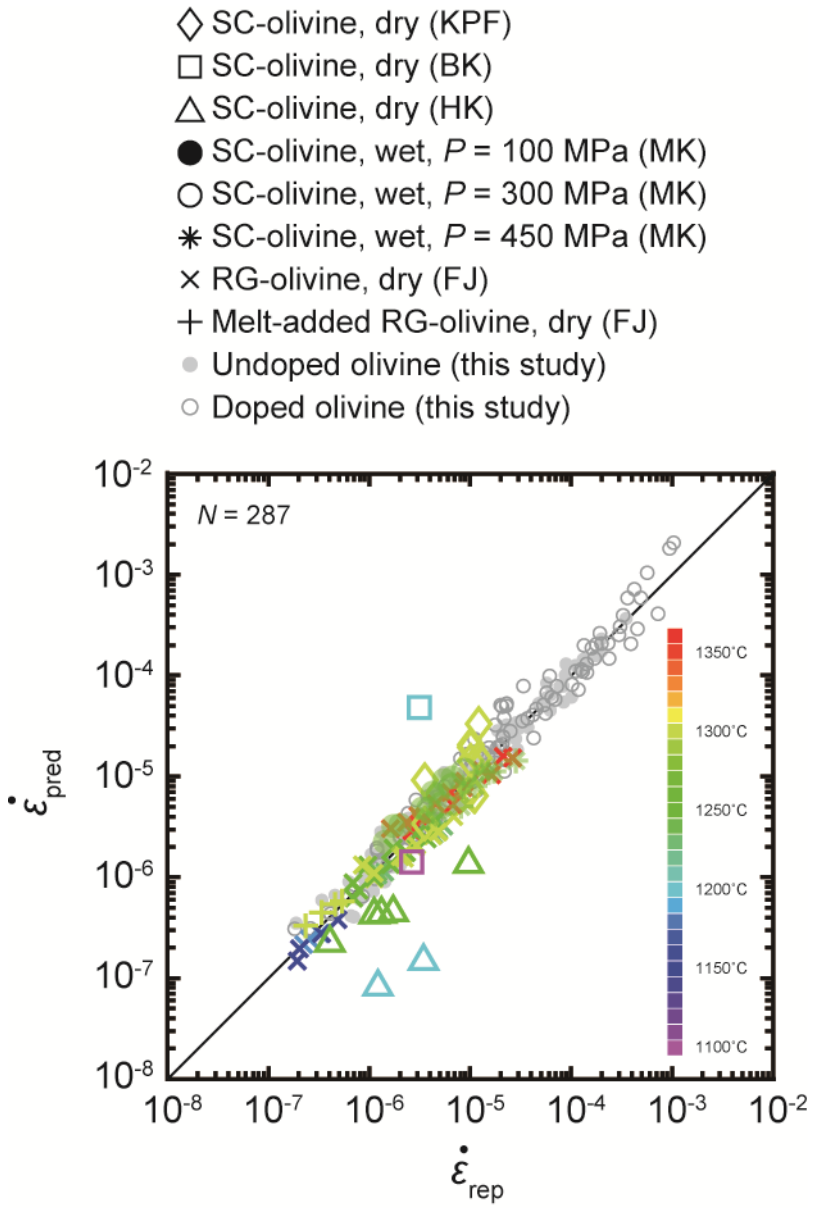

Fig. 3-4. Plot of predicted strain rate ($\dot{\varepsilon}_{\mathrm{pred}}$) (Eqs. (2-6), (2-8), (2-11), (2-12), and (2-13)) versus reported strain rate ($\dot{\varepsilon}_{\mathrm{rep}}$). *N*: number of ($\sigma$, $\dot{\varepsilon}$) data analyzed.

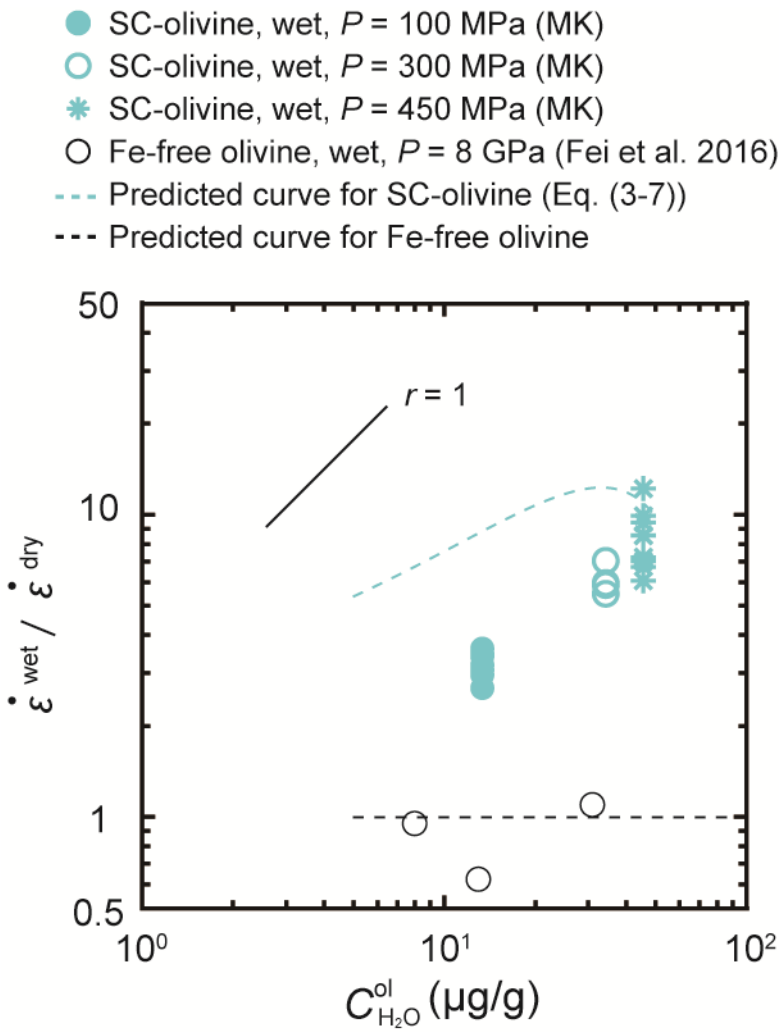

Fig. 3-5. Plot of strain-rate ratios at wet and dry conditions (i.e., $\dot{\varepsilon}^{\mathrm{wet}}/\dot{\varepsilon}^{\mathrm{dry}}$) based on the results of MK and Fei et al. (2016) as a function of the weight fraction of water in olivine ($C_{\mathrm{H_2O}}^{\mathrm{ol}}$). The predicted curve for SC-olivine based on Eq. (3-7) with $T_{\mathrm{s}}^{\mathrm{dry}}$ = 1160˚C and $T_{\mathrm{s}}^{\mathrm{wet}}$ as a function of $C_{\mathrm{H_2O}}^{\mathrm{ol}}$ is included. The predicted $\dot{\varepsilon}^{\mathrm{wet}}/\dot{\varepsilon}^{\mathrm{dry}}$ = 1 relation for Fe-free olivine is also shown as a black broken line.

Chapter 4

4. Application to the oceanic upper mantle

In *chapter 2*, I concluded that grain-boundary diffusion creep rather than interface-controlled creep controls mantle flow based on the T (K)-$\sigma \cdot d$ (MPa · mm) relationship, which was derived for a combined grain-boundary diffusion and interface-controlled creep mechanism (see Fig. 2-20). Thus, I consider the shear viscosity ($\eta = \sigma/(3\dot{\varepsilon})$) of the upper mantle based on Eqs. (2-6), (2-11) with $\chi_{\mathrm{int}} \cdot \dot{\varepsilon}_{\mathrm{int}}^{\mathrm{ref}} = \infty$, and (2-13), in which an activation volume (V) is added and the temperature is replaced with the geotherm (T_{geo}):

$$\eta = \frac{d^3}{3A_{\mathrm{diff}}\chi_{\mathrm{diff}}} \exp\left(-\frac{Q_{\mathrm{diff}}+PV}{\mathrm{R}T_{\mathrm{geo}}}\right), \qquad (4\text{-}1a)$$

where

$$\chi_{\mathrm{diff}} = 1 \qquad \text{at} \quad T_{\mathrm{geo}}/T_{\mathrm{s}} \leq 0.92, \qquad (4\text{-}1b)$$

$$\chi_{\mathrm{diff}} = \exp\left[-\frac{\Delta Q}{\mathrm{R}T_{\mathrm{s}}} \cdot \left(\frac{1}{T_{\mathrm{geo}}/T_{\mathrm{s}}} - \frac{1}{0.92}\right)\right] \qquad \text{at} \quad T_{\mathrm{geo}}/T_{\mathrm{s}} > 0.92. \qquad (4\text{-}1c)$$

I used 4 cm^3/mol for V, which was determined by Si grain-boundary self-diffusion experiments on Fe-free olivine aggregates synthesized in our laboratory at pressures ranging from 0.1 MPa to 13 GPa (Fei et al., 2016). In *chapter 2*, I showed good reproductions of creep rates for Fe-free and Fe-bearing olivine obtained in Nakakoji et al., (2018) and this study, respectively, with their reported diffusivities (Fig. 2-16). As seen in Eq. (4-1), grain size, temperature (T_{geo}) and normalized temperature ($T_{\mathrm{geo}}/T_{\mathrm{s}}$) are the primary factors controlling viscosity. The grain size in the mantle is not easily determined and I simply provide a constant grain size of 1 mm. I discuss the assumption of the grain size in the next section.

I should note the water effect on diffusion creep through the reduction of T_{s} in our model (Eqs. (3-7) and (4-1)), which differs from the effect through increasing water concentration of olivine in the classic olivine creep model (e.g., Hirth & Kohlstedt, 2003).

I assume Eq. (4-1), which was established based on the experimental results of olivine aggregates with pyroxene fractions of 0 to 0.3 (i.e., olivine fractions of 0.7 to 1), to be

applicable to lherzolite mantle with olivine fraction of ~0.6. This could be justified by the applicability of the single diffusion creep law to Fe-free olivine aggregates with pyroxene fraction of up to 0.4 in grain-boundary-diffusion-creep regime (Tasaka et al., 2013; Nakakoji et al., 2018). The little effect of pyroxene on grain-boundary diffusion creep of Fe-bearing olivine was also indicated in this study (see *section 2.4.1.2*)

I choose the upper mantle beneath mid-ocean ridges (MOR) and 50-Ma-old seafloor. First I explore the depth dependence of T_{geo} and T_{s} for the two mantle settings and then use these values to investigate the depth dependence of η using Eq. (4-1). The application of Eq. (4-1) to the mantle implicitly assumes zero contribution of melt to mantle weakening. A small estimated melt fraction (i.e., $\phi \leq 0.04$), even beneath MOR (Hammond & Toomey, 2003; Dunn & Forsyth, 2003; Baba et al., 2006), predicts little reduction in the mantle viscosity (Eq. (3-8c)) (Hirth & Kohlstedt, 1995). Meanwhile, I will consider the role of melt in strengthening the mantle through water extraction from the mineral phases, which is described by increases in T_{s} in my model (Eq. (3-7)).

4.1. Grain size

A few microstructural studies have investigated mantle xenoliths believed to originate from the oceanic mantle lithosphere, which exhibit grain sizes of 1–3 mm (Harigane et al., 2011; Liu et al., 2019). Thanks to a detailed report of microstructures by Liu et al. (2019), I was able to analyze olivine grain sizes (d_{ol}) with respect to the fraction of other (secondary) minerals (f_{II}) and the grain size of orthopyroxene (d_{px}). I choose the coarse-grained xenoliths they referred to as CG sample no. 16FN in that paper, which is distinct in terms of being (apparently) free from recrystallization, which is prominent in other types of xenoliths. I attribute such recrystallization to a process that occurs subsequent to asthenospheric flow. The coarse-grained xenoliths exhibit tabular grain shapes with CPO, which correspond to the microstructural characteristics of olivine aggregates synthesized in our laboratory that developed CPO during diffusion creep (Miyazaki et al., 2013; Maruyama & Hiraga 2017b; Fig. 2-6h). I plot $d_{\mathrm{ol}}/d_{\mathrm{px}}$ against f_{II} in Fig. 4-1 with the data from statically annealed and deformed our Fe-free (Tasaka & Hiraga, 2013) and Fe-bearing (Tables 2-2 and 2-3) samples. The grain sizes in Fe-free aggregates are known to follow a Zener relationship of the form $d_{\mathrm{ol}}/d_{\mathrm{px}} = \beta/{f_{\mathrm{II}}}^{z_e}$, where β (≈ 0.7) is the Zener coefficient and z_e (≈ 0.5) is the Zener parameter (Smith, 1948; Hiraga et al., 2010b; Tasaka & Hiraga, 2013), which has been found to explain the grain sizes in some natural mantle rocks (Linckens et al., 2011; Tasaka et al., 2014; Hansen & Warren 2015; Ambrose et al., 2018). It has been shown that this relationship is maintained during diffusion creep where grain growth occurs due to the driving force of interfacial energy

(Tasaka et al., 2014). The grain size ratios in the natural samples of Liu et al. (2019) overlie the ratios observed in our experimental samples as well as the Zener relationship (Fig. 4-1), indicating that the observed grain sizes are controlled by grain growth under secondary-phase pinning rather than dynamic recrystallization, where the observed grain size is a result of the paleostress experienced by the rocks (e.g., Ave Lallemant et al., 1980).

The mineral mode assumed for the upper mantle material (i.e., peridotite) in *sections 4.2–4.4* corresponds to f_{II} of 0.4–0.5, for which the finest grain sizes of 1.3–1.5 mm were measured (Liu et al., 2019). They reported area-weighted average grain sizes (i.e., $d = \frac{1}{S}\sum_{i=1}^{N} S_i \cdot d_i$ where N is the total number of grains, S is the total area of grains, and S_i and d_i are the area and diameter of i-th grain, respectively), which are known to give larger values than conventional number-average grain sizes (i.e., $d = \frac{1}{N}\sum_{i=1}^{N} d_i$) (used in this study). Using the former method, I obtained d values that are about 1.6 times larger than values given by the latter method from the same microstructures (see Fig. D1 in *appendix*). Although their size ratio is a function of the grain-size distribution, I can reasonably consider a grain size of 1 mm in Eq. (4-1a) based on the oceanic lherzolite described by Liu et al. (2019). Obviously, it is premature to conclude the predominance of a millimeter-scale grain size in the mantle with such limited observations, leaving the issue for future studies.

4.2. Temperature

At dry conditions, $T_{\mathrm{s}}^{\mathrm{dry}}$ is a function of pressure (Eq. (3-2)), which changes with depth (z) in the mantle as $z\ (\mathrm{km}) = 30.2 \times P(\mathrm{GPa}) + 5$. Thus, $T_{\mathrm{s}}^{\mathrm{dry}}$ is related to z by (Fig. 4-2a):

$$T_{\mathrm{s}}^{\mathrm{dry}}(^{\circ}\mathrm{C}) = -5.104 \times \left(\frac{z-5}{30.2}\right)^2 + 132.899 \times \left(\frac{z-5}{30.2}\right) + 1120.661. \quad (4\text{-}2)$$

At wet conditions, $T_{\mathrm{s}}^{\mathrm{wet}}$ is a function of $C_{\mathrm{H_2O}}^{\mathrm{melt}}$ (Eqs. (3-3) and (3-4)), which has been calculated for water concentrations in mantle peridotite ($C_{\mathrm{H_2O}}^{\mathrm{perid}}$) of 50, 100, 200, and 300 μg/g and the partition coefficient of water between peridotite and melt ($KD_{\mathrm{H_2O}}^{\mathrm{perid-melt}}$) (Fig. 4-2a). Here peridotite maintains a constant olivine fraction of ~60 vol%, while other

mineralogical compositions change with depth following Hirschmann et al. (2009). The values of $C_{H_2O}^{perid}$ include estimated concentrations for a MOR basalt source (i.e., 50-200 μg/g) (Saal et al., 2002; Salters & Stracke, 2004) and the source for oceanic island basalt (i.e., 300-900 μg/g) (Dixon et al., 1997; Jamtveit et al., 2001; Nichols et al., 2002; Simons et al., 2002). I used previously calculated z-dependent $KD_{H_2O}^{perid-melt}$ values (O'Leary et al., 2010; Dasgupta et al., 2013; see Fig. 4-2b). Due to the lack of reported $KD_{H_2O}^{perid-melt}$ values at low-P (i.e., <1 GPa) conditions, I cannot obtain reliable T_s^{wet} values, and hence, η is also unreliable at z<35 km under wet conditions.

A mantle potential temperature and adiabatic temperature gradient of 1350˚C and 0.4˚C/km, respectively, were used to calculate T_{geo} beneath MOR. I consider this T_{geo} to be applicable to depths of >10 km (Sleep, 1975). The adiabatic temperature profile intersects T_s^{dry} at z = 68 km, resulting in the onset of anhydrous melting of the upwelling mantle (Fig. 4-2a). The degree of mantle melting rapidly increases, causing a decrease in temperature due to extraction of the latent heat of fusion from the internal energy. This is expected to produce a large temperature gradient, so I use 2˚C/km for T_{geo} at $z \leq$68 km (Fig. 7 of McKenzie and Bickle, 1988). For the case of wet conditions, the adiabatic temperature profile intersects T_s^{wet} at $z >$68 km depending on $C_{H_2O}^{perid}$, which corresponds to the depth where hydrous melting starts. For hydrous melting, I simply use the adiabatic temperature gradient for T_{geo}, which is reasonable due to the limited degree of melting (Hirschmann, 2010) (Fig. 4-2a).

The T_{geo} of 50-Ma-old mantle was calculated based on a half-space cooling model (Turcotte & Schubert, 2014):

$$\frac{T_1 - T_{geo}}{T_1 - T_0} = \mathrm{erfc}\left(\frac{z}{2\sqrt{\kappa t}}\right), \quad (4\text{-}3)$$

where T_0 and T_1 are the temperatures at z = 0 and z>0 at t = 0, respectively, κ is thermal diffusivity (= 1 mm^2/s), and t is time (= 50 Ma). T_0 is set to 0˚C. I change T_1 in Eq. (4-3) so that T_{geo} converges to the adiabatic temperature profile at a certain z, which results in T_{geo} following Eq. (4-3) with T_1 = 1420˚C at $z \leq$157 km and the adiabatic temperature profile at z>157 km (Fig. 4-2a).

The calculated T_{geo}/T_s values beneath MOR and 50-Ma-mantle for $C_{H_2O}^{perid}$ of 0, 50, 100, 200, and 300 μg/g are shown in Figs. 4-3a and b. Beneath MOR, T_{geo}/T_s increases with decreasing depth mainly due to the decrease in T_s (Eq. (4-2)) (Fig. 4-3a). Here I incorporate the removal of water through melt migration. If I consider melt to be the most efficient medium for extraction of the water, that is, dehydration through fractional melting of peridotite, the water remains extracted until T_s^{wet}, which is determined by $C_{H_2O}^{perid}$, reaches T_{geo}. In this case, T_{geo}/T_s stays constant at unity with decreasing z from the depth at which hydrous melting starts down to z = 68 km, where anhydrous melting starts, which corresponds to the dotted curve in Fig. 4-3a. At z<68 km, T_{geo}/T_s follows T_{geo}/T_s of $C_{H_2O}^{perid}$ = 0.

In 50-Ma-old mantle, T_{geo}/T_s peaks at a depth of 100–150 km, depending on $C_{H_2O}^{perid}$ (Fig. 4-3b). At z>150 km, T_{geo}/T_s essentially follows the same profile as beneath MOR. At z<100 km, T_{geo}/T_s decreases sharply with decreasing z, essentially following the large T_{geo} gradient in the region. If I consider water extraction to occur beneath MOR with no subsequent change in $C_{H_2O}^{perid}$, the T_s-depth profile in 50-Ma-old mantle corresponds to the profile formed beneath MOR. We used this T_s to determine T_{geo}/T_s in 50-Ma-old mantle, which is shown by the dotted curve in Fig. 4-3b.

4.3. Enhancement of grain-boundary diffusion creep

Having established how T_{geo}/T_s and T_s change with z and $C_{H_2O}^{perid}$ beneath MOR and 50-Ma-old seafloor, I can calculate depth profiles of χ_{diff} based on Eqs. (4-1b and c). As predicted from the T_{geo}/T_s profile beneath MOR (Fig. 4-3a), χ_{diff} is >1 at $z \leq$250 km for the highest value of $C_{H_2O}^{perid}$ (Fig. 4-3c). The lowermost depth of the χ_{diff}>1 regime decreases with decreasing $C_{H_2O}^{perid}$. At $C_{H_2O}^{perid}$ = 0, the χ_{diff}>1 regime is limited to $z \leq$115 km. Within the χ_{diff}>1 regime, χ_{diff} increases with decreasing z. The value of χ_{diff} during dehydration due to fractional melting follows the dotted curve in Fig. 4-3c. Such efficient dehydration forces χ_{diff} to maintain a fixed value of ~4 due to T_{geo}/T_s = 1 during hydrous melting.

Beneath 50-Ma-seafloor, the χ_{diff}>1 regime for the highest $C_{\mathrm{H_2O}}^{\mathrm{perid}}$ corresponds to 80≤z≤250 km (Fig. 4-3d). The smaller the $C_{\mathrm{H_2O}}^{\mathrm{perid}}$, the narrower the z range resulting in the absence of a χ_{diff}>1 regime for $C_{\mathrm{H_2O}}^{\mathrm{perid}}$ = 0. As $C_{\mathrm{H_2O}}^{\mathrm{perid}}$ decreases from 300 to 100 μg/g, the upper limit of the χ_{diff}>1 regime changes from 80 to 100 km in depth, while its lower limit significantly changes from 250 km to 150 km. The largest χ_{diff} value of ~4 is estimated to occur at a depth of ~130 km in the case of the highest $C_{\mathrm{H_2O}}^{\mathrm{perid}}$. χ_{diff} peaks at essentially the same depths for different $C_{\mathrm{H_2O}}^{\mathrm{perid}}$. The trend of χ_{diff} affected by efficient dehydration follows the dotted curve in Fig. 4-3d. Only at a $C_{\mathrm{H_2O}}^{\mathrm{perid}}$ of 300 μg/g is χ_{diff} affected by dehydration, but the effect is very minor.

4.4. Viscosity–depth profiles

Now all parameters needed to estimate the mantle viscosity based on Eq. (4-1) are available. Beneath MOR, a depth-independent viscosity of 5×10^{19} Pa·s is predicted for any $C_{\mathrm{H_2O}}^{\mathrm{perid}}$ in the deeper portion of the mantle, while the mantle becomes weaker with decreasing z in the shallower portion. The depth at which weakening starts becomes shallower with decreasing $C_{\mathrm{H_2O}}^{\mathrm{perid}}$. The largest estimated $C_{\mathrm{H_2O}}^{\mathrm{perid}}$ for the MOR basalt source (= 200 μg/g) gives the lowest η of ~4×10^{18} Pa·s in the shallowest region in the mantle. For the case of efficient dehydration and $C_{\mathrm{H_2O}}^{\mathrm{perid}}$ = 0, a depth-insensitive regime with η of ~1×10^{19} Pa·s appears in the shallow portion of the mantle.

Beneath 50-Ma-old seafloor, a depth-independent viscosity of 5×10^{19} Pa·s is predicted for any $C_{\mathrm{H_2O}}^{\mathrm{perid}}$ in the deeper portion of the mantle, while the mantle weakens with decreasing z in the middle portion of the mantle, depending on $C_{\mathrm{H_2O}}^{\mathrm{perid}}$. In the shallow portion, viscosity significantly increases with decreasing z for any $C_{\mathrm{H_2O}}^{\mathrm{perid}}$. The

middle weak zone at depths of 100–250 km forms only at $C_{H_2O}^{perid}$>100 μg/g. Its thickness increases with increasing $C_{H_2O}^{perid}$, resulting in a ~100-km-thick zone with a viscosity reaching a minimum of 2×10^{19} Pa·s at a $C_{H_2O}^{perid}$ of 200 μg/g. Efficient dehydration does not essentially change the viscosity at any $C_{H_2O}^{perid}$, as shown by the dotted curve.

4.5. Characteristics of mantle deforming by the grain-boundary diffusion creep mechanism

Here I discuss various characteristics of the (upper) mantle when it is deforming mainly by the mechanism of grain-boundary diffusion creep. Overall, the weak zones in the mantle correspond to the regime where χ_{diff}>1, i.e., the regime of T_{geo}/T_s>0.92. During mantle cooling, the χ_{diff}>1 zone gradually disappears from the top surface resulting in the development of lithosphere with a low-viscosity region below. The base of the low-viscosity region remains at the same depth over time due to the time-independent T_{geo} at that depth. The low-viscosity region clearly corresponds to the mantle asthenosphere.

I show the viscosity profile of χ_{diff} fixed at unity (Eq. (4-1a)) at all depths in Fig. 4-3e. This situation corresponds to a mantle viscosity essentially controlled by T_{geo} instead of T_{geo}/T_s. As seen in the profile, such pure thermal (T_{geo}) control of viscosity results in the formation of a stiff top layer of mantle even beneath MOR. Similar stiff top mantle layers beneath MOR have been predicted to form based on the classic water effects on both diffusion creep and dislocation creep (see discussion in *section 3.3.2*) (Karato, 1986; Hirth & Kohlstedt, 1996; Karato & Jung, 1998). These studies estimated that significant hardening occurs during the transformation of wet mantle into dry mantle from a depth of ~70 km by anhydrous melting, resulting in the formation of lithosphere with thicknesses of several tens of km beneath MOR. My viscosity model is also affected by anhydrous melting at a depth of ~70 km; however, the low-viscosity mantle is still present with decreasing depth (Fig. 4-3e), which results in very thin (< 10 km) lithosphere beneath MOR.

The effect of water on viscosity as a manifestation of the reduction of T_s in my model predicts water-induced mantle weakening to be associated with high T_{geo} (or high T_{geo}/T_s). The $C_{H_2O}^{perid}$-independent viscosity, i.e., the viscosity that is free from water effects in both the shallow and deeper portions of the mantle (Figs. 4-3e and f), is

essentially due to this temperature requirement for weakening.

Grain-boundary diffusion creep is highly grain-size sensitive; thus, the proposed viscosity profiles (Figs. 4-3e and f) change significantly for different grain sizes. 1 mm grain size imposed in this study stands from the limited observations and we remain the possibility of different grain sizes especially for their larger values. Since the viscosity is proportional to d^3 (Eq. (4-1)), the presented viscosity profiles shift to almost an order of magnitude larger viscosity for grain size of 2 mm. Assuming 10^{19}~10^{20} Pa·s as the viscosity of asthenosphere, the size corresponds to almost maximum value that permits grain-boundary diffusion creep to control the mantle viscosity.

As briefly explained in the *Introduction*, the temperature condition of T/T_s>0.92 for χ_{diff}>1 was firstly identified as a condition for CPO development during diffusion creep of Fe-free olivine, which corresponds to the condition for the appearance of crystallographic low-index-plane grain boundaries (Miyazaki et al., 2013). While the temperature condition for CPO during diffusion creep of Fe-bearing olivine was not explored in this study, the observed tabular grain shapes and CPO support their appearance at the same T/T_s>0.92 (Fig. 2-6f and h). Although there is no clear physical explanation yet, I consider grain-boundary disordering to promote the development of such boundaries. Since GBS is easier at low-index grain boundaries, CPO can form at any conditions once the boundaries are formed (Maruyama & Hiraga, 2017b). Miyazaki et al. (2013) previously demonstrated CPO development at T/T_s<0.92 after the sample had been annealed at T/T_s>0.92, where low-index grain boundaries formed. Once the rocks have experienced the highest temperature (or highest T_{geo}/T_s), the grain size (grain growth) is essentially saturated (Nakakoji et al., 2018) so that changes from low-index grain boundaries to general boundaries is predicted to be limited, especially during diffusion creep. Thus, it is likely that the grain-boundary structure reflects the highest T_{geo}/T_s experienced, which corresponds to the T_{geo}/T_s beneath MOR. As a result, either a significant CPO or a random CPO, in other words, elastically (seismically) anisotropic or isotropic mantle is expected to form depending on the depths of T_{geo}/T_s>0.92 and T_{geo}/T_s<0.92 beneath MOR, respectively. The T_{geo}/T_s depth profile beneath MOR predicts T_{geo}/T_s = 0.92 at a depth of 190 km at $C_{H_2O}^{perid}$ of 200 μg/g. The mantle deforming by diffusion creep seems to explain the observation of a sharp change from anisotropic to isotropic oceanic mantle with depth at a depth of ~200 km (Nettles & Dziewonski, 2008).

Yamauchi and Takei (2016) and Takei (2017) explained the low-velocity zone and/or

high-attenuation zone in the oceanic mantle by grain-boundary pre-melting (Eq. (3-8)). In comparing their proposed enhancement of grain-boundary diffusion by pre-melting with my diffusion creep law ((Eq. (2-13)), I see that their pre-melting is essentially identical to the situation of χ_{diff}>1 in my model. Thus, it is reasonable to correlate that seismically distinct zone in the oceanic mantle with the χ_{diff}>1 region (Figs. 4-3c and d); i.e., the low-viscosity mantle asthenosphere.

4.6. Involvement of other creep mechanisms

An alternative mechanism to grain-boundary diffusion is lattice (volume) diffusion, which can control creep at the grain size present in the mantle. As grain size increases, the relative contribution of lattice diffusion to total diffusional processes increases, resulting in a transition from grain-boundary diffusion to lattice diffusion creep. The transition from grain-boundary to lattice diffusion should occur at a grain size (often referred to as the critical grain size: d_{cr}) determined by $d_{\mathrm{cr}} \approx 3\delta D_{\mathrm{GB}}/D_{\mathrm{latt}}$ (D_{latt}: lattice diffusivity) (Stocker & Ashby, 1973). The switch from a grain-boundary-controlled to a lattice-controlled diffusion process occurs at a grain size of ~1 mm, depending on the self-diffusion data used (Dohmen et al., 2002; Fei et al., 2012; Nakakoji & Hiraga, 2018). If I assume lattice diffusion creep as the dominant mechanism in the mantle, the unique viscosity profile due to grain-boundary disordering, i.e., the $T_{\mathrm{geo}}/T_{\mathrm{s}}$-dependent rheology in the χ_{diff}>1 region, will not appear. Meanwhile, the strain rate due to the lattice diffusion creep mechanism couples in parallel with the rate of grain-boundary diffusion creep so that the lattice-diffusion-creep-controlled viscosity should appear at a viscosity lower than that predicted from grain-boundary diffusion creep.

The significance of GBS during diffusion creep should not vary with a change from grain-boundary diffusion creep to lattice diffusion creep, since both diffusional processes are considered to accommodate GBS during diffusion creep (Raj & Ashby, 1971; Ashby & Verrall, 1973; Wang, 2000). It has been pointed out that there is no experimental evidence that one has to assume the presence of both diffusion creep and diffusion-controlled GBS creep mechanisms (Rust & Todd, 2011; Maruyama & Hiraga, 2017a); thus, lattice diffusion creep can also be referred to as lattice-diffusion-controlled (accommodated) GBS creep. Lattice diffusion creep accompanied by the development of low-index-plane grain boundaries at $T_{\mathrm{geo}}/T_{\mathrm{s}}$>0.92 will result in the same CPO as during grain-boundary diffusion creep.

Similarly to lattice diffusion creep, dislocation motion is a parallel process with diffusion creep (Nakakoji et al., 2018). Thus, dislocation-based viscosity should appear in a similar manner to lattice-diffusion-creep-controlled viscosity overlaying the grain-

boundary-diffusion-creep-controlled viscosity. However, a quantitative prediction is not straightforward, because the stress as well as the grain size determines the dominant deformation mechanism. Geophysical modelling studies incorporating olivine flow laws have shown that the grain size of ≥1 cm is favored for the mantle viscosity controlled by dislocation creep (Behn et al., 2009; Turner et al., 2015). Lattice and grain-boundary diffusion creep laws predict the mantle to be 10^2 to 10^3 times stronger at a cm grain-size than the mantle properties calculated in this study (Figs. 4-3e and f), which rules out the possible role of diffusion creep at such grain sizes.

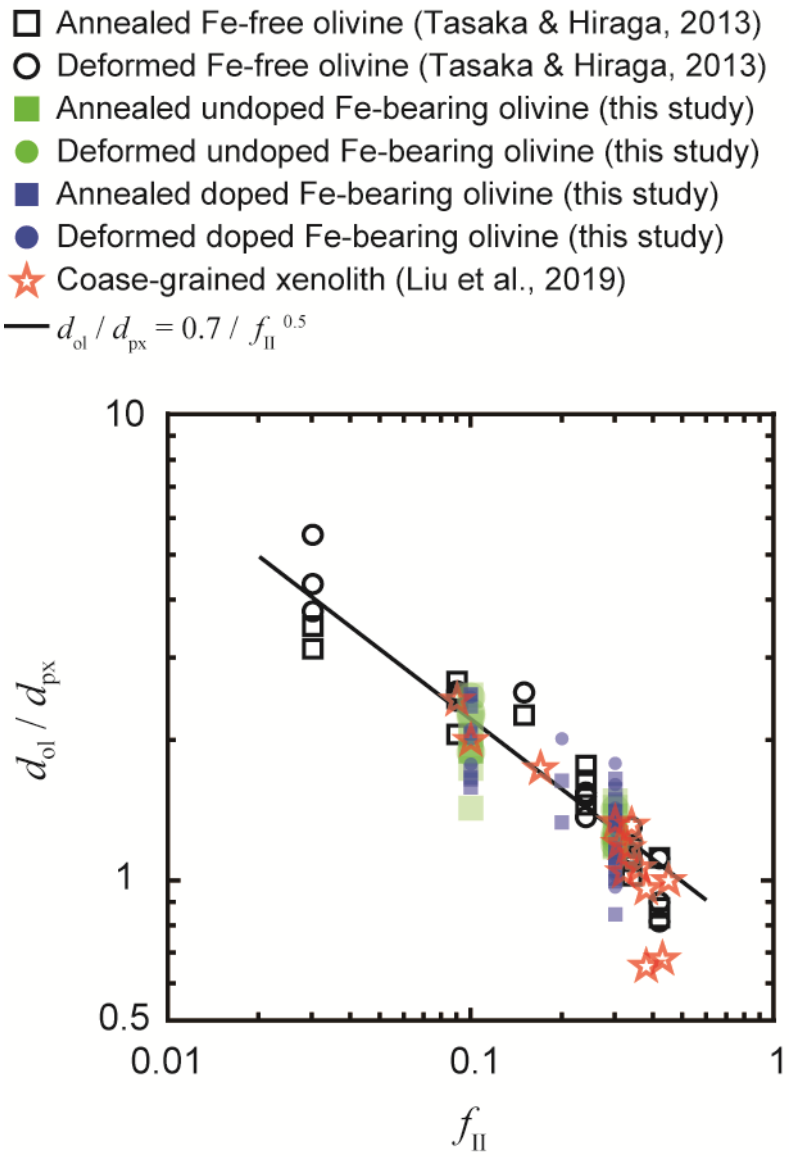

Fig. 4-1. Plots of olivine grain size (d_{ol}) normalized by that of pyroxene (d_{px}) as a function of the fraction of secondary minerals (f_{II}). The analyzed samples correspond to synthetic Fe-free olivine + pyroxene aggregates described in Tasaka and Hiraga (2013), synthetic Fe-bearing olivine + pyroxene aggregates reported in Tables 2-2, and 2-3, and mantle xenoliths from Fernando de Noronha reported by Liu et al. (2019). The synthetic samples were statically annealed and deformed at high temperatures. The Zener relationship identified in olivine + pyroxene aggregates synthesized in the same way as this study (Hiraga et al., 2010b; Tasaka and Hiraga, 2013) is included in the figure.

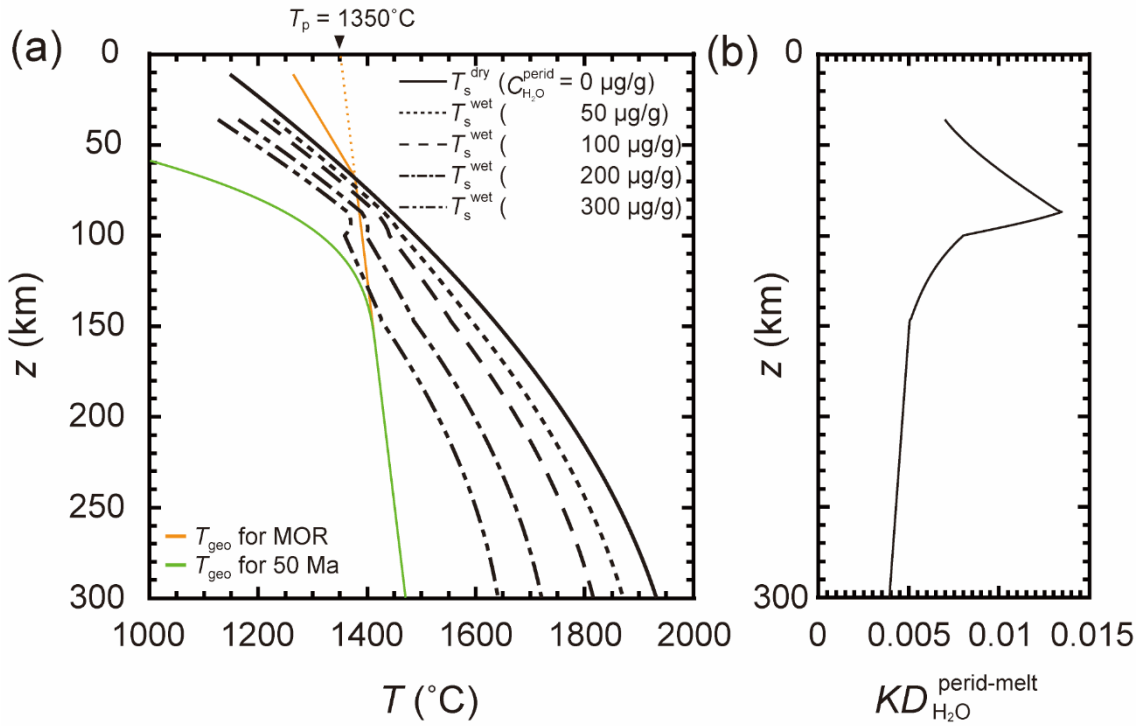

Fig. 4-2. Depth profiles of geological parameters required to apply the grain-boundary diffusion-creep-based viscosity law of Eq. (4-1a). (a) Geotherms and estimated solidi for the mantle with $C_{H_2O}^{perid}$ of 0, 50, 100, 200, and 300 μg/g beneath MOR and 50-million-year-old seafloor. (b) Partition coefficients of water between peridotite and melt ($KD_{H_2O}^{perid-melt}$) (O'Leary et al., 2010; Dasgupta et al., 2013), which was estimated for peridotite with an olivine fraction of ~60 vol% (Fig. 6 in Hirschmann et al. (2009)).

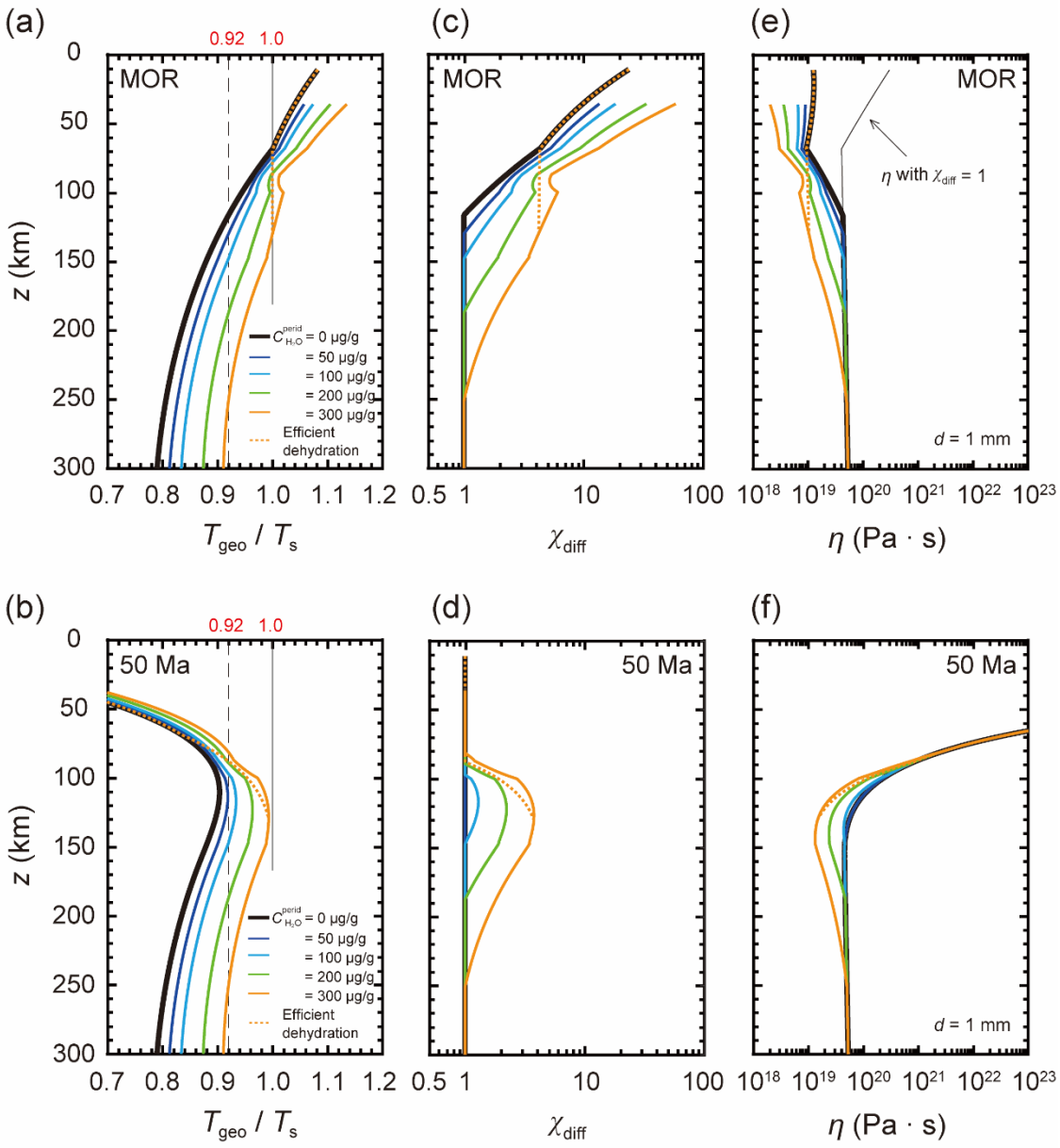

Fig. 4-3. Depth profiles of the primary factors controlling olivine grain-boundary diffusion creep and its consequence for upper mantle viscosity beneath mid-ocean ridges (MOR) and 50-million-year-old seafloor. Grain size is given as 1 mm. (a–b): Estimated geotherms (T_{geo}) normalized by the mantle solidus (T_s) beneath (a) MOR and (b) 50-million-year-old seafloor. We use T_{geo} given in Fig. 4-2a and T_s calculated for water concentrations in mantle peridotite ($C_{H_2O}^{perid}$) of 0, 50, 100, 200, and 300 µg/g (Eqs. (3-3), (3-4), and (4-2)). The dotted curves show T_{geo}/T_s during efficient dehydration by

melting. (c–d): Estimated χ_{diff} (Eqs. 4-1b and c) for different $C_{\mathrm{H_2O}}^{\mathrm{perid}}$ beneath (c) MOR and (d) 50-million-year-old seafloor. The dotted curves show χ_{diff} during efficient dehydration. (e–f): Predicted viscosity (η) beneath (e) MOR and (f) 50-million-year-old seafloor (Eq. (4-1a)). The dotted curves show η during efficient dehydration. η for a fixed χ_{diff} value of 1 is shown in (e).

Chapter 5

Conclusions

The plots in Fig. 2-13 indicate that my deformation experiments were conducted in a range sufficient to characterize power-law interface-controlled creep of olivine and grain-boundary diffusion creep of undoped olivine. As a result, I established precise flow laws for both deformation processes. I used the combined flow law as a reference to detect the effect of doping on olivine creep. I created a nondimensional stress and strain-rate space that allowed us to compare essentially intact experimental data from doped samples with the reference data. This method differs from using flow law parameters to calibrate mechanical data obtained from various grain sizes, temperatures, stress, etc. under certain conditions. The new method is a more powerful tool for comparing mechanical data from various research groups.

I showed that doping olivine aggregates with Ca and Al enhances creep rates above certain temperatures, and that the magnitude of this effect increases with temperature. I interpreted the effect in terms of enhancement of both reaction and mass transport at olivine grain boundaries due to grain-boundary disordering promoted by grain-boundary segregation of Ca and Al. I was able to relate the sample solidus to the temperature at which grain-boundary disordering begins to have an effect on the creep rate. This last finding may lead to speculation on the effect of incipient melting on creep. Although this is not supported by phase diagrams, microstructural observations, or theoretical modeling of creep, it is difficult to completely eliminate that possibility. I found enhancement of interface-controlled creep rates even at >200˚C below the solidus temperatures that I determined based on microstructures. Taking into account the detection of 0.1 vol% melt in the aggregates, such low temperatures undoubtedly exclude the role of incipient melting, at least for enhancement of interface-controlled creep. Additionally, I found that the enhancement characteristics of interface-controlled creep and diffusion creep could be explained by the same changes in grain-boundary disordering with temperature.

I compared previously reported diffusion creep rates of naturally derived and synthetic, reagent-derived olivine aggregates in the nondimensional space that was constructed based on the olivine grain-boundary diffusion creep law established in this study. The comparisons confirmed that all of the previous experimental results had measured diffusion creep of olivine. Further, it detected lower strength in naturally derived olivine aggregates by up to two orders of magnitude than reagent-derived olivine aggregates at the same temperatures, stress, and grain sizes.

Comparisons of the creep data based on the experimental temperatures normalized by sample solidi (bulk eutectic temperatures) revealed that all the experiments using naturally-derived olivine were conducted at conditions where diffusion creep operates with enhancement of grain-boundary diffusion due to grain-boundary disordering at >0.92×solidus. An olivine grain-boundary diffusion creep law that incorporates the grain-boundary disordering effect at >0.92×solidus explains the majority of the reported creep rates, including those from wet conditions.

Values of the geotherm normalized by the mantle solidus temperature were calculated for the oceanic upper mantle with water contents ranging from 0 to 300 μg/g. I identified conditions for the grain-boundary disordering effect on diffusion creep at depth ranges of 10–250 km and 100–250 km, depending on the water contents, beneath mid-ocean ridges and 50-Ma-old seafloor, respectively.

Grain-boundary diffusion-creep-based mantle viscosity indicates a very thin (<10 km) mantle lithosphere beneath mid-ocean ridges with development of the lithosphere away from the ridge, leaving a low-viscosity region (asthenosphere) below. Depending on the water content, a viscosity of $2–5\times10^{19}$ Pa·s is predicted for the low-viscosity zone beneath 50-Ma-old seafloor at a grain size of 1 mm.

Due to the large grain-size-dependence of diffusion creep mechanisms, diffusion creep will not contribute to the flow of low-viscosity mantle when the olivine grain size is on the order of a centimeter. However, a millimeter-scale grain size that favors diffusion creep in the mantle would exhibit similar mechanical characteristics to the oceanic mantle, as well as similar microstructures to some mantle xenoliths derived from the oceanic lithosphere.

Appendix

A List of symbols, definitions, and units.

Notation	Properties	Unit
ε	Strain	-
$\dot{\varepsilon}$	Strain rate	s^{-1}
$\dot{\varepsilon}_{\mathrm{int}}, \dot{\varepsilon}_{\mathrm{diff}}$	Strain rates of interface-controlled creep and diffusion creep, respectively	s^{-1}
$\dot{\varepsilon}_{\mathrm{int}}^{\mathrm{ref}}, \dot{\varepsilon}_{\mathrm{diff}}^{\mathrm{ref}}$	Strain rates of interface-controlled creep and diffusion creep of reference (=undoped) olivine, respectively	s^{-1}
$\dot{\varepsilon}_{\mathrm{rep}}, \dot{\varepsilon}_{\mathrm{pred}}$	Reported strain rates, and calculated strain rates based on our flow law, respectively	s^{-1}
σ	Stress	MPa
d	Grain size	µm
$d_{\mathrm{ini}}, d_{\mathrm{fin}}, d_{\mathrm{s}}$	Initial grain size, final grain size in deformed sample, and grain size in statically annealed (reference) sample	µm
d_{ε}	Estimated grain size during deformation	µm
$d_{\mathrm{ol}}, d_{\mathrm{px}}$	Grain sizes of olivine and pyroxene, respectively	µm
T	Temperature	K
T_{s}	Sample solidus (bulk eutectic temperature)	K
$T_{\mathrm{s}}^{\mathrm{dry}}, T_{\mathrm{s}}^{\mathrm{wet}}$	Sample solidus (bulk eutectic temperature) under dry and wet condition, respectively	K
T_{enh}	Temperature at which enhancement of grain-boundary processes begins	K
T_{geo}	Geotherm of the oceanic upper mantle	K
A	Preexponential factor of flow law	$s^{-1} \cdot \mu m^{p} \cdot MPa^{-n}$
$A_{\mathrm{int}}, A_{\mathrm{diff}}$	Preexponential factors of flow laws for interface-controlled creep and diffusion creep, respectively	$s^{-1} \cdot \mu m^{p} \cdot MPa^{-n}$
n	Stress exponent	none
n_{app}	Apparent stress exponent	none
n_{int}	Stress exponent of interface creep	none
p	Grain size exponent	none
p_{app}	Apparent grain size exponent	none
p_{diff}	Grain size exponent of diffusion creep	none
P	(Confining or lothostatic) pressure	Pa
Q	Activation energy	$kJ \cdot mol^{-1}$
Q_{app}	Apparent activation energy	$kJ \cdot mol^{-1}$
$Q_{\mathrm{int}}, Q_{\mathrm{diff}}$	Activation energies of interface creep and diffusion creep, respectively	$kJ \cdot mol^{-1}$
R	Gas constant	$J \cdot mol^{-1} \cdot K^{-1}$
$\sigma^{*}, \dot{\varepsilon}^{*}$	Stress and strain rate which satisfy $\dot{\varepsilon}_{\mathrm{int}} = \dot{\varepsilon}_{\mathrm{diff}}$, repectively	MPa and s^{-1}
$\sigma^{*\mathrm{ref}}, \dot{\varepsilon}^{*\mathrm{ref}}$	Stress and strain rate which satisfy $\dot{\varepsilon}_{\mathrm{int}}^{\mathrm{ref}} = \dot{\varepsilon}_{\mathrm{diff}}^{\mathrm{ref}}$, repectively	MPa and s^{-1}
$\sigma_0, \dot{\varepsilon}_0$	Nondimensional stress and strain rate, respectively	none
$\sigma_0^{\mathrm{doped}}, \dot{\varepsilon}_0^{\mathrm{doped}}$	σ_0 and $\dot{\varepsilon}_0$ for doped samples, respectively	none
$\sigma_{0\_\mathrm{ref}}^{\mathrm{doped}}, \dot{\varepsilon}_{0\_\mathrm{ref}}^{\mathrm{doped}}$	$\sigma_0^{\mathrm{doped}}$ and $\dot{\varepsilon}_0^{\mathrm{doped}}$ based on $\sigma^{*\mathrm{ref}}$ and $\dot{\varepsilon}^{*\mathrm{ref}}$, respectively	none
$\sigma_0^{\mathrm{Data}}, \dot{\varepsilon}_0^{\mathrm{Data}}$	$\boldsymbol{\sigma_0}$ and $\boldsymbol{\dot{\varepsilon}_0}$ for previous studies, respectively	none
$\sigma_{0\_\mathrm{ref}}^{\mathrm{Data}}, \dot{\varepsilon}_{0\_\mathrm{ref}}^{\mathrm{Data}}$	σ_0^{Data} and $\dot{\varepsilon}_0^{\mathrm{Data}}$ based on $\sigma^{*\mathrm{ref}}$ and $\dot{\varepsilon}^{*\mathrm{ref}}$, respectively	none
χ	Enhancement of creep rates due to doping	none
$\chi_{\mathrm{int}}, \chi_{\mathrm{diff}}$	χ for interface-controlled and diffusion creep, respectively	none
ΔQ	Estimated activation energy of χ_{int} and χ_{diff} (= 230)	$kJ \cdot mol^{-1}$

A List of symbols, definitions, and units (continued).

Notation	Properties	Unit
f_{px}	Fraction of pyroxene	none
f_{II}	Fraction of secondary phases (other than olivine)	none
α	Dynamic grain growth exponent	none
k	Grain growth coefficient under static conditions	$\mu m^{m} \cdot s^{-1}$
m	Grain growth exponent (assumed to be 4)	none
M	Number of grams in one mole of silicate (= 59)	$g \cdot mol^{-1}$
$\Delta S_{\mathrm{perid}}^{\mathrm{fusion}}$	Entropy of fusion of (mantle) peridotite per unit mass (= 0.4)	$J \cdot K^{-1} \cdot g^{-1}$
$X_{\mathrm{OH^-}}^{\mathrm{melt}}$	Mole fraction of dissolved H_2O in melt	none
$C_{\mathrm{H_2O}}^{\mathrm{ol}}$	Weight fraction of water in olivine	µg/g
$C_{\mathrm{H_2O}}^{\mathrm{perid}}$	Weight fraction of water in mantle peridotite	µg/g
$C_{\mathrm{H_2O}}^{\mathrm{melt}}$	Weight fraction of water in melt	µg/g
$KD_{\mathrm{H_2O}}^{\mathrm{ol-melt}}$	Partition coefficient of water between olivine and melt	none
$KD_{\mathrm{H_2O}}^{\mathrm{perid-melt}}$	Partition coefficient of water between mantle peridotite and melt	none

B FT-IR analyses

I used a system composed of a JASCO FT/IR-660 Plus spectrometer and a JASCO IRT-30 microscope, installed at the Earthquake Research Institute, the University of Tokyo. The entire beam path was evacuated to less than a few tens of Pascal using a rotary vacuum pump, which minimized the noise absorption from atmospheric CO_2 and H_2O (Yasuda, 2014). The spectra were collected between wavenumbers 400 to 7800 cm^{-1} (resolution of 4 cm^{-1}) at room temperature. We analyzed 0.30-mm-thick samples using an aperture of 100 × 100 μm; thus, the number of grains generating the observed absorption is on the order of 10^6 in each sample. As shown in Fig. B1, absorption peaks indicating the presence of "water" are absent.

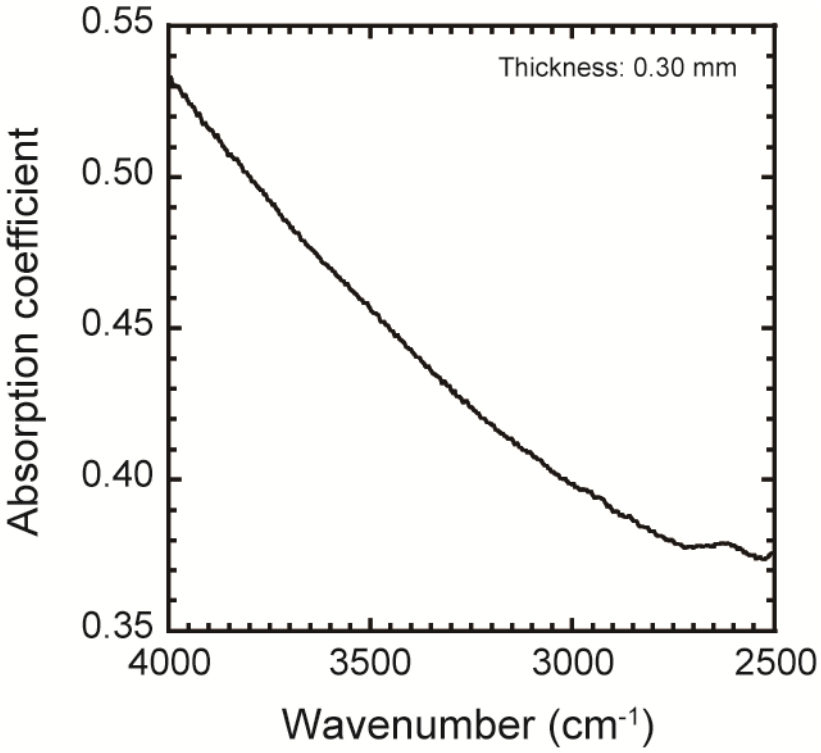

Fig. B1. FT-IR spectrum (without background correction) from the deformed undoped $f_{px} = 0$ sample (KH-14). The specimen thickness is 0.30 mm.

C Grain sizes

Olivine grain sizes (= $2\sqrt{S_i/\pi}$) normalized by the average value (i.e., d in this study) exhibit similar log-normal distributions in all samples (Fig. 2-2). The Zener relationship, which relates the fraction of the secondary (minor) phase to the grain size ratio of the primary (major) and secondary phases, predicts much a smaller secondary-phase grain size relative to the primary phase at very small secondary-phase fractions. This Zener effect is clearly observed in our samples (see Tables 2-2 and 2-3; Fig. 4-1); however, the effect on the average grain size of the sample seems to be negligible due to the small number of secondary-phase grains.

D Comparison of grain sizes measured by different methods

In Fig. D1, we compare our area-based grain size determinations with sizes measured by the line intercept method, which is often used in Earth science, including several previous experimental studies on olivine rheology (e.g., Karato et al., 1986; Hirth and Kohlstedt, 1995a; Mei and Kohlstedt, 2000a). We applied both methods to SEM images of initial, final, and reference samples of undoped f_{px} = 0 material. The images contain >100 olivine grains. In the line intercept method, we did not multiply the results by a correction factor such as 1.5, which is often used to convert the measured lengths to grain diameters. As seen in Fig. D1, both methods extract essentially the same grain sizes, which is a somewhat surprising result because the intercept method tends to measure a shorter length than a diameter of each grain, which is approximated as a circle in the area-based method. We attribute this result to a sectioning bias for larger grains in the line intercept method.

We checked the grain size determination methods used in previous works that were compiled by Wang (2000), who examined the relationship between observed $\dot{\varepsilon}_{\mathrm{diff}}$ values and $\dot{\varepsilon}_{\mathrm{diff}}$ predicted from self-diffusivities (Eq. (2-7)). Despite the small number of studies that reported grain size measurement details, we found sizes corresponding to the size measured by the line intercept method with a correction factor of 1.5 (Lessing & Gordon, 1977). As discussed above, we consider the correction factor to overestimate the grain size of samples, although the size can be regarded as a 3D grain size due to the similar coefficients used for converting 2D grain sizes to 3D. Wang (2000) showed that $\dot{\varepsilon}_{\mathrm{diff}}$ values could be well reproduced by using an $A'_{\mathrm{GB\_diff}}$ value of $150/\pi$ (Coble, 1963; Burton, 1977) multiplied by 10. Since 3D grain sizes were used in the paper, we normalized $(150/\pi) \times 10$ by 1.77^3 so that the equation holds for 2D grain sizes.

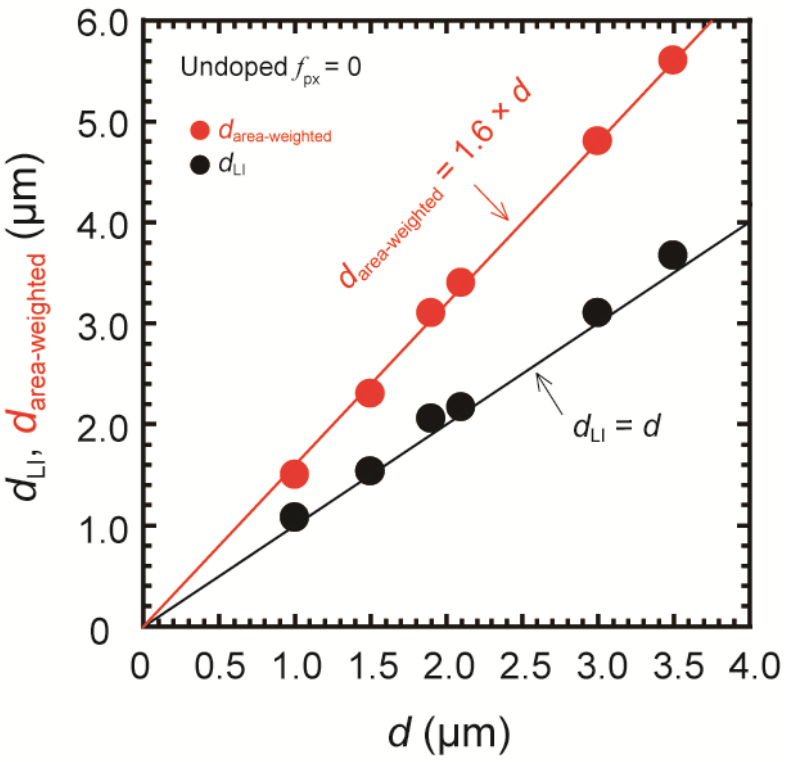

Fig. D1. Area-based olivine grain size (d in this study) versus grain size based on the line intercept method (d_{LI}) in the undeformed undoped f_{px} = 0 aggregate. d_{LI} corresponds to the average length without multiplication by a correction factor (see text). The area-weighted grain sizes (i.e., $d_{\mathrm{area-weighted}} = \frac{1}{S}\sum_{i=1}^{N} S_i \cdot d_i$ where N is the total number of grains, S is the total area of grains, and S_i is the area of the i-th grain with d_i), which will be discussed in *section 4*, are included in the figure. The $d_{\mathrm{area-weighted}}$ are systematically larger than d, and can be described by $d_{\mathrm{area-weighted}} \approx 1.6 \times d$.

E Derivation of Eq. (3-5)

Mei et al. (2002) conducted deformation experiments on SC-olivine with additions of melt (2–12 vol%) under water-saturated conditions. They analyzed the sample water contents using FTIR. We obtained values for $C_{H_2O}^{ol}$ of 30 μg/g and $C_{H_2O}^{melt}$ of 5×10^4 μg/g at T of 1150–1200˚C and P of 300 MPa from their report following the method of Withers et al. (2012). We obtained a $KD_{H_2O}^{ol-melt}$ of 6×10^{-4}, which is consistent with the value estimated in Mei et al. (2002). We used this value for all MK data. At water-saturated conditions with f_{H_2O} of <500 MPa, $C_{H_2O}^{ol}$ and $C_{H_2O}^{melt}$ are $\propto f_{H_2O}$ (Kohlstedt et al., 1996) and $\propto {f_{H_2O}}^{0.5}$ (Hamilton et al., 1964), respectively, which leads to Eq. (3-5).

F Creep data

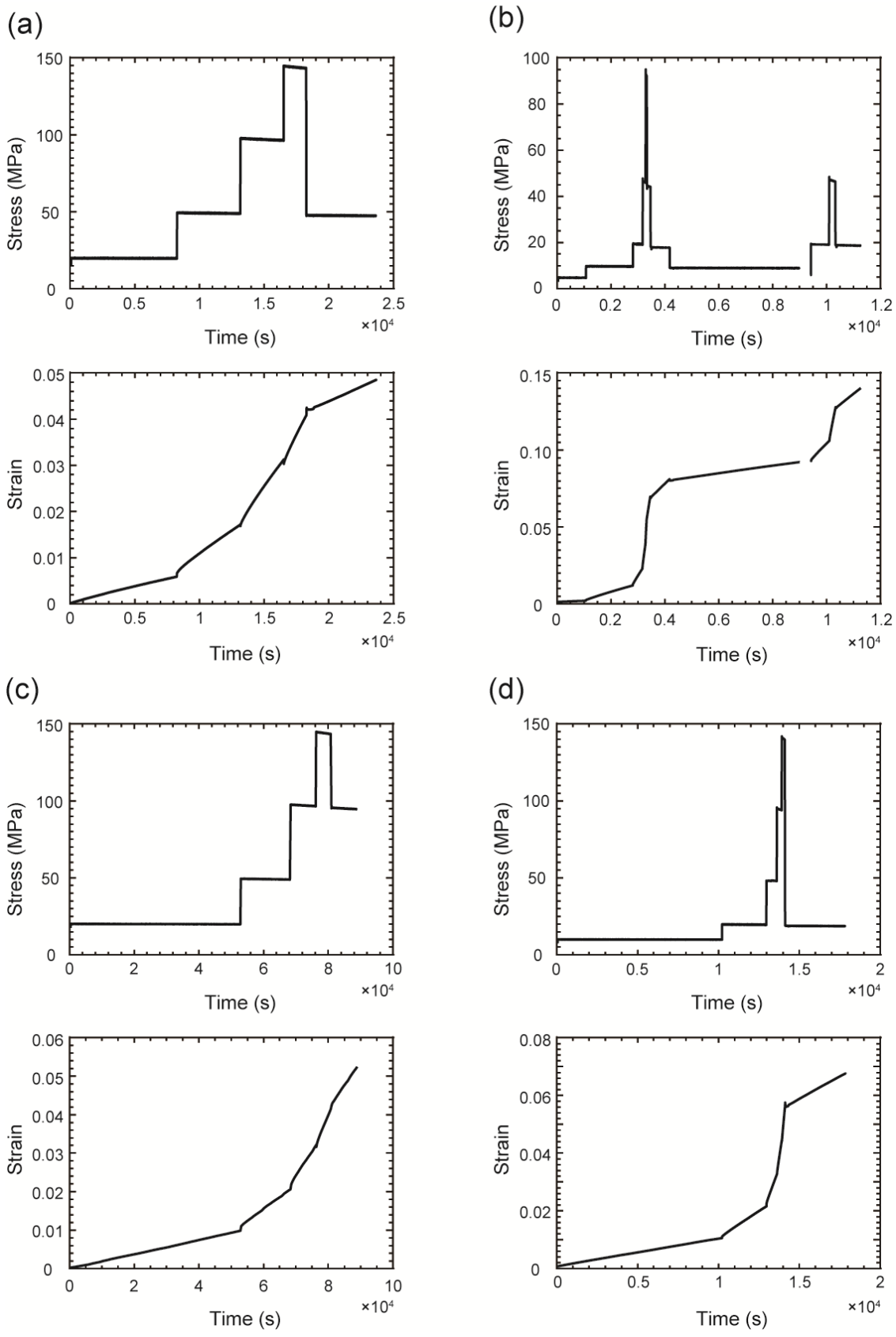
(a)
Stress (MPa)
Time (s)
×10⁴
Strain
Time (s)
×10⁴
(b)
Stress (MPa)
Time (s)
×10⁴
Strain
Time (s)
×10⁴
(c)
Stress (MPa)
Time (s)
×10⁴
Strain
Time (s)
×10⁴
(d)
Stress (MPa)
Time (s)
×10⁴
Strain
Time (s)
×10⁴

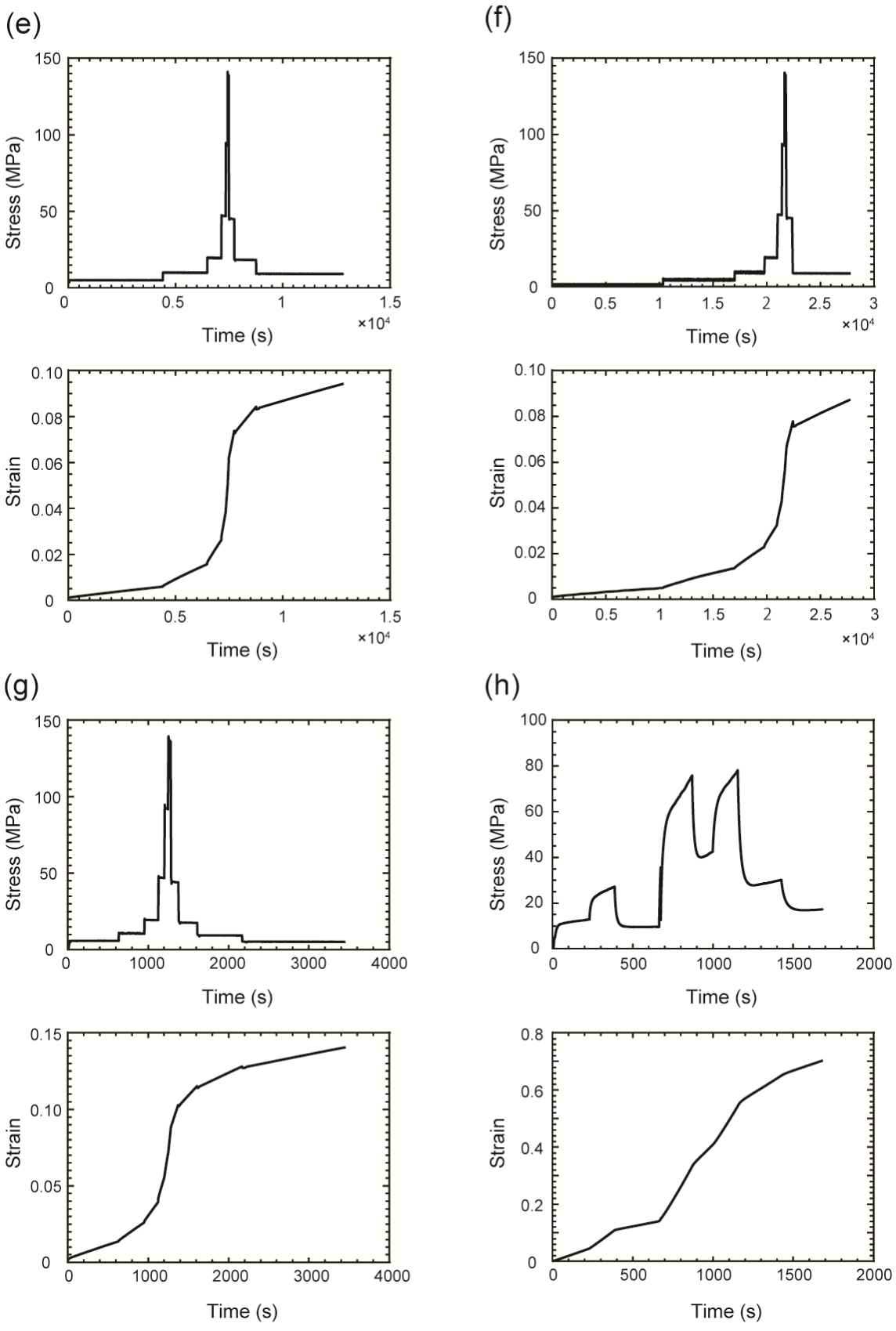
(e)
Stress (MPa)
Time (s)
×10⁴
Strain
Time (s)
×10⁴
(f)
Stress (MPa)
Time (s)
×10⁴
Strain
Time (s)
×10⁴
(g)
Stress (MPa)
Time (s)
Strain
Time (s)
(h)
Stress (MPa)
Time (s)
Strain
Time (s)

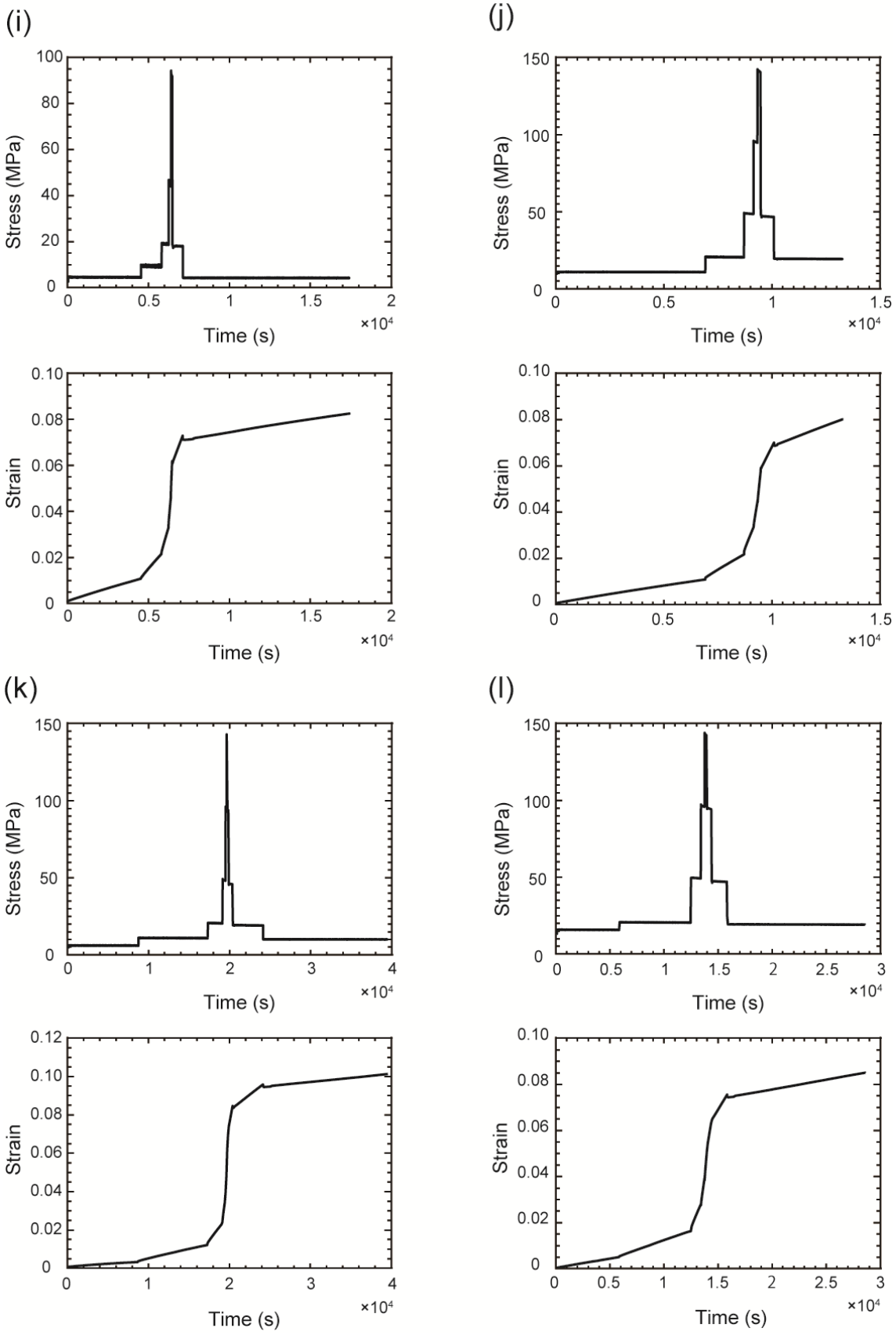
(i)
Stress (MPa)
Time (s)
×10⁴
Strain
Time (s)
×10⁴
(j)
Stress (MPa)
Time (s)
×10⁴
Strain
Time (s)
×10⁴
(k)
Stress (MPa)
Time (s)
×10⁴
Strain
Time (s)
×10⁴
(l)
Stress (MPa)
Time (s)
×10⁴
Strain
Time (s)
×10⁴

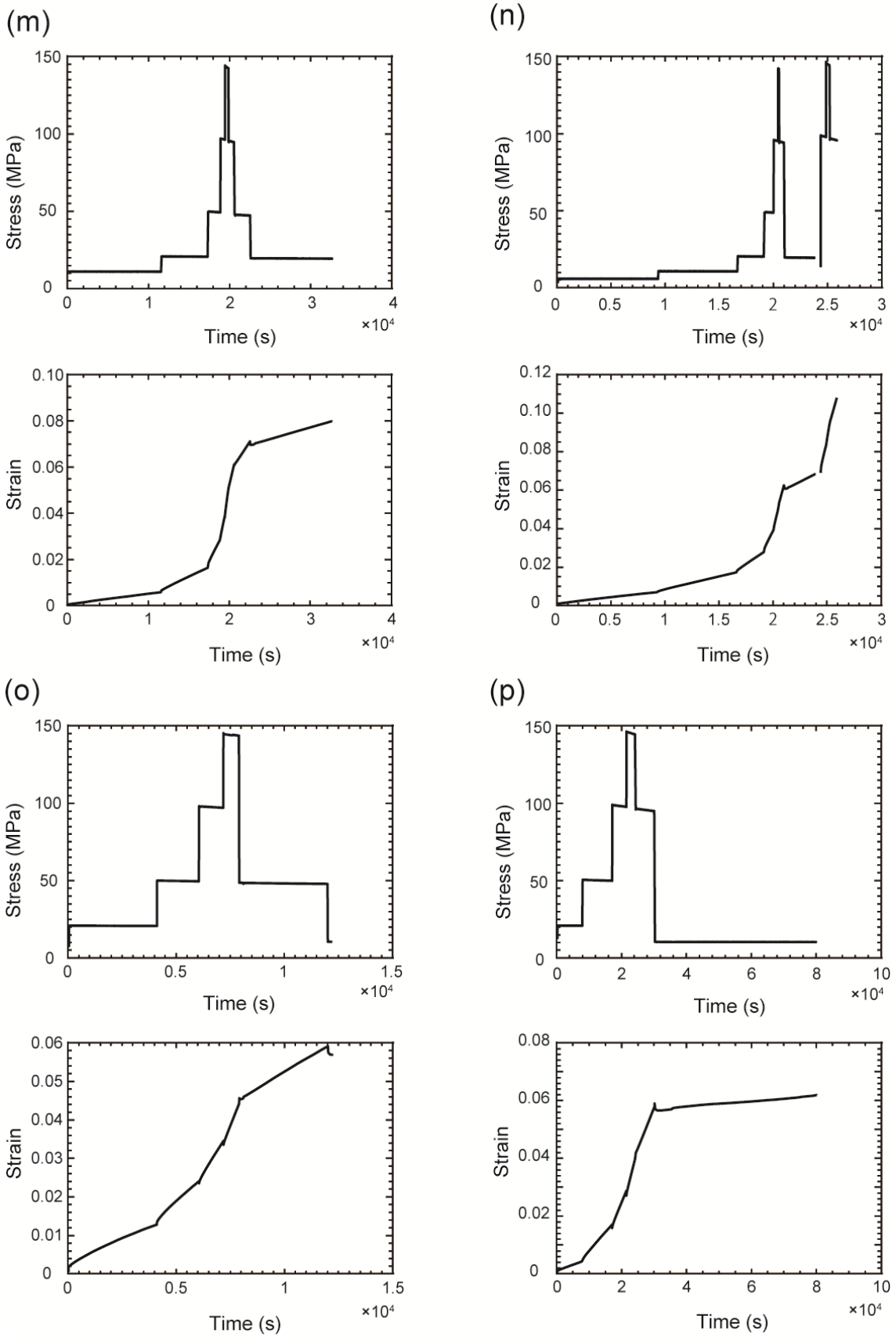
(m)
Stress (MPa)
Time (s)
×10⁴
Strain
Time (s)
×10⁴
(n)
Stress (MPa)
Time (s)
×10⁴
Strain
Time (s)
×10⁴
(o)
Stress (MPa)
Time (s)
×10⁴
Strain
Time (s)
×10⁴
(p)
Stress (MPa)
Time (s)
×10⁴
Strain
Time (s)
×10⁴

(q)

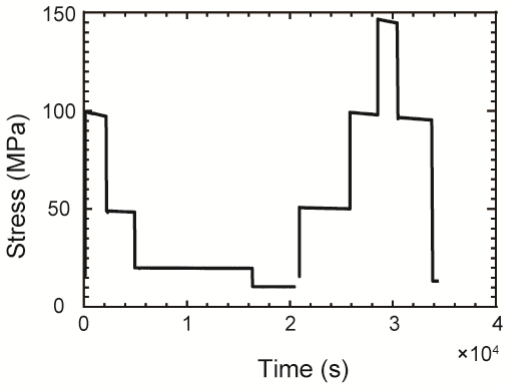
Stress (MPa)
Time (s)
×10⁴

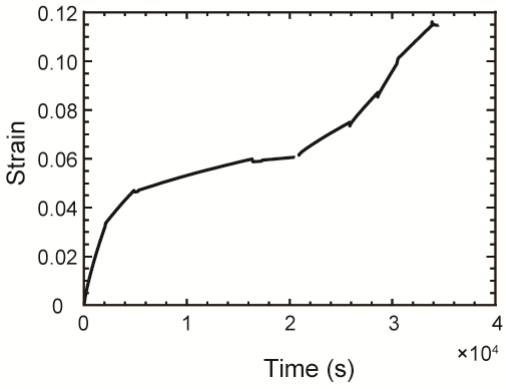
Strain
Time (s)
×10⁴

(r)

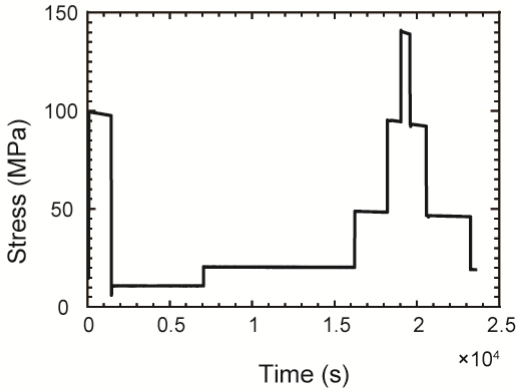
Stress (MPa)
Time (s)
×10⁴

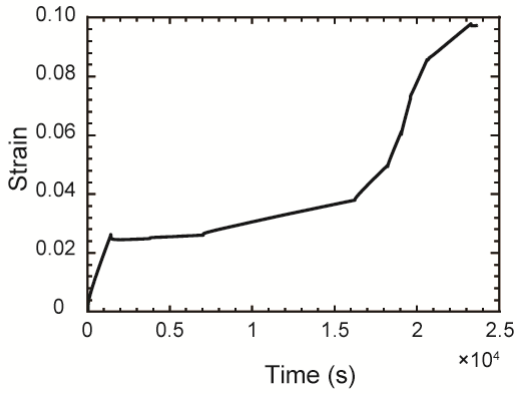
Strain
Time (s)
×10⁴

(s)

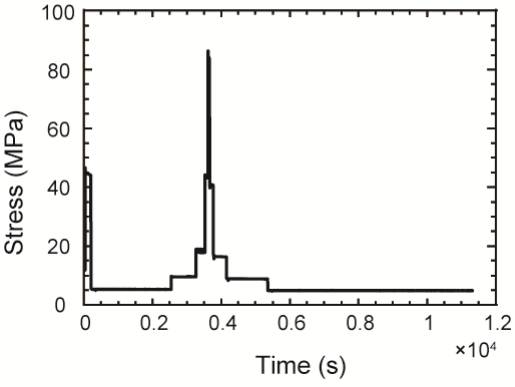
Stress (MPa)
Time (s)
×10⁴

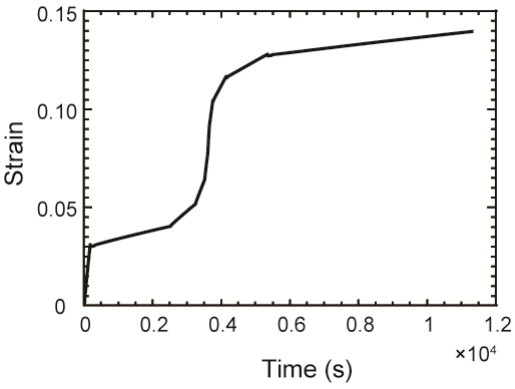
Strain
Time (s)
×10⁴

Fig. F1. Mechanical data obtained during stepped-load tests. Upper figure: time versus stress. Lower figure: time versus strain. (a) KH-14. (b) KH-50. (c) KH-52. (d) KH-53. (e) KH-54. (f) KH-55. (g) KH-68. (h) KH-71. (i) KH-72. (j) KH-81. (k) KH-87. (l) KH-90. (m) KH-91. (n) KH-92. (o) KH-138. (p) KH-143. (q) KH-152. (r) KH-171. (s) KH-172.

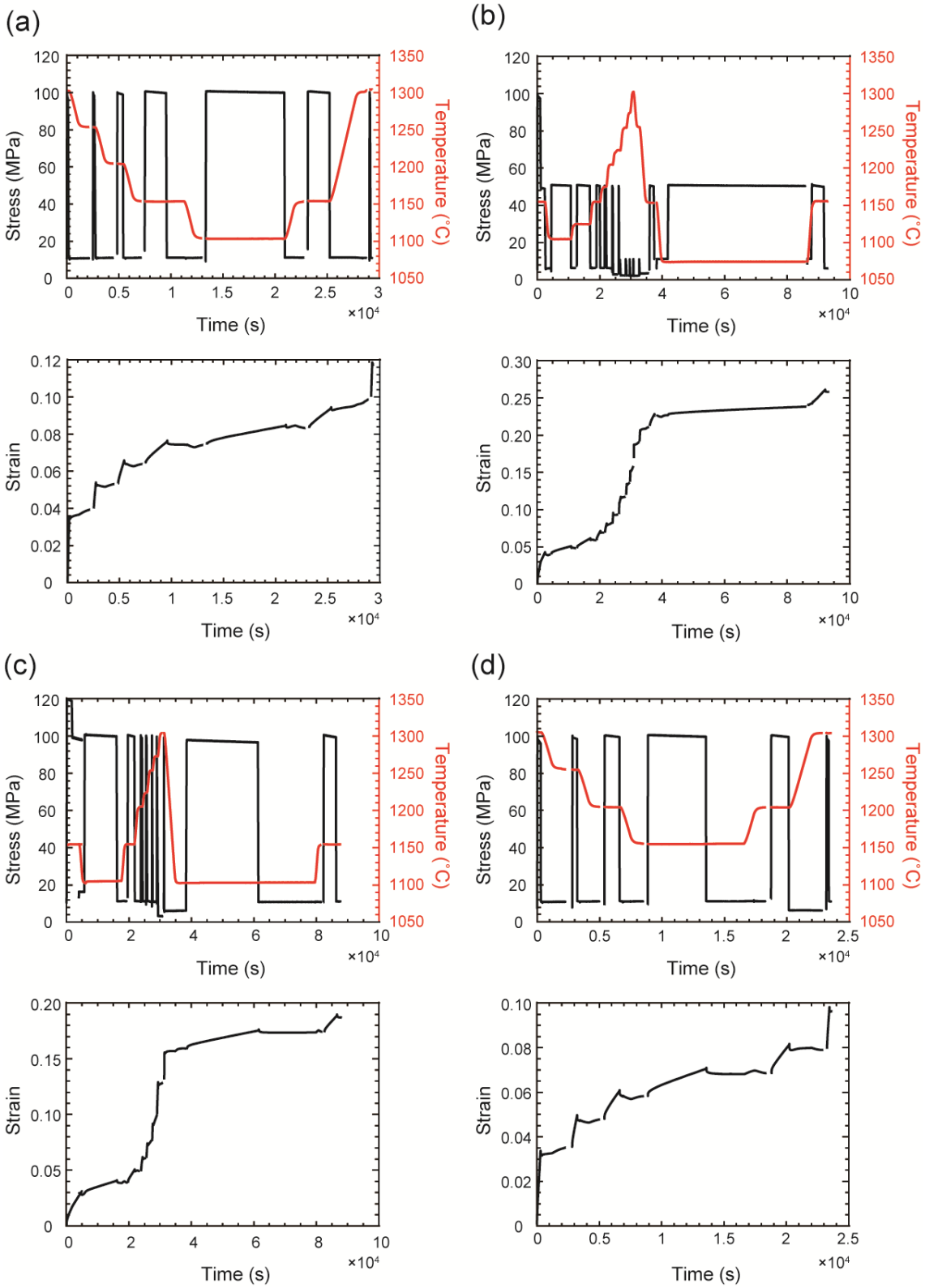
(a)
(b)
(c)
(d)
Stress (MPa)
Temperature (°C)
Time (s)
×10⁴
Strain

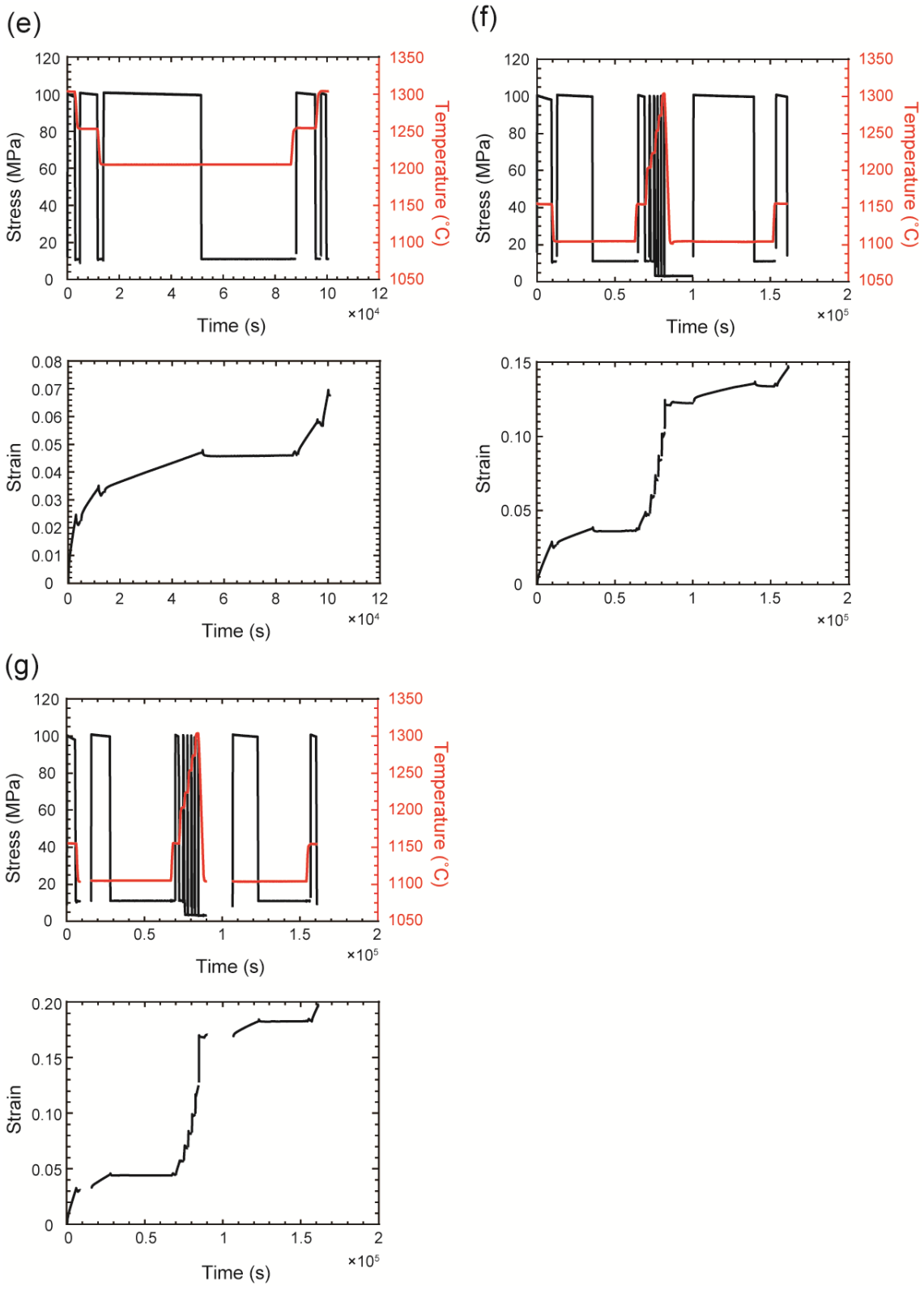
(e)
Stress (MPa)
Temperature (°C)
Time (s)
×10⁴
Strain
Time (s)
×10⁴
(f)
Stress (MPa)
Temperature (°C)
Time (s)
×10⁵
Strain
×10⁵
(g)
Stress (MPa)
Temperature (°C)
Time (s)
×10⁵
Strain
Time (s)
×10⁵

Fig. F2. Mechanical data obtained during stepped-temperature tests. Upper figure: time versus stress (black) and temperature (red). Lower figure: time versus strain. (a) KH-141. (b) KH-142. (c) KH-146. (d) KH-148. (e) KH-149. (f) KH-151. (g) KH-174.

Acknowledgements

I would like to express my sincere gratitude to my supervisor, Assoc. Prof. Takehiko Hiraga in Earthquake Research Institute (ERI), the Univ. of Tokyo. He always gave me very helpful comments and encouraged me to proceed with my Ph.D. study. Without his support, this thesis would not have been completed. I also wish to thank Prof. Yasuko Takei in ERI, the Univ. of Tokyo, for thoughtful discussions especially on experimental results and its interpretations.

I would like to thank the rest of my thesis committee: Prof. Wallis Simon, Assoc. Prof. Yoshiyuki Tanaka in the Univ. of Tokyo, Assoc. Prof. Masao Nakatani, and Prof. Hikaru Iwamori, in ERI, the Univ. of Tokyo for their insightful comments and suggestions. I am also very grateful to discussions about experimental results with Prof. David Kohlstedt in the Univ. of Minnesota, Prof. Hidehiro Yoshida, the Univ. of Tokyo, Dr. Hatsuki Yamauchi, and Dr. Tadashi Nakakoji. It was very helpful to discuss the geophysical applications with Prof. Hitoshi Kawakatsu in ERI, the Univ. of Tokyo.

I thank very much Assoc. Prof. Atsushi Yasuda in ERI, the Univ. of Tokyo, Dr. Sanae Koizumi, Natsumi Hokanishi, Masayuki Uchida, Dr. Akihiro Takeuchi, and Shigeru Ohtsuka for their technical assistance.

I thank to my colleagues, Kenta Sueyoshi, Atsuro Okamoto, Nahyeon Kim, Akihiro Ando, Akihiro Tsunoda, and Bunrin Natsui for their daily discussions and assistance in the experiments. Also I would like to thank my family for supporting me spiritually throughout writing this thesis and my life in general.

Chapter 2 and 3–4 are mainly based on Yabe et al., (2020) (DOI: 10.1029/2020JB019415) and Yabe & Hiraga (2020) (DOI: 10.1029/2020JB019416), respectively. Experimental results presented in chapter 2 (Table 2-2, and 2-3) are available in Zenodo (DOI: 10.5281/zenodo.3608499).

This study was supported by the JSPS through a Grant-in-Aid for youth Scientific Research to K. Y (17J05131). A portion of this work was conducted at the Center for Nano Lithography & Analysis of the University of Tokyo, supported by the Ministry of Education, Culture, Sports, Science and Technology (MEXT), Japan.

References

Ambrose, T. K., Wallis, D., Hansen, L. N., Waters, D. J., & Searle, M. P. (2018). Controls on the rheological properties of peridotite at a palaeosubduction interface: A transect across the base of the Oman–UAE ophiolite. *Earth and Planetary Science Letters*, *491*, 193-206.

Arzt, E., Ashby, M. F., & Verrall, R. A. (1983). Interface controlled diffusional creep. *Acta metallurgica*, *31*(12), 1977-1989.

Ashby, M. F. (1969). On interface-reaction control of Nabarro-Herring creep and sintering. *Scripta Metallurgica*, *3*(11), 837-842.

Ashby, M. F., & Verrall, R. A. (1973). Diffusion-accommodated flow and superplasticity. *Acta metallurgica*, *21*(2), 149-163.

Ashby, M. F., Edward, G. H., Davenport, J., & Verrall, R. A. (1978). Application of bound theorems for creeping solids and their application to large strain diffusional flow. *Acta Metallurgica*, *26*(9), 1379-1388.

Ave Lallemant, H. G., Mercier, J.-C. C., Carter, N. L., & Ross, J. V. (1980). Rheology of the upper mantle: inferences from peridotite xenoliths. *Tectonophysics*, *70*(1-2), 85-113.

Baba, K., Chave, A. D., Evans, R. L., Hirth, G., & Mackie, R. L. (2006). Mantle dynamics beneath the East Pacific Rise at 17 S: Insights from the Mantle Electromagnetic and Tomography (MELT) experiment. *Journal of Geophysical Research: Solid Earth*, *111*(B2).

Bai, Q., & Kohlstedt, D. L. (1993). Effects of chemical environment on the solubility and incorporation mechanism for hydrogen in olivine. *Physics and Chemistry of Minerals*, *19*(7), 460-471.Bai, J., & Raj, R. (2005). Influence of grain size variability on the strain rate dependence of the stress exponent in mixed-mode power law and diffusional creep. *Metallurgical and Materials Transactions A*, *36*(11), 2913-2919.

Bai, J., & Raj, R. (2010). Inverse problems in stochastic modeling of mixed-mode power-law and diffusional creep for distributed grain size. *Metallurgical and Materials Transactions A*, *41*(2), 308-317.

Bali, E., Bolfan-Casanova, N., & Koga, K. T. (2008). Pressure and temperature dependence of H solubility in forsterite: an implication to water activity in the Earth interior. *Earth and Planetary Science Letters*, *268*(3-4), 354-363.

Beeman, M. L., & Kohlstedt, D. L. (1993). Deformation of fine-grained aggregates of

olivine plus melt at high temperatures and pressures. *Journal of Geophysical Research: Solid Earth*, *98*(B4), 6443-6452.

Beere, W. (1978). Stresses and deformation at grain boundaries. *Philosophical Transactions of the Royal Society of London. Series A, Mathematical and Physical Sciences*, *288*(1350), 177-196.

Behn, M. D., Hirth, G., & Elsenbeck II, J. R. (2009). Implications of grain size evolution on the seismic structure of the oceanic upper mantle. *Earth and Planetary Science Letters*, *282*(1-4), 178-189.

Berbon, M. Z., & Langdon, T. G. (1999). An examination of the flow process in superplastic yttria-stabilized tetragonal zirconia. *Acta materialia*, *47*(8), 2485-2495.

Bowen, N. L., & Schairer, J. F. (1935). The system MgO-FeO-SiO 2. *American Journal of Science*, *29*(170), 151-217.

Burton, B. (1972). Interface reaction controlled diffusional creep: a consideration of grain boundary dislocation climb sources. *Materials Science and Engineering*, *10*, 9-14.

Burton, B. (1977). Diffusional creep of polycrystalline materials. *Diffusion and Defect Monograph Series*. (Vol. 5). pp. 5. Bay Village, OH: Trans Tech Publications.

Cantwell, P. R., Tang, M., Dillon, S. J., Luo, J., Rohrer, G. S., & Harmer, M. P. (2014). Grain boundary complexions. *Acta Materialia*, *62*, 1-48.

Carter, C. B., & Norton, M. G. (2013). *Ceramic materials: science and engineering*, pp. 253-265. Springer, New York.

Chakraborty, S. (1997). Rates and mechanisms of Fe-Mg interdiffusion in olivine at 980°–1300° C. *Journal of Geophysical Research: Solid Earth*, *102*(B6), 12317-12331.

Cline II, C. J., Faul, U. H., David, E. C., Berry, A. J., & Jackson, I. (2018). Redox-influenced seismic properties of upper-mantle olivine. *Nature*, *555*(7696), 355-358.

Coble, R. L. (1963). A model for boundary diffusion controlled creep in polycrystalline materials. *Journal of applied physics*, *34*(6), 1679-1682.

Dasgupta, R., Mallik, A., Tsuno, K., Withers, A. C., Hirth, G., & Hirschmann, M. M. (2013). Carbon-dioxide-rich silicate melt in the Earth's upper mantle. *Nature*, *493*(7431), 211-215.

Deines, P., Nafzinger, R. H., Ulmer, G. C., & Woermann, E. (1974). Temperature-oxygen fugacity tables for selected gas mixtures in the system C-H-O at one atmosphere total pressure. *Bulletin of the Earth and Mineral Sciences*

Experiment Station, *88*, pp. 17-27. Pennsylvania State University.

De Paola, N., Holdsworth, R. E., Viti, C., Collettini, C., & Bullock, R. (2015). Can grain size sensitive flow lubricate faults during the initial stages of earthquake propagation?. *Earth and Planetary Science Letters*, *431*, 48-58.

Dohmen, R., Chakraborty, S., & Becker, H. W. (2002). Si and O diffusion in olivine and implications for characterizing plastic flow in the mantle. *Geophysical research letters*, *29*(21), 2030.

Dunn, R. A., & Forsyth, D. W. (2003). Imaging the transition between the region of mantle melt generation and the crustal magma chamber beneath the southern East Pacific Rise with short‐period Love waves. *Journal of Geophysical Research: Solid Earth*, *108*(B7).

Dixon, J. E., Clague, D. A., Wallace, P., & Poreda, R. (1997). Volatiles in alkalic basalts form the North Arch Volcanic Field, Hawaii: extensive degassing of deep submarine-erupted alkalic series lavas. *Journal of Petrology*, *38*(7), 911-939.

Farver, J. R., & Yund, R. A. (2000). Silicon diffusion in forsterite aggregates: Implications for diffusion accommodated creep. *Geophysical Research Letters*, *27*(15), 2337-2340.

Faul, U. H., & Jackson, I. (2007). Diffusion creep of dry, melt-free olivine. *Journal of Geophysical Research: Solid Earth*, *112*, B04204.

Fei, H., Hegoda, C., Yamazaki, D., Wiedenbeck, M., Yurimoto, H., Shcheka, S., & Katsura, T. (2012). High silicon self-diffusion coefficient in dry forsterite. *Earth and Planetary Science Letters*, *345*, 95-103.

Fei, H., Koizumi, S., Sakamoto, N., Hashiguchi, M., Yurimoto, H., Marquardt, K., ... & Katsura, T. (2016). New constraints on upper mantle creep mechanism inferred from silicon grain-boundary diffusion rates. *Earth and Planetary Science Letters*, *433*, 350-359.

Gasparik, T. (2003). *Phase diagrams for geoscientists*, Springer, Berlin, Germany.

Gribb, T. T., & Cooper, R. F. (1998). Low-frequency shear attenuation in polycrystalline olivine: Grain boundary diffusion and the physical significance of the Andrade model for viscoelastic rheology. *Journal of Geophysical Research: Solid Earth*, *103*(B11), 27267-27279.

Hamilton, D. L., Burnham, C. W., & Osborn, E. F. (1964). The solubility of water and effects of oxygen fugacity and water content on crystallization in mafic magmas. *Journal of Petrology*, *5*(1), 21-39.

Hammond, W. C., & Toomey, D. R. (2003). Seismic velocity anisotropy and heterogeneity beneath the Mantle Electromagnetic and Tomography Experiment

(MELT) region of the East Pacific Rise from analysis of P and S body waves. *Journal of Geophysical Research: Solid Earth*, *108*(B4).

Hansen, L. N., & Warren, J. M. (2015). Quantifying the effect of pyroxene on deformation of peridotite in a natural shear zone. *Journal of Geophysical Research: Solid Earth*, *120*(4), 2717-2738.

Hansen, L. N., Zimmerman, M. E., & Kohlstedt, D. L. (2011). Grain boundary sliding in San Carlos olivine: Flow law parameters and crystallographic-preferred orientation. *Journal of Geophysical Research: Solid Earth*, *116*, B08201.

Harigane, Y., Mizukami, T., Morishita, T., Michibayashi, K., Abe, N., & Hirano, N. (2011). Direct evidence for upper mantle structure in the NW Pacific Plate: Microstructural analysis of a petit-spot peridotite xenolith. *Earth and Planetary Science Letters*, *302*(1-2), 194-202.

Herring, C. (1950). Diffusional viscosity of a polycrystalline solid. *Journal of applied physics*, *21*(5), 437-445.

Hiraga, T., Nagase, T., & Akizuki, M. (1999). The structure of grain boundaries in granite-origin ultramylonite studied by high-resolution electron microscopy. *Physics and chemistry of minerals*, *26*(8), 617-623.

Hiraga, T., Anderson, I., Zimmerman, M., Mei, S., & Kohlstedt, D.L. (2002). Structure and chemistry of grain boundaries in deformed, olivine+ basalt and partially molten lherzolite aggregates: evidence of melt-free grain boundaries. *Contributions to Mineralogy and Petrology*, *144*(2), 163-175.

Hiraga, T., Anderson, I. M., & Kohlstedt, D. L. (2003). Chemistry of grain boundaries in mantle rocks. *American Mineralogist*, *88*(7), 1015-1019.

Hiraga, T., Anderson, I. M., & Kohlstedt, D. L. (2004). Grain boundaries as reservoirs of incompatible elements in the Earth's mantle. *Nature*, *427*(6976), 699-703.

Hiraga, T., & Kohlstedt, D. L. (2007). Equilibrium interface segregation in the diopside–forsterite system I: Analytical techniques, thermodynamics, and segregation characteristics. *Geochimica et Cosmochimica Acta*, *71*(5), 1266-1280.

Hiraga, T., & Kohlstedt, D. L. (2009). Systematic distribution of incompatible elements in mantle peridotite: importance of intra-and inter-granular melt-like components. *Contributions to Mineralogy and Petrology*, *158*(2), 149-167.

Hiraga, T., Miyazaki, T., Tasaka, M., & Yoshida, H. (2010a). Mantle superplasticity and its self-made demise. *Nature*, *468*(7327), 1091-1094.

Hiraga, T., Tachibana, C., Ohashi, N., & Sano, S. (2010b). Grain growth systematics for forsterite±enstatite aggregates: Effect of lithology on grain size in the upper

mantle. *Earth and Planetary Science Letters*, *291*(1-4), 10-20.

Hirschmann, M. M. (2000). Mantle solidus: Experimental constraints and the effects of peridotite composition. *Geochemistry, Geophysics, Geosystems*, *1*(10), 2000GC000070.

Hirschmann, M. M., Tenner, T., Aubaud, C., & Withers, A. C. (2009). Dehydration melting of nominally anhydrous mantle: The primacy of partitioning. *Physics of the Earth and Planetary Interiors*, *176*(1-2), 54-68.

Hirschmann, M. M. (2010). Partial melt in the oceanic low velocity zone. *Physics of the Earth and Planetary Interiors*, *179*(1-2), 60-71.

Hirth, G., & Kohlstedt, D. L. (1995a). Experimental constraints on the dynamics of the partially molten upper mantle: Deformation in the diffusion creep regime. *Journal of Geophysical Research: Solid Earth*, *100*(B2), 1981-2001.

Hirth, G., & Kohlstedt, D. L. (1995b). Experimental constraints on the dynamics of the partially molten upper mantle: 2. Deformation in the dislocation creep regime. *Journal of Geophysical Research: Solid Earth*, *100*(B8), 15441-15449.

Hirth, G., & Kohlstedt, D. L. (1996). Water in the oceanic upper mantle: implications for rheology, melt extraction and the evolution of the lithosphere. *Earth and Planetary Science Letters*, *144*(1-2), 93-108.

Hirth, G. & Kohlstedt, D. L. (2003). Rheology of the upper mantle and the mantle wedge: A view from the experimentalists. In *Inside the Subduction Factory* (ed. J. E. Eiler), pp. 83-105. American Geophysical Union.

Holland, T. J. B., & Powell, R. (2011). An improved and extended internally consistent thermodynamic dataset for phases of petrological interest, involving a new equation of state for solids. *Journal of Metamorphic Geology*, *29*(3), 333-383.

Holm, K., Embury, J. D., & Purdy, G. R. (1977). The structure and properties of microduplex Zr-Nb alloys. *Acta Metallurgica*, *25*(10), 1191-1200.

Jain, C., Korenaga, J., & Karato, S. I. (2018). On the grain size sensitivity of olivine rheology. *Journal of Geophysical Research: Solid Earth*, *123*(1), 674-688.

Jain, C., Korenaga, J., & Karato, S. I. (2019). Global Analysis of Experimental Data on the Rheology of Olivine Aggregates. *Journal of Geophysical Research: Solid Earth*, *124*(1), 310-334.

Jamtveit, B., Brooker, R., Brooks, K., Larsen, L. M., & Pedersen, T. (2001). The water content of olivines from the North Atlantic Volcanic Province. *Earth and Planetary Science Letters*, *186*(3-4), 401-415.

Karato, S. I. (1986). Does partial melting reduce the creep strength of the upper mantle?. *Nature*, *319*(6051), 309-310.Karato, S. I., Paterson, M. S., &

FitzGerald, J. D. (1986). Rheology of synthetic olivine aggregates: Influence of grain size and water. *Journal of Geophysical Research: Solid Earth*, *91*(B8), 8151-8176.

Karato, S. I., & Jung, H. (1998). Water, partial melting and the origin of the seismic low velocity and high attenuation zone in the upper mantle. *Earth and Planetary Science Letters*, *157*(3-4), 193-207.

Karato, S. I., Paterson, M. S., & FitzGerald, J. D. (1986). Rheology of synthetic olivine aggregates: Influence of grain size and water. *Journal of Geophysical Research: Solid Earth*, *91*(B8), 8151-8176.

Keefner, J. W., Mackwell, S. J., Kohlstedt, D. L., & Heidelbach, F. (2011). Dependence of dislocation creep of dunite on oxygen fugacity: implications for viscosity variations in Earth's mantle. *Journal of Geophysical Research: Solid Earth*, *116*, B05201.

Kohlstedt, D. L., Keppler, H., & Rubie, D. C. (1996). Solubility of water in the α, β and γ phases of (Mg, Fe) 2 SiO 4. *Contributions to Mineralogy and Petrology*, *123*(4), 345-357.

Koizumi, S., Hiraga, T., Tachibana, C., Tasaka, M., Miyazaki, T., Kobayashi, T., ... & Sano, S. (2010). Synthesis of highly dense and fine-grained aggregates of mantle composites by vacuum sintering of nano-sized mineral powders. *Physics and Chemistry of Minerals*, *37*(8), 505-518.

Kojitani, H., & Akaogi, M. (1997). Melting enthalpies of mantle peridotite: calorimetric determinations in the system CaO-MgO-Al2O3-SiO2 and application to magma generation. *Earth and Planetary Science Letters*, *153*(3-4), 209-222.

Korenaga, J., & Karato, S. I. (2008). A new analysis of experimental data on olivine rheology. *Journal of Geophysical Research: Solid Earth*, *113*, B02403.

Lee, D. (1970). Structural changes during the superplastic deformation. *Metallurgical and Materials Transactions B*, *1*(1), 309-311.

Lessing, P. A., & Gordon, R. S. (1977). Creep of polycrystalline alumina, pure and doped with transition metal impurities. *Journal of Materials Science*, *12*(11), 2291-2302.

Linckens, J., Herwegh, M., Müntener, O., & Mercolli, I. (2011). Evolution of a polymineralic mantle shear zone and the role of second phases in the localization of deformation. *Journal of Geophysical Research: Solid Earth*, *116*, B06210.

Liu, S., Tommasi, A., Vauchez, A., & Mazzucchelli, M. (2019). Deformation, Annealing, Melt‐Rock Interaction, and Seismic Properties of an Old Domain of the Equatorial Atlantic Lithospheric Mantle. *Tectonics*, *38*(4), 1164-1188.

Maruyama, G., & Hiraga, T. (2017a). Grain- to multiple-grain-scale deformation processes during diffusion creep of forsterite + diopside aggregate: 1. Direct observations. *Journal of Geophysical Research: Solid Earth*, *122*(8), 5890-5915.

Maruyama, G., & Hiraga, T. (2017b). Grain- to multiple-grain-scale deformation processes during diffusion creep of forsterite + diopside aggregate: 2. Grain boundary sliding-induced grain rotation and its role in crystallographic preferred orientation in rocks. *Journal of Geophysical Research: Solid Earth*, *122*(8), 5916-5934.

McKenzie, D. A. N., & Bickle, M. J. (1988). The volume and composition of melt generated by extension of the lithosphere. *Journal of petrology*, *29*(3), 625-679.

McLean, D. (1957). *Grain boundaries in metals*. pp. 116-149. Clarendon Press, Oxford.

Mei, S., & Kohlstedt, D. L. (2000a). Influence of water on plastic deformation of olivine aggregates: 1. Diffusion creep regime. *Journal of Geophysical Research: Solid Earth*, *105*(B9), 21457-21469.

Mei, S., & Kohlstedt, D. L. (2000b). Influence of water on plastic deformation of olivine aggregates: 2. Dislocation creep regime. *Journal of Geophysical Research: Solid Earth*, *105*(B9), 21471-21481.

Mei, S., Bai, W., Hiraga, T., & Kohlstedt, D. L. (2002). Influence of melt on the creep behavior of olivine–basalt aggregates under hydrous conditions. *Earth and Planetary Science Letters*, *201*(3-4), 491-507.

Miyazaki, T., Sueyoshi, K., & Hiraga, T. (2013). Olivine crystals align during diffusion creep of Earth's upper mantle. *Nature*, *502*(7471), 321-326.

Nabarro, F. R. N. (1948). Deformation of crystals by the motion of single ions. *Report of a Conference on the Strength of Solids*, 75-90.

Nakakoji, T., & Hiraga, T. (2018). Diffusion creep and grain growth in forsterite+ 20 vol% enstatite aggregates: 2. Their common diffusional mechanism and its consequence for weak-temperature-dependent viscosity. *Journal of Geophysical Research: Solid Earth*, *123*(11), 9513-9527.

Nakakoji, T., Hiraga, T., Nagao, H., Ito, S., & Kano, M. (2018). Diffusion creep and grain growth in forsterite+ 20 vol% enstatite aggregates: 1. High-resolution experiments and their data analyses. *Journal of Geophysical Research: Solid Earth*, *123*(11), 9486-9512.

Nakamura, A., & Schmalzried, H. (1984). On the Fe^{2+}- Mg^{2+}-Interdiffusion in Olivine (II). *Berichte der Bunsengesellschaft für physikalische Chemie*, *88*(2), 140-145.

Nettles, M., & Dziewoński, A. M. (2008). Radially anisotropic shear velocity structure of the upper mantle globally and beneath North America. *Journal of*

Geophysical Research: Solid Earth, *113*, B02303.

Nichols, A. R. L., Carroll, M. R., & Höskuldsson, A. (2002). Is the Iceland hot spot also wet? Evidence from the water contents of undegassed submarine and subglacial pillow basalts. *Earth and Planetary Science Letters*, *202*(1), 77-87.

Nicolas, A., & Christensen, N. I. (1987). Formation of anisotropy in upper mantle peridotites: a review, in *Composition, structure and dynamics of the lithosphere-asthenosphere system*, *Geodynamics*, vol. 16, edited by K. Fuchs and C. Froidevaux, pp. 111-123, American Geophysical Union, Washington DC.

O'Leary, J. A., Gaetani, G. A., & Hauri, E. H. (2010). The effect of tetrahedral Al^{3+} on the partitioning of water between clinopyroxene and silicate melt. *Earth and Planetary Science Letters*, *297*(1-2), 111-120.

Owen, D. M., & Chokshi, A. H. (1998). The high temperature mechanical characteristics of superplastic 3 mol% yttria stabilized zirconia. *Acta Materialia*, *46*(2), 667-679.

Raj, R., & Ashby, M. F. (1971). On grain boundary sliding and diffusional creep. *Metallurgical transactions*, *2*(4), 1113-1127.

Rudge, J. F. (2018). The viscosities of partially molten materials undergoing diffusion creep. *Journal of Geophysical Research: Solid Earth*, *123*(12), 10534-10562.

Rust, M. A., & Todd, R. I. (2011). Surface studies of Region II superplasticity of AA5083 in shear: Confirmation of diffusion creep, grain neighbour switching and absence of dislocation activity. *Acta Materialia*, *59*(13), 5159-5170.

Saal, A. E., Hauri, E. H., Langmuir, C. H., & Perfit, M. R. (2002). Vapour undersaturation in primitive mid-ocean-ridge basalt and the volatile content of Earth's upper mantle. *Nature*, *419*(6906), 451-455.

Salters, V. J., & Stracke, A. (2004). Composition of the depleted mantle. *Geochemistry, Geophysics, Geosystems*, *5*(5), Q05B07.

Simons, K., Dixon, J., Schilling, J. G., Kingsley, R., & Poreda, R. (2002). Volatiles in basaltic glasses from the Easter‐Salas y Gomez Seamount Chain and Easter Microplate: Implications for geochemical cycling of volatile elements. *Geochemistry, Geophysics, Geosystems*, *3*(7), 1-29.

Sleep, N. H. (1975). Formation of oceanic crust: some thermal constraints. *Journal of Geophysical Research*, *80*(29), 4037-4042.

Smith, C. S. (1948). Grains, phases, and interfaces: an interpretation of microstructure. *Transactions of the American Institute of Mining and Metallurgical Engineers*, *175*, 15-51.

Spingarn, J. R., & Nix, W. D. (1978). Diffusional creep and diffusionally

accommodated grain rearrangement. *Acta Metallurgica*, *26*(9), 1389-1398.

Stocker, R. L., & Ashby, M. F. (1973). On the rheology of the upper mantle. *Reviews of Geophysics*, *11*(2), 391-426.

Sundberg, M., & Cooper, R. F. (2008). Crystallographic preferred orientation produced by diffusional creep of harzburgite: Effects of chemical interactions among phases during plastic flow. *Journal of Geophysical Research: Solid Earth*, *113*(B12).

Takei, Y. (2000). Acoustic properties of partially molten media studied on a simple binary system with a controllable dihedral angle. *Journal of Geophysical Research: Solid Earth*, *105*(B7), 16665-16682.

Takei, Y. (2017). Effects of partial melting on seismic velocity and attenuation: A new insight from experiments. *Annual Review of Earth and Planetary Sciences*, *45*, 447-470.

Takei, Y., & Holtzman, B. K. (2009). Viscous constitutive relations of solid-liquid composites in terms of grain boundary contiguity: 1. Grain boundary diffusion control model. *Journal of Geophysical Research: Solid Earth*, *114*, B06205.

Tasaka, M., & Hiraga, T. (2013). Influence of mineral fraction on the rheological properties of forsterite+ enstatite during grain-size-sensitive creep: 1. Grain size and grain growth laws. *Journal of Geophysical Research: Solid Earth*, *118*(8), 3970-3990.

Tasaka, M., Hiraga, T., & Zimmerman, M. E. (2013). Influence of mineral fraction on the rheological properties of forsterite + enstatite during grain-size-sensitive creep: 2. Deformation experiments. *Journal of Geophysical Research: Solid Earth*, *118*(8), 3991-4012.

Turcotte, D. L, & Schubert, G. (2014). *Geodynamics*, 3rd ed. Cambridge University Press, Cambridge, UK.

Turner, A. J., Katz, R. F., & Behn, M. D. (2015). Grain-size dynamics beneath mid-cean ridges: Implications for permeability and melt extraction. *Geochemistry, Geophysics, Geosystems*, *16*(3), 925-946.

Wakai, F., & Nagono, T. (1988). The role of interface-controlled diffusion creep on superplasticity of yttria-stabilized tetragonal ZrO 2 polycrystals. *Journal of materials science letters*, *7*(6), 607-609.

Wanamaker, B. J. (1994). Point defect diffusivites in San Carlos olivine derived from reequilibration of electrical conductivity following changes in oxygen fugacity. *Geophysical research letters*, *21*(1), 21-24.

Wang, J. N. (2000). An investigation of the deformation mechanism in grain size-

sensitive Newtonian creep. *Acta materialia*, *48*(7), 1517-1531.

Warren, J. M., & Hirth, G. (2006). Grain size sensitive deformation mechanisms in naturally deformed peridotites. *Earth and Planetary Science Letters*, *248*(1-2), 438-450.

Watts, A. B., & Zhong, S. (2000). Observations of flexure and the rheology of oceanic lithosphere. *Geophysical Journal International*, *142*(3), 855-875.

Withers, A. C., Bureau, H., Raepsaet, C., & Hirschmann, M. M. (2012). Calibration of infrared spectroscopy by elastic recoil detection analysis of H in synthetic olivine. *Chemical Geology*, *334*, 92-98.

Yabe, K., & Hiraga, T. (2020). Grain-boundary diffusion creep of olivine: 2. Solidus effects and consequences for the viscosity of the oceanic upper mantle. *Journal of Geophysical Research: Solid Earth*.

Yabe, K., Sueyoshi, K., & Hiraga, T. (2020). Grain-boundary diffusion creep of olivine: 1. Experiments at 1 atm. *Journal of Geophysical Research: Solid Earth*.

Yamauchi, H., & Takei, Y. (2016). Polycrystal anelasticity at near-solidus temperatures. *Journal of Geophysical Research: Solid Earth*, *121*(11), 7790-7820.

Yasuda, A. (2014). A new technique using FT-IR micro-reflectance spectroscopy for measurement of water concentrations in melt inclusions. *Earth, Planets and Space*, *66*(1), 34.

Yoshida, H., Okada, K., Ikuhara, Y., & Sakuma, T. (1997). Improvement of high-temperature creep resistance in fine-grained Al2O3 by Zr4+ segregation in grain boundaries. *Philosophical magazine letters*, *76*(1), 9-14.

Yoshida, H., Yamamoto, T., Ikuhara, Y., & Sakuma, T. (2002). A change in the chemical bonding strength and high-temperature creep resistance in Al2O3 with lanthanoid oxide doping. *Philosophical Magazine A*, *82*(3), 511-525.

Zhao, Y. H., Ginsberg, S. B., & Kohlstedt, D. L. (2004). Solubility of hydrogen in olivine: dependence on temperature and iron content. *Contributions to Mineralogy and Petrology*, *147*(2), 155-161.

Zhao, Y. H., Zimmerman, M. E., & Kohlstedt, D. L. (2009). Effect of iron content on the creep behavior of olivine: 1. Anhydrous conditions. *Earth and Planetary Science Letters*, *287*(1-2), 229-240.

Zhao, N., Hirth, G., Cooper, R. F., Kruckenberg, S. C., & Cukjati, J. (2019). Low viscosity of mantle rocks linked to phase boundary sliding. *Earth and Planetary Science Letters*, *517*, 83-94.

Zhong, S., & Watts, A. B. (2013). Lithospheric deformation induced by loading of the

Hawaiian Islands and its implications for mantle rheology. *Journal of Geophysical Research: Solid Earth*, *118*(11), 6025-6048.

Zimmerman, M. E., & Kohlstedt, D. L. (2004). Rheological properties of partially molten lherzolite. *Journal of Petrology*, *45*(2), 275-298.